University of Southampton

Faculty of Engineering and Physical Sciences
Department of Physics and Astronomy

Walking Technicolor in the LHC Era and Beyond

Azaria Deborah Coupe

Submitted for the degree of
Doctor of Philosophy

September 2019

ABSTRACT

In this thesis we explore the compelling BSM model of Walking Technicolor, where *new strong dynamics* with a modified slowly running (walking) coupling dynamically break electroweak symmetry. We detail the Next-to-Minimal Walking Technicolor (NMWT) model, connecting an effective chiral Lagrangian to the underlying dynamics via the Weinberg Sum Rules. We discuss the theoretical upper limit on the NMWT scale, M_A, set by the requirement of walking dynamics, and experimental limits from reducing tension with Electroweak Precision Data.

We investigate the potential of the Large Hadron Collider (LHC) to probe the NMWT model at LHC@13TeV, $36fb^{-1}$, using dilepton signatures from heavy neutral Z' and Z'' resonances predicted by the model. We establish a new limit in the $(M_A, \tilde{g})$ plane, demonstrating the complementarity of the two resonances. We find the most conservative limit as $M_A > 3$TeV for low $\tilde{g}$. We set the first complementary limits from searches in the Drell-Yan produced VV/Vh channels, demonstrating new potential to probe the intermediate-high $\tilde{g}$ regime.

We use a holographic model to explore WTC from a top-down approach with varying number of techniquark colours and flavours (N_c,N_f), tuning the gauge running dynamics to produce a light Higgs and low S parameter. The resulting models predict technimeson masses and couplings above the current LHC limits, where the top-down equivalent model to NMWT lies at $M_A \simeq 4$TeV, $\tilde{g} \simeq 8$. This estimate provides a benchmark for the challenge of exclusion/discovery of new strong dynamics at future collider experiments.

We begin the task of determining the future of Walking Technicolor, developing a procedure for setting expected 95% CL limits on neutral resonances in the DY dilepton channel. We use this to predict the exclusions on the NMWT parameter space for the LHC era up to HLLHC@14TeV, $3ab^{-1}$, and for future 27TeV and 100TeV colliders. The DY dilepton channel is limited by the systematics, but can begin to probe the most extreme (large number of techni-doublets) top-down models from holography. We draw prospects on predicting limits from VV/Vh searches from Drell-Yan and Vector Boson Fusion production, and to ultimately determine the fate of Walking Technicolor in the LHC era and beyond.

Contents

List of Figures

List of Tables

Declaration of Authorship

I, Azaria Coupe, declare that this thesis, entitled ‘Walking Technicolor in the LHC Era and Beyond’, and the work presented in it are my own.

I confirm that:

- This work was done wholly or mainly while in candidature for a research degree at this University.
- No part of this thesis has previously been submitted for a degree or any other qualification at this University or any other institution.
- Where I have consulted the published work of others, this is always clearly attributed.
- Where I have quoted from the work of others, the source is always given. With the exception of such quotations, this thesis is entirely my own work.
- I have acknowledged all main sources of help.
- Where the thesis is based on work done by myself jointly with others, I have made clear exactly what was done by others and what I have contributed myself.
- Work contained in this thesis has been previously published in [4, 5], with work included in this thesis from [6] to be published.

Signed: .... Date: ....

Copyright Statement

Thesis: Azaria Deborah Coupe (2019) "Walking Technicolor in the LHC Era and Beyond", University of Southampton, Faculty of Engineering and Physical Sciences, Department of Physics and Astronomy, pagination.

Acknowledgements

Firstly I would like to thank my supervisor, Sasha Belyaev, for taking a chance on me as a summer intern back in 2014 and inspiring a passion for BSM phenomenology and Technicolor, which ultimately provided the basis for these 4 years of PhD research. I always learn something new from our conversations whether that be about physics or otherwise, and I thank him for pushing me to strengthen my confidence and also being sympathetic and understanding when needed. I would also like to thank my second supervisor, Nick Evans, for giving me great advice and support in personal and professional areas, and for taking the time to answer my (often basic!) questions on Holography.

I've been lucky to collaborate with a host of wonderful physicists whom I would like to thank for broadening my understanding of BSM physics from experimental, phenomenological, and theoretical perspectives. These excellent people are Mads Frandsen, Emmanuel Olaiya, Claire Shepherd-Themistocleous, Marc Scott, and Daniel Locke. I would especially like to thank Mads, whose thesis has been my Technicolor bible, and whose extensive collaboration was integral to the early years of my PhD.

I would like to thank all of the residents of 4007, past and present, for being a fantastic mixture of hilarious, supportive, helpful, and exceedingly nerdy, a finer office has never existed! To Simon King, thank you for being a fantastic friend, a hilarious presence in every environment, for enabling me to open up about and ultimately escape from my home situation, and for offering me a place to stay during the resulting period of homelessness. To Ronnie Rodgers, thank you for being an endless font of physics knowledge, for touring the hospitals of England with me whenever I was taken in, and for introducing me to the wonderful world of RPGs (even though I still can't un-hear Alex Titterton's accent!).

I thank Anthony Preston for his advice, excessive cats, and enriching my life with all manner of oddities. I thank Marc Scott for being an equally wonderful support in my early years in the office, and for his continued guidance and collaboration even after finishing his own PhD. Thank you to James Richings for being both brilliantly sarcastic and incredibly kind, and for being an unintentionally comedic D&D player. Thank you to Sam Rowley for taking the brunt of the regional jokes - surprising for a Welsh lady to be out-sheeped - and for being an excellent fellow Mayflower with whom I have shared the highs and lows of Mayflower life. Thank you also to Sophie Dillon and Andrew Lawson for their excellent performance as fellow D&D players, and for their friendship throughout the years.

To the Elessar to my Undòmiel, Tom Jefferson-Brain, thank you for supporting me in rebuilding my confidence and for always championing me to succeed, for treating me as an equal and enriching my life beyond measure. In addition to your love and support, our laser physics collaboration has extended my knowledge outside of particle physics and deepened my appreciation for machine learning, and I am so proud to have published this work together. I would also like to thank BBAS for accepting me as a member and becoming excellent friends/D&D players/lunch-goers.

I'd like to thank my little sister, Sasha Coupe, of whom I am incredibly proud. Celebrating your successes, from your degree, to your job and promotions, to personal successes, has been astoundingly wonderful and inspiring. You've helped me to see that personal hardship can be overcome, and that sometimes all I need in life is a long chat with a sassy Welsh woman to set me right!

Finally, to my mother, Deborah Coupe, you are the reason I am here today, writing this thesis and achieving a life-long dream. Thank you for being my Eärendil, I have been in many dark places but in all you are my light in the darkness. You have been with me for all the ups and downs of the last 4 years, and indeed my entire life, always reminding me that I am good enough and supporting me in my dream to become a successful physicist. Thank you for fostering my love of science, for continuing to push for answers with my health, and for believing in me.

It is no secret that I have had considerable health issues throughout the entirety of my PhD, with daily migraines and the ensuing depression at the forefront. This thesis is in part dedicated to the organisations that have helped me during these 4 years; National Migraine Centre, Steps 2 Wellbeing, Women's Aid, and the NHS.

Without the help of the wonderful people in my life I would not be here to see the completion of my PhD, nor would I have been able to experience the exciting future ahead of me. I owe you my life, and I dedicate this thesis to you.

Chapter 1

Introduction

The Standard Model (SM) of Particle Physics has prevailed throughout the last century as the most robust description of fundamental particles and their interactions, and with the famed discovery of the Higgs boson by the CMS [7] and ATLAS [8] collaborations in 2012 the SM puzzle is seemingly complete. However, there remain many important issues that the SM fails to address, such as a quantum description of gravity, the origin of neutrino masses, and the nature of Dark Matter[1]. Perhaps the most imperative unresolved issue is the nature of Electro-Weak Symmetry Breaking (EWSB) and the origin of mass for fundamental particles. The current SM understanding of mass generation through spontaneous EWSB, i.e. the Higgs mechanism, fails to adequately explain the observed mass of the Higgs boson without introducing huge fine tuning. This is the hierarchy problem, where radiative corrections push the Higgs mass up to the Planck scale (Λ_{Pl}), 16 orders of magnitude greater than the physical Higgs mass at the weak scale.

To answer these questions we must look Beyond the Standard Model (BSM), models for which can be categorised into several common classes (e.g. Supersymmetry, Extra Dimensions, Grand Unified Theories). One of the more exciting paradigms is Technicolor, based on the introduction of *new strong dynamics* [9, 10], under which a chiral condensate forms and dynamically breaks electroweak symmetry. This provides a natural scale for mass generation and removes the fine tuning required for the SM Higgs mechanism. In the age of high energy and high luminosity colliders it is now possible to search for new physics at $\gtrsim$TeV energy scales, and Technicolor provides a wealth of phenomenology to explore at this scale.

---

[1] These topics are not discussed within this thesis

The original inception of Technicolor was a replacement of the Higgs mechanism, in fact having no Higgs boson at all[2]. Of course, observation at the LHC tells us such a particle does exist, so where does this leave Technicolor? Electroweak precision data (EWPD) also disfavours the QCD-like dymanics of the original Technicolor theory[11]. Thankfully for us, Technicolor theories with modified strong dynamics can address both of these experimental constraints, whilst retaining the richness of TeV scale phenomenology of the original Technicolor. These well motivated Walking Technicolor (WTC) models contain a new strong coupling α_S, modified to include a very slowly running ('walking') regime between the Technicolor scale Λ_{TC} and some high energy Extended Technicolor scale Λ_{ETC}[12, 13, 14, 15, 16]. The weak scale phenomenology of WTC includes a composite spin-0 resonance consistent with the observed Higgs boson, providing a naturally generated Higgs mass and an interesting potential nature for the Higgs boson. The phenomenology also includes multiple composite triplets of spin-1 resonances around the TeV scale, making WTC a prime candidate for experimental searches.

By studying physics at TeV scale colliders, we can probe the WTC paradigm, the nature of mass generation, and provide insight into the nature of the Higgs boson itself. Through such searches we hope to provide an answer as to the current potential of WTC as a solution to the hierarchy problem, as well as predict the future of Technicolor in the high luminosity LHC era and beyond.

The structure of this introduction will be as follows; In section 1.1 the SM gauge sector, the Higgs mechanism for spontaneous electroweak symmetry breaking (SEWSB), and the hierarchy problem are detailed. The mechanism of dynamical EWSB (DEWSB) as observed in the QCD sector is discussed in 1.2, along with the scaled-up QCD model of Technicolor in the pre-Higgs discovery era. Finally the evolution of the DEWSB models from running to walking dynamics is introduced and discussed in section 1.3.

The remainder of this thesis is structured as follows; In chapter 2 the Next-to-Minimal Walking Technicolor model (NMWT) at the level of the low-energy effective Lagrangian is introduced and its parameter space discussed in detail. Chapter 3 details the physical spectrum of NMWT and how it is obtained from explicit diagonalisation of mass matrices in the model. The phenomenology of neutral resonances (mass spectra, branching ratios, cross sections etc.) is explored in detail in chapter 4. In chapter 5 we update the

---

[2] There does exist a composite scalar in QCD-like Technicolor, equivalent to the QCD σ meson, however it has mass$\gg M_h$ and therefore cannot be identified as the observed Higgs

Drell-Yan dilepton limits on the NMWT parameter space for LHC@13TeV, $36fb^{-1}$, at which we also produce the first limits on NMWT from neutral and charged resonances in VV/Vh channels. In chapter 6 the spectra of Walking Technicolor models are calculated from a top-down perspective using a Holographic model, and projected into the NMWT parameter space to explore the current capacity of the LHC to probe such models. In chapter 7 a method of predicting dilepton limits at future colliders (HLLHC, 27TeV LHC, 100TeV FCC) is detailed and validated, and projected limits on NMWT for these collider searches are presented and discussed in the context of both bottom-up (effective $\mathcal{L}$) and top-down (holographic model) constructions of Walking Technicolor. Finally, we conclude with chapter 8, ultimately determining the future of Walking Technicolor in the LHC era and beyond.

1.1 Standard Model of Particle Physics

Introduction to SM Gauge Interactions

The history of the Standard Model (SM) is an interesting one; being the most successful and experimentally consistent theory of fundamental particle interactions to date and yet still lacking the satisfying resolutions to its problems, such as the hierarchy problem associated with the Higgs boson. To understand where the hierarchy problem and electroweak symmetry breaking (EWSB) enter in to the SM, it is helpful to recount the history of gauge interactions in the SM.

The Standard Model is a gauge theory describing interactions under the strong, electromagnetic and weak forces. Overall the theory has the gauge structure $SU(3)_C \otimes SU(2)_L \otimes U(1)_Y$, where C, L, Y represent colour charge, left-handedness, and hypercharge respectively. Interactions are mediated by spin-one gauge bosons corresponding to the generators of the relevant symmetry group. Let us briefly discuss the gauge sector of the strong force before giving a detailed overview of the electroweak gauge sector.

The strong force is mediated by eight gluon fields, G^a_μ where $a = 1, \ldots, 8$, corresponding to the 3x3 matrix generators of the fundamental representation of the $SU(3)$ group,

$$[t]^a_{ij} = \frac{\lambda^a}{2}, \tag{1.1}$$

where λ^a are the Gell-Mann matrices [17]. These generators follow the relations

$$Tr[t^a t^b] = \frac{\delta_{ab}}{2}, \quad [t^a, t^b] = i f^{abc} t_c, \tag{1.2}$$

where f^{abc} are the antisymmetric structure constants of $SU(3)_C$. As QCD is a non-abelian gauge theory, the field strength tensor can be constructed from the following combination of gluon fields;

$$G^a_{\mu\nu} = \partial_\mu G^a_\nu - \partial_\nu G^a_\mu + g_S f^{abc} G^b_\mu G^c_\nu, \tag{1.3}$$

where g_S is the coupling strength of the strong force interactions.

Testing this field strength tensor under $SU(3)$ transformations will provide the appropriate kinetic term for the Lagrangian. The $SU(3)_C$ group contains set of 3x3 Unitary matrices with determinant 1, $U = e^{it^a \theta^a_C}$, where θ^a_C are arbitrary parameters. Applying an infinitesimal $SU(3)_C$ transformation to the field strength tensor,

$$G^a_{\mu\nu} \mapsto U^\dagger G^a_{\mu\nu} U \tag{1.4}$$

is invariant *if* the gluon field transforms as

$$G^a_\mu \mapsto G^a_\mu - \frac{1}{g_S} \partial_\mu (\delta\theta^a) - f_{abc} \delta\theta^b G^c_\mu. \tag{1.5}$$

This allows us to safely construct the gauge invariant kinetic Lagrangian for QCD,

$$\begin{aligned} \mathcal{L}^{kin}_{QCD} &= -\frac{1}{2} \mathtt{Tr}[G^{\mu\nu} G_{\mu\nu}] \qquad (1.6) \\ &= -\frac{1}{4} G^{\mu\nu}_a G^a_{\mu\nu}, \qquad (1.7) \end{aligned}$$

which, in addition to the usual 2-point gauge boson interactions, contains both cubic and quartic gluon self-coupling terms. If we try to add in a mass term for the gluon, e.g. $\frac{1}{2} m_G G^\mu_a G^a_\mu$, under the transformations given above this term breaks the gauge symmetry of $SU(3)_C$. Thus, the gluon must be massless.

As proposed by Glashow, Weinberg, and Salam, the electromagnetic and weak sectors can be considered together in a unified electroweak theory [18, 19, 20]. Consider the case of exact $SU(2)_L \otimes U(1)_Y$ symmetry; each group has its own set of fields corresponding to the generators of said group. The $U(1)_Y$ group contains one generator which can be identified as hypercharge, Y, associated with a field B_μ. The $SU(2)_L$ group contains three generators T^a, $a = 1, 2, 3$, corresponding to three fields W^a_μ. These $SU(2)_L$ generators are related simply to the 2x2 Pauli matrices by a factor of 1/2,

$$T^1 = \frac{1}{2}\begin{pmatrix} 0 & 1 \\ 1 & 0 \end{pmatrix}, \quad T^2 = \frac{1}{2}\begin{pmatrix} 0 & -i \\ i & 0 \end{pmatrix}, \quad T^3 = \frac{1}{2}\begin{pmatrix} 1 & 0 \\ 0 & -1 \end{pmatrix}. \tag{1.8}$$

The generators follow the commutation relations

$$[T^a, T^b] = i\epsilon^{abc}T_c, \quad [Y, Y] = 0, \quad [T^a, Y] = 0, \tag{1.9}$$

and the field strength tensors of the associated fields B_μ and W^a_μ take the form

$$\begin{aligned} B_{\mu\nu} &= \partial_\mu B_\nu - \partial_\nu B_\mu, \\ W^a_{\mu\nu} &= \partial_\mu W^a_\nu - \partial_\nu W^a_\mu - g_2 \epsilon^{abc} W^b_\mu W^c_\nu, \end{aligned} \tag{1.10}$$

where ϵ^{abc} are the antisymmetric Levi-Civita structure constants and g_2 is the dimensionless gauge coupling associated with $SU(2)_L$.

The $B_{\mu\nu}$ field strength transforms as an abelian theory (e.g QED), so the local gauge transformation of B_μ is simple to write down, whereas $W^a_{\mu\nu}$ is non-abelian so should transform similarly to the QCD field strength under $SU(2)_L$ transformations. Thus we can see that under infinitesimal transformations the $SU(2)_L$ and $U(1)_Y$ fields transform locally as

$$\begin{aligned} B_\mu &\mapsto B_\mu + \frac{1}{g_1}\partial_\mu \theta_Y(x) \\ W^a_\mu &\mapsto W^a_\mu + \frac{1}{g_2}\partial_\mu \theta^a_L(x) + \epsilon^{abc} W^b_\mu \theta^c_L(x), \end{aligned} \tag{1.11}$$

where g_1, g_2 are the dimensionless gauge couplings associated with $U(1)_Y$ and $SU(2)_L$ respectively.

A first hint of unification of the electromagnetic and weak forces can be seen in the relationship between generators of each group and the properties (quantum numbers) they represent. The QED generator Q and $U(1)_Y$ generator Y represent electric charge and hypercharge respectively, where the generators of $SU(2)_L$ represent isospin. Of particular importance is the third component of isospin, i.e T^3, which is the conserved quantity in gauge transformations of a fermion field under $SU(2)_L$. The weak isospin and the hypercharge are related through the electromagnetic charge as

$$Q = T^3 + \frac{Y}{2} \tag{1.12}$$

Thus the gauge invariant kinetic Lagrangian for the electroweak sector is

$$\mathcal{L}^{kin}_{EW} = -\frac{1}{4} W^{\mu\nu}_a W^a_{\mu\nu} - \frac{1}{4} B^{\mu\nu} B_{\mu\nu}. \tag{1.13}$$

As in the case of the QCD bosonic lagrangian (equation 1.7), we are forbidden from writing down mass terms for the B^μ and W^μ_a fields if the $SU(2)_L \otimes U(1)_Y$ gauge symmetry is to remain intact. However, the bosons of the weak force (W^+, W^-, Z) have been experimentally observed to be massive, so how does one reconcile the existence of massive gauge bosons with a fully invariant Lagrangian? There must be some mechanism to break $SU(2)_L \otimes U(1)_Y$ gauge symmetry whilst preserving the symmetry of the Lagrangian.

1.1.1 Electroweak Symmetry Breaking in the SM

The SM achieves this feat by introducing a complex scalar $SU(2)$ doublet - the Higgs field - that breaks electroweak symmetry spontaneously, inducing invariant mass terms for the $W^{+/-}$ and Z bosons whilst maintaining a massless photon and a fully gauge invariant Lagrangian. This Higgs doublet is Φ,

$$\Phi = \begin{pmatrix} \phi^+ \\ \phi^0 \end{pmatrix}, \tag{1.14}$$

where ϕ^+, ϕ^0 are the complex scalar fields

$$\phi^+ = \frac{1}{\sqrt{2}}(\phi^1 + i\phi^2), \quad \phi^0 = \frac{1}{\sqrt{2}}(\phi^3 + i\phi^4). \tag{1.15}$$

This Higgs doublet enters into the SM Lagrangian with a scalar potential part and a gauge-interacting part,

$$\mathcal{L}_{Higgs} = (D^{\mu}\Phi)^{\dagger}(D_{\mu}\Phi) - V(\Phi). \tag{1.16}$$

The covariant derivative of Φ is

$$D_{\mu}\Phi = (\partial_{\mu} + i\frac{g_1}{2}YB_{\mu} + ig_2T^aW_{\mu}^a)\Phi, \tag{1.17}$$

where B_{μ} and W_{μ}^a are the $U(1)_Y$ and $SU(2)_L$ gauge fields introduced previously.

The mechanism for spontaneous symmetry breaking can be understood through the form of the Higgs potential

$$V(\Phi) = \mu^2\Phi^{\dagger}\Phi + \lambda(\Phi^{\dagger}\Phi)^2, \tag{1.18}$$

where $\lambda > 0$ to ensure the Higgs potential is bounded from below, therefore ensuring a state of minimum energy is possible.

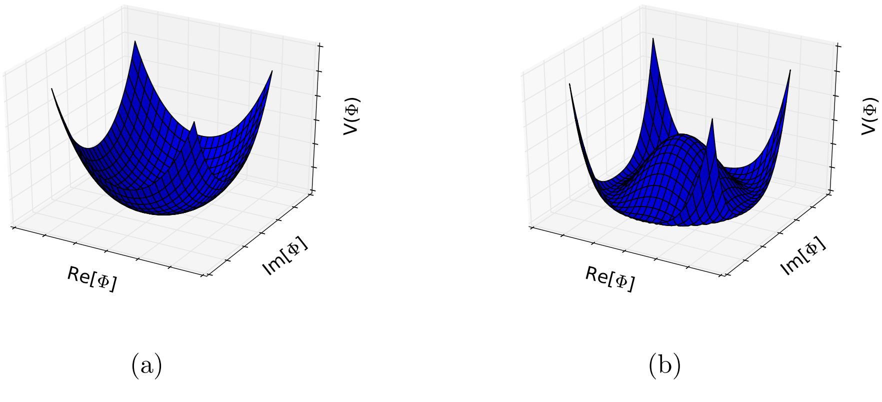

(a) (b)

Figure 1.1: Form of the Higgs potential $V(\Phi)$ in the case of a) $\mu^2 > 0$, b) $\mu^2 < 0$.

Two cases now exist for the form of the potential, the case of $\mu^2 > 0$ (Figure 1.1a) and that of $\mu^2 < 0$ (Figure 1.1b). When we take $\mu^2 > 0$, the Higgs potential $V(\Phi)$ has a unique minimum, the trivial state $\Phi = 0$. Here, electroweak symmetry is preserved, and the Higgs does not generate masses for the EW gauge bosons.

The case of $\mu^2 < 0$ is more interesting, as now the ground state no longer lies at $\Phi = 0$ but instead exhibits a degenerate 'ring' of ground states at which the vacuum acquires a non-zero expectation value. At the potential minimum,

$$\Phi^\dagger \Phi = -\frac{\mu^2}{2\lambda} = \frac{v^2}{2}, \tag{1.19}$$

where v is identified as the vacuum expectation value (vev). Only one of these ϕ^a $(a = 1, \ldots, 4)$ will acquire a vev, and consequently the choice of vacuum state will spontaneously break EWS.

For any choice of vacuum state, the $U(1)_{EM}$ symmetry is preserved, so the symmetry breaking pattern is then

$$SU(2)_L \otimes U(1)_Y \to U(1)_{EM}. \tag{1.20}$$

In light of this, let us make the choice of vacuum state as where $\langle \phi \rangle^{1,2,4} = 0$ and $\phi^3 = v$,

$$\langle \Phi \rangle = \frac{1}{\sqrt{2}} \begin{pmatrix} 0 \\ v \end{pmatrix}. \tag{1.21}$$

We can also introduce a real scalar field h whose vev is $\langle h \rangle = 0$, which enters in to the scalar doublet as

$$\Phi = \frac{1}{\sqrt{2}} \begin{pmatrix} 0 \\ v + h \end{pmatrix}. \tag{1.22}$$

From the Higgs potential we have found the mechanism for spontaneous breaking of the $SU(2)_L \otimes U(1)_Y$ symmetry, but what of the W and Z masses? According to Goldstone's theorem, as there are three broken global symmetries there will also appear three massless Goldstone bosons [21, 22, 23], however as these are unphysical degrees of freedom, we will consider the mass generation mechanism in the Unitary gauge, so we can neglect them[3]. Let us now consider the kinetic part of the Higgs Lagrangian 1.16,

$$(D^\mu\Phi)^\dagger(D_\mu\Phi) = \frac{1}{\sqrt{2}}\begin{pmatrix}0 & v\end{pmatrix}\left(i\frac{g_1}{2}YB_\mu + ig_2T^aW^a_\mu\right)\left(-i\frac{g_1}{2}YB^\mu - ig_2T^aW^{a,\mu}\right)\frac{1}{\sqrt{2}}\begin{pmatrix}0\\ v\end{pmatrix} \tag{1.23}$$

Substituting the generators of the W^a_μ fields from equation 1.8 and performing the matrix multiplication, this becomes

$$(D^\mu\Phi)^\dagger(D_\mu\Phi) = \frac{v^2}{8}[g_2^2(W_1^2 + W_2^2) + (g_1YB_\mu - g_2W_3)^2]. \tag{1.24}$$

We can recast this in terms of physical gauge bosons, identifying that the W_1, W_2 components can be re-written as

$$W^\pm = \frac{1}{\sqrt{2}}(W_1 \mp iW_2), \tag{1.25}$$

we can then replace

$$g_2^2(W_1^2 + W_2^2) = 2g_2^2W^+W^-. \tag{1.26}$$

The remaining fields can be rewritten as

$$(g_1YB_\mu - g_2W^3)^2 = \begin{pmatrix}W^3 & B_\mu\end{pmatrix}\begin{pmatrix}g_2^2 & -g_1g_2Y\\ -g_1g_2Y & g_1^2\end{pmatrix}\begin{pmatrix}W^3\\ B_\mu\end{pmatrix}, \tag{1.27}$$

and setting the hypercharge $Y = 1$ we can identify the physical photon field, A_μ, and physical Z boson field, Z_μ, as solutions to the eigenvalue equation formed from equation 1.27,

$$A_\mu = \frac{(g_1W_3 + g_2B_\mu)}{\sqrt{g_1^2 + g_2^2}} \tag{1.28}$$

$$Z_\mu = \frac{(g_2W_3 - g_1B_\mu)}{\sqrt{g_1^2 + g_2^2}}. \tag{1.29}$$

---

[3] In t'Hooft-Feynman gauge the Goldstone bosons are 'eaten' by the physical gauge bosons, becoming the longitudinal components of the W's and Z

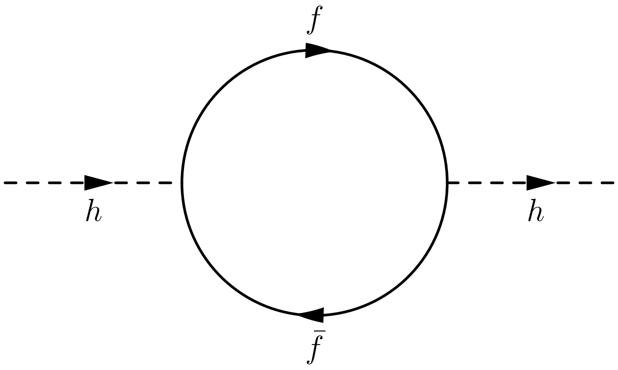

Figure 1.2: 1-loop fermion correction to the Higgs propagator.

Thus equation 1.23 can be written in terms of the physical gauge boson fields as

$$(D^{\mu}\Phi)^{\dagger}(D_{\mu}\Phi) = \frac{v^2}{8}[2g_2^2 W^+W^- + (g_1^2 + g_2^2)Z_{\mu}^2 + 0A_{\mu}^2], \tag{1.30}$$

where each term's coefficient corresponds to the mass-squared of the physical $W^{\pm}$ and Z, with of course the massless photon γ.

1.1.2 Hierarchy Problem

The mechanism of EWSB providing the correct EW gauge boson masses and the discovery of a 125GeV Higgs boson at the LHC provide a compelling argument for the Higgs mechanism as the mechanism of mass generation in Nature. Let us assume then that this is the complete picture of strong, EM, and weak interactions, and the SM is an effective field theory of some high-scale physics, specifically that it is valid up to the Planck scale Λ_{Pl}. This implies that there exist two fundamental scales $\Lambda_{EW} \sim \mathcal{O}(10^2)$GeV and $\Lambda_{Pl} \sim \mathcal{O}(10^{18})$GeV, why then is their separation so large? This is the hierarchy problem, and we discuss here its implications for the naturalness of the SM through the lens of radiative corrections to the Higgs mass[24, 25, 26].

Let us examine the 1-loop fermionic corrections to the Higgs propagator (Figure 1.2). Recalling that the neutral Higgs field in the doublet of equation 1.22 takes the form $\phi = (h{+}v)/\sqrt{2}$, the generic Lagrangian for Higgs-fermion-

fermion interactions with a Yukawa coupling λ_f is

$$\mathcal{L}_{\phi f\bar{f}} = -\frac{\lambda_f}{\sqrt{2}}(h\bar{f}f + v\bar{f}f). \tag{1.31}$$

The tree-level mass of the fermion is then $m_f = \lambda_f v/\sqrt{2}$. We can compute the two-point function of the Higgs diagram in Figure 1.2,

$$i\Pi^f_{hh}(0) = (-)\int \frac{d^4k}{(2\pi)^4}\mathtt{Tr}\left[\left(-i\frac{\lambda_f}{\sqrt{2}}\right)\frac{i}{\not{k} - m_f}\left(-i\frac{\lambda_f}{\sqrt{2}}\right)\frac{i}{\not{k} - m_f}\right] \tag{1.32}$$

$$= -2\lambda_f^2\int \frac{d^4k}{(2\pi)^4}\left[\frac{1}{k^2 - m_f^2} + \frac{2m_f^2}{(k^2 - m_f^2)^2}\right]. \tag{1.33}$$

The first term in this correlator is divergent, which is not an issue as one can remove the divergences using regularisation techniques such as dimensional regularisation or introducing some cut-off scale Λ, at which new physics appears. Even if one does not put the cut-off Λ in the integration by hand, Λ still arises upon integration as in the UV, one runs in to a Landau pole in the QED coupling, at which charged particles would form new bound states - i.e introducing new physics at the scale Λ. Once the divergences are dealt with, there still remains a finite correction to the squared Higgs mass proportional to Λ^2,

$$\Delta M_h^2(f) = -\frac{\lambda_f^2\Lambda^2}{8\pi^2}. \tag{1.34}$$

In the scenario in which there is no new physics between the EW scale and the Planck scale, the cut-off is Λ_{Pl}, so the 1-loop fermion contribution to the Higgs propagator results in a mass correction of $\Delta M_h^2 \sim \mathcal{O}(\Lambda_{Pl}^2)$. There are equivalent diagrams to Figure 1.2 for bosonic loops which exhibit this Λ dependence with the opposite sign to the fermion correction, so there is some cancellation between the fermionic and bosonic loops. However, these diagrams enter with different vertex coupling strengths, and there remains a finite correction to the squared Higgs mass proportional to Λ^2. This is a disastrous result for the naturalness of the SM, the Higgs has been observed at $M_h^{phys} \sim \Lambda_{EW}$ so one must fine-tune the model to one part in 10^{28} to cancel out the $\mathcal{O}(\Lambda_{Pl}^2)$ mass-squared correction at 1-loop level.

This huge level of fine-tuning is already a hint that the SM is an incomplete description of fundamental physics. Additionally, the sensitivity of the Higgs to physics at the cut-off scale suggests that the appearance of new physics at $\Lambda_{NP} \sim \mathcal{O}(\text{TeV})$ would naturally solve the hierarchy problem[27, 28].

1.2 Technicolor

When discussing models of dynamical electroweak symmetry breaking (DEWSB), one should briefly introduce the pre-Higgs era motivation and formulation of the original Technicolor paradigm. Although this is roundly excluded by a number of experimental factors, not least of which is the discovery of a Higgs boson at $M_h = 125\text{GeV}$, it is worthwhile to understand the groundwork laid by this pioneering approach to solving the hierarchy problem. [29, 30] The origin of Technicolor stems from the motivation to explain EWSB and the origin of fundamental particle mass without invoking the Higgs mechanism, taking inspiration from observations already made in the QCD sector[31]. In fact, in the absence of a Higgs mechanism the EW symmetry is still broken, instead breaking due to chiral symmetry breaking in QCD. Here we will detail this mechanism in the low-scale QCD theory, and discuss the origin of Technicolor as a QCD-like theory, before discussing the modern interpretations of new strong dynamics.

1.2.1 Dynamical Symmetry Breaking in QCD

Consider the low energy behaviour of a massless QCD theory, where only quarks with mass $m_q \ll \Lambda_{QCD}$ contribute. This discussion follows closely that of section 19.3 of Peskin and Schroeder[32]. Although $m_s < \Lambda_{QCD}$, it is significantly heavier than the u, d quarks and as such we do not include it in this discussion. In the massless u, d limit the QCD Lagrangian is

$$\mathcal{L}^{QCD} = -\frac{1}{4} G_a^{\mu\nu} G^a_{\mu\nu} + i\bar{q}\not{D}q, \tag{1.35}$$

where

$$D_\mu = \partial_\mu + i g_S t^a A^a_\mu, \quad q = \begin{pmatrix} u \\ d \end{pmatrix}. \tag{1.36}$$

This Lagrangian contains no mixing of left and right handed terms, and is invariant separately under left and right unitary transformations of the form

$$\begin{pmatrix} u \\ d \end{pmatrix}_L \to U_L \begin{pmatrix} u \\ d \end{pmatrix}_L, \quad \begin{pmatrix} u \\ d \end{pmatrix}_R \to U_R \begin{pmatrix} u \\ d \end{pmatrix}_R. \tag{1.37}$$

Thus in the limit of low energy massless QCD the Lagrangian exhibits a chiral symmetry under the symmetry group $SU(2)_L \otimes SU(2)_R \otimes U(1)_V \otimes U(1)_A$[4]. By definition we are in the regime in which the coupling between quarks is strong, as such the energy expenditure for creating bound states is actually less than that of maintaining free, unbound quarks, and so the ground state of QCD forms a condensate of quark-antiquark pairs each with zero total and angular momentum. Naturally then the vacuum state is described by the non-zero vacuum expectation value

$$\langle \bar{q}q \rangle = \langle 0 | \bar{q}_L q_R + \bar{q}_R q_L | 0 \rangle \neq 0, \quad q_{L/R} = \frac{1 \mp \gamma^5}{2} \begin{pmatrix} u \\ d \end{pmatrix}. \tag{1.38}$$

As this describes the ground state of QCD and explicitly contains interactions between left-handed and right-handed fields, this means that the chiral symmetry must be broken by the formation of this quark condensate[33], with a chiral symmetry breaking pattern of

$$SU(2)_L \otimes SU(2)_R \to SU(2)_V. \tag{1.39}$$

In this theory the vector symmetries are preserved and transform with $U_L = U_R$ for vector currents, however the axial vector currents break the symmetry and as a result generate massless Goldstone bosons (akin to the Higgs mechanism described in section 1.1.1)[22]. These are identified as the pions, which are massless in the $m_u = m_d = 0$ limit but do gain non-zero mass from adding explicit symmetry breaking mass terms to the QCD Lagrangian of equation 1.35. These pions form an isospin triplet π^a, which are defined by the pion decay constant f_π through the important relation

$$\langle 0 | j_\mu^{5a} | \pi^b \rangle = f_\pi q_\mu \delta^{ab}, \tag{1.40}$$

where j_μ^{5a} are the axial isospin currents with a, b as the isospin indices, and $f_\pi = 93$MeV as measured experimentally.

---

[4] This is generalised to $SU(N_f)_L \otimes SU(N_f)_R \otimes U(1)_V \otimes U(1)_A$

The main result of this chiral symmetry breaking is that as the vacuum state is a condensate of quark bound-states, any massless quark moving through the vacuum will gain an effective mass proportional to $\langle \bar{Q}Q \rangle^{\frac{1}{3}}$. In the two flavour approximation we have discussed here, the quark condensate takes the value $\langle \bar{u}u + \bar{d}d \rangle \simeq (250\text{MeV})^3$[31]. This gives a neat explanation of why the proton/neutron masses are much larger than the sum of constituent valence quarks, even in the case of massless u, d quarks.

Additionally, if one were to remove the Higgs mechanism entirely, then this QCD chiral condensate $\langle \bar{u}u + \bar{d}d \rangle$ does still break electroweak symmetry[31]. In this mechanism, the chiral condensate induced EW symmetry breaking generates Goldstone bosons that become the longitudinal modes of the W, Z bosons. The dynamically generated mass for the W is then

$$M_W = \frac{g_2 f_\pi}{2} \sim 29\texttt{MeV}. \tag{1.41}$$

Although this is significantly smaller than the measured W mass ($M_W \simeq$ 80.4MeV), it does provide an enticing example of how EW symmetry could be broken by the dynamics of a theory with strongly interacting fundamental fermions.

1.2.2 Technicolor as scaled-up QCD

With the inspiration from dynamical symmetry breaking and mass generation already observed in the QCD sector, the explanation for EWSB as a consequence of new strong dynamics at the TeV scale emerged in the form of Technicolor[29, 30]. In direct analogy to the low-energy limit of QCD with two flavours, the simplest Technicolor model is an $SU(N_{TC}) = SU(3)$ gauge theory with two techniquarks in the fundamental of $SU(N_{TC})$,

$$\begin{pmatrix} U \\ D \end{pmatrix}_L, \quad U_R, \quad D_R, \tag{1.42}$$

which in the massless limit exhibit a chiral $SU(2)_L \otimes SU(2)_R$ symmetry.

These techniquarks interact strongly around the scale of the theory, Λ_{TC}, as such the vacuum state of the theory is filled with a condensate of techni-quark bound states

$$\langle \bar{U}_L U_R \rangle = \langle \bar{D}_L D_R \rangle \sim \Lambda_{TC}^3, \tag{1.43}$$

which spontaneously breaks the chiral symmetry in the familiar pattern of

$$SU(2)_L \otimes SU(2)_R \otimes U(1)_V \to SU(2)_V \otimes U(1)_V. \tag{1.44}$$

As in the QCD model, the spontaneously broken chiral symmetry produces three pions π^+, π^-, π^0 with a new pion decay constant F_π, which become the longitudinal modes of the $W^\pm, Z$ bosons. The W bosons acquire a mass of

$$M_W = \frac{g_2 F_\pi}{2}, \tag{1.45}$$

where setting $F_\pi = v = 246\text{GeV}$ recovers the correct EW mass spectrum.

Additionally to inducing EWSB from a dynamical origin and providing a natural scale for generation of gauge boson masses, the Technicolor model also contains a spectrum of techni-mesons at the TeV scale in analogy to the ρ, a_1 mesons in QCD. This provides a rich phenomenology that could be accessed by high-energy collider experiments, and which (at the time of Technicolor's origin in the 70's) would not yet have been observed[5].

Despite its initial appeal as a solution to the hierarchy problem via DEWSB, the scaled-up QCD version of Technicolor is roundly excluded for a number of reasons. The most obvious failing of new QCD-like strong dynamics is that it completely replaces the Higgs mechanism, and there is no particle resembling the Higgs - the composite scalar mode that is generated (the techni-σ) is significantly heavier than the Higgs that has famously been discovered at the LHC[8, 7]. The model is also strongly disfavoured by electroweak precision data (EWPD)[11], and attempts to provide mass to the SM fermions with Extended Technicolor (ETC) sectors result in flavour changing neutral currents (FCNC) which are highly constrained[34, 35]. In light of this plethora of experimental evidence against scaled-up QCD dynamics, it may seem that DEWSB by formation of a techniquark condensate is not the correct mechanism for mass generation. However, there is a surprisingly elegant solution to all of these aforementioned issues in the form of new strong dynamics with a *modified running coupling*, i.e Walking Technicolor.

---

[5] The purpose of this statement is to provide further motivation for new strong dynamics over models of Supersymmetry, which predicts the existence of new particles with equal mass to those SM particles already observed at experiment

1.3 Walking Technicolor

The general idea of Walking Technicolor (WTC) paradigms is that there are two new fundamental scales of physics, Λ_{TC} ($\sim$TeV scale) and Λ_{ETC} (some high scale), between which the running α_{TC} of the new strong force is modified to be 'walking' (very slowly running). WTC [36, 37, 38, 39, 40, 41] and its recent developments [42, 13, 16, 14, 15, 43] provide a very compelling candidate for the underlying theory of Nature.

To demonstrate the need for a modified running behaviour of the new strong coupling α_{TC}, one should inspect the implications for SM fermion mass generation for running and walking Technicolor models. In both scenarios, the SM fermion masses originate from the ETC interactions, where technifermions and SM fermions couple and interact via some ETC gauge boson of mass M_{ETC} of order $\mathcal{O}(\Lambda_{ETC})$[44]. When the chiral techni-quark condensate $\langle\bar{Q}Q\rangle(=\langle\bar{U}U\rangle=\langle\bar{D}D\rangle)$ is formed, these fermion/technifermion interactions generate a fermion mass of the form

$$m_f \approx \frac{g^2_{ETC}}{M^2_{ETC}}\langle\bar{Q}Q\rangle_{ETC}, \tag{1.46}$$

where g_{ETC} is the coupling strength of the interaction, $\langle\bar{Q}Q\rangle_{ETC}$ is the value of the chiral condensate evaluated at the scale Λ_{ETC}.

The condensate evaluated at the ETC can be related to the TC scale condensate via

$$\langle\bar{Q}Q\rangle_{ETC} = \langle\bar{Q}Q\rangle_{TC}\exp\left(\int_{\Lambda_{TC}}^{\Lambda_{ETC}}\frac{d\mu}{\mu}\gamma(\alpha_{TC}(\mu))\right), \tag{1.47}$$

where γ is the anomalous dimension of the technifermion mass operator. Herein lies the difference between models with a QCD-like α_{TC} and those with a regime of walking α_{TC}[6].

In Technicolor models resembling a scaled-up QCD, between the scales Λ_{TC} and Λ_{ETC} the coupling α_{TC} runs with scale μ as

$$\alpha_{TC}(\mu) \propto \frac{1}{\ln\mu}, \tag{1.48}$$

---

[6] Note here that the subscript α_{TC} does not refer to the specific value of α at the TC scale, rather a label identifying this as the coupling of a new strong force in a general Technicolor model

which enhances the chiral condensate by a factor of

$$\langle \bar{Q}Q \rangle_{ETC} \sim \langle \bar{Q}Q \rangle_{TC} \ln \left(\frac{\Lambda_{ETC}}{\Lambda_{TC}} \right)^{\gamma}, \tag{1.49}$$

and leads to the anomalous dimension $\gamma \propto \alpha_{TC}(\mu)$. The logarithmic enhancement along with the running of the anomalous dimension infers that the enhancement to the chiral condensate from the ETC scale physics is negligible in comparison to the condensate at the TC scale. We can therefore directly substitute the TC scale condensate $\langle \bar{Q}Q \rangle_{TC} \sim \Lambda^3_{TC}$[45, 46, 47, 48] into the fermion mass relation (equation 1.46) to find

$$m_f \approx \frac{g^2_{ETC}}{M^2_{ETC}} \Lambda^3_{TC}. \tag{1.50}$$

This approximation must be considered in the context of FCNCs, which are severely experimentally constrained, most strongly by potential $|\Delta S| = 2$ interactions and their contributions to the $K_L - K_S$ mass difference (see [49, 44] for details). The main point here is that the mass/coupling ratio of the ETC gauge boson must be pushed up to at least the level of $\gtrsim \mathcal{O}(600\text{TeV})$, greatly suppressing the SM fermion mass generated by the ETC interaction. With this approximation for the fermion masses, one cannot hope to generate the correct fermion mass of even the strange quark, and certainly not the top quark!

One can solve the problem of avoiding problematic FCNCs while generating sufficient masses for the SM fermions if the contribution to the techniquark condensate from the ETC sector is enhanced. This is the motivation for modifying the α_{TC} coupling such that it *walks* (i.e very slowly runs) in the regime of $\Lambda_{TC} < \mu < \Lambda_{ETC}$, where the walking behaviour approaches a conformal fixed point $\alpha^*_{TC} = (g^*_{TC})^2/4\pi$ near the scale Λ_{TC}. The chiral condensate then receives an enhancement from the ETC sector of

$$\langle \bar{Q}Q \rangle_{ETC} \sim \langle \bar{Q}Q \rangle_{TC} \left(\frac{\Lambda_{ETC}}{\Lambda_{TC}} \right)^{\gamma(\alpha^*_{TC})}, \tag{1.51}$$

where the anomalous dimension is evaluated at α^*_{TC} and is approximately constant across this energy range. This constant $\mathcal{O}(1)$ anomalous dimension, along with the now linear enhancement of the chiral condensate, significantly

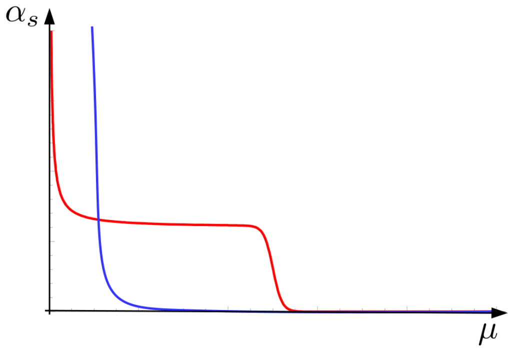

Figure 1.3: Visual representation of *running* (blue) and *walking* (red) dynamics of $\alpha_S = \alpha_{TC}$ as a function of momentum μ.

enhances $\langle \bar{Q}Q \rangle_{ETC}$ above the ETC contribution with QCD-like running coupling dynamics. This relieves tension with FCNCs as the interaction between SM fermions and technifermions is enhanced while interactions between only SM fermions is unaffected.

The concept of modified Technicolor with a walking coupling regime up to an ETC scale was originated and explored initially from 1987[50, 51, 52, 53, 54, 55, 56, 57, 53, 58, 59, 60], with a revival in interest from 2005 with the demonstration that certain Walking Technicolor theories can be physically viable within limits from FCNCs and EWPD[61, 13].

In Figure 1.3 the general picture for the coupling $\alpha_{TC}(\mu)$ in QCD-like Technicolor and Walking Technicolor models. For WTC, the new strong force is QCD-like up to Λ_{TC}, where the walking behaviour begins up to some high scale Λ_{ETC}, after which the theory runs again and is asymptotically free. The exact physics of the ETC sector is not known, and to account for the generations of SM fermions there should be some staggered set of scales which provide mass to each generation. For the purpose of exploring BSM physics from a phenomenological perspective, we do not need to know the exact ETC theory, we can simply take the analysis of the modified running coupling and assume that the correct ETC theory does provide a dynamical origin of the SM fermion masses.

We will discuss in detail the simplest model of WTC in chapter 2, first let us make some final statements on the advantages of Walking dynamics. The technimeson spectrum of WTC models contain not only ρ and A mesons (analogous to the QCD ρ and a_1), but also a composite scalar meson analogous to the QCD σ. Identifying the scale of WTC as $\Lambda_{TC} \sim 1\text{TeV}$ and the technipion decay constant F_π as the SM Higgs vev $v = 246\text{GeV}$, the dynamical mass of the σ meson can be lighter than $M_\rho \simeq \Lambda_{TC}$. Accounting for negative corrections from top loops, the σ mass naturally is found to be $M_\sigma = M_h = 125\text{GeV}$[62]. Thus WTC models naturally generate a composite scalar consistent with the observed Higgs, removing the hierarchy problem and providing a dynamical origin of mass.

Chapter 2

Next-to-Minimal Walking Technicolor Model

With the concepts behind Walking Technicolor (WTC) firmly in place (1.3), the models underpinning this mechanism of DEWSB can be constructed. As with all Beyond the Standard Model (BSM) theories, one should always begin with the most minimal model possible. In the case of WTC, there are two possibilities available as ideal candidate models, each with their own unique chiral symmetry breaking pattern. The first is Minimal Walking Technicolor (MWTC)[42], built on an $SU(4)$ global symmetry with the symmetry breaking pattern $SU(4) \to SO(4)$. Despite its name, MWTC is actually not the most minimal model of WTC in terms of additional particle content. Both MWT and NMWT have $N_f = 2$ flavours of Dirac techni-fermions in the two index symmetric representation of $SU(N_c)$, with $N_c = 2$ and $N_c = 3$ respectively. The two-colour model suffers from a Witten anomaly as there are an odd number of EW doublets, so the model must introduce a new leptonic EW doublet to remedy this[63, 42]. Additionally, the global symmetry breaking to $SO(4)$ generates nine Goldstone bosons, three of which become the longitudinal modes of W, Z, and the remainder are expected to obtain mass from the dynamics of the ETC sector[64, 34, 35, 65].

Therefore, the simplest model with respect to additional composite particles is Next to Minimal Walking Technicolor (NMWT). The model has an $SU(2)_L \otimes SU(2)_R$ global symmetry, whose chiral symmetry breaking pattern is

$$SU(2)_L \otimes SU(2)_R \otimes U(1)_V \to SU(2)_V \otimes U(1)_V. \tag{2.1}$$

NMWT has the advantage of exhibiting near-conformal behaviour in the new strong force coupling with just two Dirac flavours[66]. The breaking to $SU(2)_V$ generates only the Goldstone bosons required for the SM EW gauge bosons, and as $N_c = 3$ there are an even number of EW doublets, so there is no Witten anomaly and no need for additional leptonic doublets. In fact the NMWT chiral symmetry breaking pattern is the minimal pattern required to generate three Goldstone bosons which become the longitudinal modes of the W, Z, the correct tree-level value for $\sin\theta_W$, and a Higgs sector resembling the SM. This means that the NMWT model can be used as a template/guideline for the greater class of Walking Technicolor theories, hence our focus on this model.

An interesting feature of the NMWT model is the presence of two triplets of techni-mesons, corresponding to new heavy spin-one resonances similar to the SM weak force triplet of $W^\pm$,Z. It is these new resonances that particularly strike our interest in this model, as will be discussed later in chapter 4.

2.1 NMWT Effective Low Energy Model

At the scale of DEWSB, Λ_{TC}, the Technicolor interactions with the electroweak sector can be investigated within an Effective Field Theory (EFT), i.e an approximate description of the model's interactions at a low energy (relative to Λ_{ETC}). Following the prescription of [67, 66], we can encode the underlying composite dynamics within a generic chiral EFT which exhibits a global $SU(2)_L \otimes SU(2)_R$ symmetry. The new heavy spin-1 triplets are represented at the level of the gauge eigenbasis as $A^\mu_{L/R}$ gauge fields under $SU(2)_{L/R}$ respectively. Identifying that the $SU(2)_L$ group here is gauged as the equivalent $SU(2)_L$ in SM weak interactions, we can see that A^μ_L transforms as a triplet under $SU(2)_L$[1], where the A^μ_R fields transform as singlets under $SU(2)_L$.

The electroweak SM fields in the gauge eigenbasis, $\tilde{W}^\mu$ and $\tilde{B}^\mu$, can then be combined with the effective L/R technicolor fields to define the chiral fields

$$C_{L\mu} \equiv A_{L\mu} - \frac{g_2}{\tilde{g}}\tilde{W}_\mu, \qquad C_{R\mu} \equiv A_{R\mu} - \frac{g_1}{\tilde{g}}\tilde{W}_\mu, \tag{2.2}$$

where g_1, g_2 are the standard coupling constants of the SM EW sector[2], and

---

[1] Analogous to the gauge triplet W^a_μ in the SM (see section 1.1)

[2] These are commonly referred to in the literature as g, g', I identify $g = g_2$ and $g' = g_2$ to avoid confusion between SM and TC nomenclature with regards to the superscript

$\tilde{g}$ is the effective coupling of the chiral TC interactions.

The lightest composite scalar resonance, identified as the Higgs H, appears alongside a triplet of pions π^a, where $a = 1, 2, 3$, as a bi-doublet field under the $SU(2)_{L/R}$ symmetries. These can be represented by the 2×2 matrix M,

$$M = \frac{1}{\sqrt{2}}[v + H + 2i\pi^a T^a], \tag{2.3}$$

where $v = \mu/\sqrt{\lambda}$ is the vev associated with the chiral symmetry breaking at the EW scale[3], and T^a are the generators of $SU(2)$ defined in equation 1.8. This Higgs mixes with the EW fields in the gauge eigenbasis through the covariant derivative of M

$$D_\mu M = \partial_\mu M + ig_1 M\tilde{B}_\mu T^3 - ig_2 \tilde{W}^a_\mu T^a M. \tag{2.4}$$

With the gauge fields defined, we can now write the gauge kinetic and gauge interaction contributions (up to dim-4 operators) to the low-energy effective Lagrangian as

$$\begin{aligned}\mathcal{L}_{boson} = &-\frac{1}{2}\mathrm{Tr}\left[\tilde{W}_{\mu\nu}\tilde{W}^{\mu\nu}\right] - \frac{1}{4}\tilde{B}_{\mu\nu}\tilde{B}^{\mu\nu} - \frac{1}{2}\mathrm{Tr}[F_{L\mu\nu}F_L^{\mu\nu} + F_{R\mu\nu}F_R^{\mu\nu}] \\ &+ m^2\mathrm{Tr}[C_{L\mu}^2 + C_{R\mu}^2] + \frac{1}{2}\mathrm{Tr}[D_\mu M D^\mu M^\dagger] - \tilde{g}^2 r_2 \mathrm{Tr}[C_{L\mu} M C_R^\mu M^\dagger] \\ &- \frac{i\tilde{g}r_3}{4}\mathrm{Tr}[C_{L\mu}(MD^\mu M^\dagger - D^\mu M M^\dagger) + C_{R\mu}(M^\dagger D^\mu M - D^\mu M^\dagger M)] \\ &+ \frac{\tilde{g}^2 s}{4}\mathrm{Tr}[C_{L\mu}^2 + C_{R\mu}^2]\mathrm{Tr}[MM^\dagger] + \frac{\mu^2}{2}\mathrm{Tr}[MM^\dagger] - \frac{\lambda}{4}\mathrm{Tr}[MM^\dagger]^2,\end{aligned} \tag{2.5}$$

where $\tilde{W}^{\mu\nu}$ and $\tilde{B}^{\mu\nu}$ are the SM field strength tensors of the EW sector, and $F^{\mu\nu}_{L/R}$ are the field strength tensors corresponding to the $A_{L/R}$ vector meson fields. The $A_{L/R}$ fields can be interpreted as gauge fields of a 'Hidden Local Symmetry' [68, 69], with the same gauge structure as the original $SU(2)_L \otimes SU(2)_R$ global symmetry as described by [70, 66]. This means that the Lagrangian $\mathcal{L}_{boson}$ is written in a 'mixed' gauge, where the $A^\mu_{L/R}$ fields have already absorbed the associated Goldstone bosons and the remaining

---

'prime'

[3] See section 1.1.1 for detailed discussion on how the vev appears from the Higgs field.

pions of the Higgs matrix M are the Goldstone's associated with the usual EW fields $\tilde{W}_\mu$ and $\tilde{B}_\mu$.

The chiral theory introduces techni-doublets under $SU(2)_{L/R}$ in the unbroken phase, where the symmetry breaking pattern described above results in the doublets producing

$$2_L \otimes 2_R \rightarrow 3_V + 1_V. \tag{2.6}$$

The vector singlets of the theory are considered to be decoupled, and as we discuss further in chapter 6 do little to alter the model if an arbitrary number of singlets are added by hand. This leaves a vector meson triplet V under $SU(2)_V$, as well as an axial-vector partner triplet A, which are analagous to the QCD vector mesons ρ and a_1. Thus, the physical spectrum of this chiral gauge theory consists of the usual EW gauge boson triplet of $W^\pm$ and Z, a light scalar meson identified as the Higgs, plus two additional triplets which throughout this thesis are referred to as $(W^{\prime,+}, W^{\prime,-}, Z^\prime)$ and $(W^{\prime\prime,+}, W^{\prime\prime,-}, Z^{\prime\prime})$ (see our work in ref [4]).

2.2 Weinberg Sum Rules: Chiral EFT→NMWT

Thus far the Lagrangian in equation 2.5 is generalised to any chiral $SU(2)_L \otimes SU(2)_R$ gauge theory with $N_D = N_f/2$ doublets. We now wish to apply this generalised theory to our NMWT model, first we specify that there exists a single doublet containing two Dirac flavours. Additionally, we can make use of the Weinberg Sum Rules (WSR) [71] to connect the effective field theory to the dynamics and DEWSB of the underlying model. The WSRs describe the 2-point correlation functions of vector and axial currents and thus sensitive to chiral symmetry breaking, providing potential constraints on the parameter space of a given chiral field theory.

The generic 2-point correlation function of the time-ordered product of left-handed (LH) and right-handed (RH) currents as a function of 4-momentum q is

$$i\Pi^{\mu\nu}_{LR}(q) = 2i \int d^4x \exp^{iq\cdot x} \langle 0 | T(L^\mu(x) R^\nu(0)^\dagger) | 0 \rangle. \tag{2.7}$$

The L/R^μ are currents of the quark spinor $Q(x)$ arising from the new strong dynamics, so can be written as

$$L^{\mu}(x) = \bar{Q}(x)\frac{\gamma^{\mu}}{2}(1-\gamma^5)Q(x), \tag{2.8}$$

$$R^{\mu}(x) = \bar{Q}(x)\frac{\gamma^{\mu}}{2}(1+\gamma^5)Q(x). \tag{2.9}$$

It is useful here to translate the correlation functions from a L/R basis to a V/A (vector/axial) basis, where the vector and axial currents are defined as

$$J_V^{a\mu} = \bar{Q}T^a\gamma^{\mu}Q, \quad J_A^{a\mu} = \bar{Q}T^a\gamma^{\mu}\gamma^5 Q. \tag{2.10}$$

The correlation function in the V/A basis is then defined as the difference between vector-vector and axial-axial currents;

$$i\Pi^{a,b}_{\mu\nu,LR}(q) = \int d^4x \exp^{iq\cdot x}[\langle J^a_{\mu,V}(x)J^b_{\nu,V}(0)\rangle - \langle J^a_{\mu,A}(x)J^b_{\nu,A}(0)\rangle]. \tag{2.11}$$

In the chiral limit, i.e. light quarks taken as massless, the correlator in momentum space can be written as

$$\Pi^{a,b}_{\mu\nu,LR}(q) = (q_{\mu}q_{\nu} - g_{\mu\nu}q^2)\delta^{ab}\Pi_{LR}(q^2), \tag{2.12}$$

where the $SU(N_f)_{L/R}$ generators have been normalised such that $\mathrm{Tr}[T^aT^b] = \delta^{ab}/2$, and $a, b = 1, \ldots, N_f^2 - 1$ are the flavour currents of the chiral groups[72]. The chiral momentum squared function $\Pi_{LR}(q^2)$ obeys the unsubtracted dispersion relation

$$\Pi_{LR}(q^2) = \int_0^{\infty} ds \frac{\rho(s)}{s - q^2 - i\epsilon}, \tag{2.13}$$

where $\rho(s)$ is the spectral function. The form of the spectral function can be found by utilising the identity $1/(s - q^2 + i\epsilon) \simeq 1/(s - q^2) + i\pi\delta(s - q^2)$ to separate the real and imaginary parts of $\Pi_{LR}(q^2)$;

$$\rho(s) \equiv \frac{1}{\pi}\mathtt{Im}\Pi_{LR}(s). \tag{2.14}$$

To compute $\Pi_{LR}(q^2)$ in a regime where the intermediate states do not dominate, we consider the intermediate states as far off-shell, i.e. the correlator is in a *spacelike* momentum regime, $Q^2 = -q^2 \geq 0$. Hence the momentum-squared correlator becomes

$$\Pi_{LR}(Q^2) = \frac{1}{\pi}\int_0^\infty ds \frac{\mathtt{Im}\Pi_{LR}(s)}{s+Q^2}, \tag{2.15}$$

note that Q^2 is momentum in this particular regime, not the techni-quark spinor previously defined.

As discussed in section 1.3, we expect NMWT to be asymptotically free beyond the ETC energy scale, Λ_{ETC}, and as such can assume that the dispersion relation in equation 2.15 scales as in QCD (Q^{-6}). We can safely perform a Taylor expansion of 2.15 in this regime,

$$\Pi_{LR}(Q^2) = \frac{1}{\pi}\int_0^\infty ds \frac{\mathtt{Im}\Pi_{LR}(s)}{Q^2} - \frac{1}{\pi}\int_0^\infty dss \frac{\mathtt{Im}\Pi_{LR}(s)}{Q^4} + \ldots, \tag{2.16}$$

so using the QCD-like properties of NMWT at asymptotically high momenta, the 1st and 2nd WSRs respectively are

$$\int_0^\infty ds\mathtt{Im}\Pi_{LR}(s) = 0, \qquad \int_0^\infty dss\mathtt{Im}\Pi_{LR}(s) = 0. \tag{2.17}$$

Assuming that only the lowest vector and axial resonances saturate the WSRs, we can directly connect the WSRs with the NMWT model, by recasting Π_{LR} in terms of the vector and axial states and defining the vector/axial spectral functions

$$\begin{aligned}
\Pi_{LR}(s) &= \Pi_V(s) - \Pi_A(s) \\
\mathtt{Im}\Pi_V(s) &= \pi F_V^2 \delta(s - M_V^2) \\
\mathtt{Im}\Pi_A(s) &= \pi F_\pi^2 \delta(s) + \pi F_A^2 \delta(s - M_A^2),
\end{aligned}$$

where $M_{V/A}$, $F_{V/A}$ are the masses and decay constants of the vector and axial mesons respectively, and F_π is the TC pion decay constant.

Applying this to the 1st WSR we find,

$$F_V^2 - F_A^2 = F_\pi^2. \tag{2.18}$$

The additional factor of s in the 2nd WSR implies that this integral is less sensitive dynamics in the IR, instead receiving important contributions from the *near conformal region.* Thus we follow the procedure in Ref. [72] and allow for a modification of the 2nd WSR encoded by a dimensionless parameter a,

$$a\frac{8\pi^2}{d(R)}F_\pi^4 = F_V^2 M_V^2 - F_A^2 M_A^2, \tag{2.19}$$

where we expect $a > 0$ and $\mathcal{O}(1)$, and $d(R)$ is the dimension of the gauge group representation of the underlying techni-fermions.

We can further parameterise the NMWT model using the WSR at order $\mathcal{O}(Q^4)$, as one can identify the 0th WSR as the definition of the Peskin-Takeuchi S parameter[11],

$$S = 4\int_0^\infty \frac{ds}{s}\mathtt{Im}\bar{\Pi}_{LR}(s) = 4\pi\left[\frac{F_V^2}{M_V^2} - \frac{F_A^2}{M_A^2}\right]. \tag{2.20}$$

Note that $\mathtt{Im}\bar{\Pi}_{LR}$ is the usual spectral function for Π_{LR} with the Goldstone contribution subtracted.

2.3 Parameter Space of NMWT

With the gauge sector of a generic global $SU(2)_L \otimes SU(2)_R$ gauge theory set up, and theoretical constraints from WSRs defined, we can now fully connect the EFT to NMWT. Initially the parameter space of NMWT is defined by the Lagrangian parameters of equation 2.5, $m, r_2, \tilde{g}, r_3, s$. Aside from the $\tilde{g}$ parameter which we have seen previously is the effective coupling for chiral technicolor interactions, these parameters do little to enlighten us on the physical interpretation of the NMWT model. We wish to express the parameter space of the model in the most minimal and physically sensible set of independent parameters.

To this end, in the limit of zero electroweak couplings these can be combined to parameterise the masses and decay constants of the vector and axial resonances,

$$M_V^2 = m^2 + \frac{\tilde{g}^2(s - r_2)v^2}{4}, \quad F_V = \frac{\sqrt{2}M_V}{\tilde{g}}, \tag{2.21}$$

$$M_A^2 = m^2 + \frac{\tilde{g}^2(s + r_2)v^2}{4}, \quad F_A = \frac{\sqrt{2}M_A}{\tilde{g}}\chi, \tag{2.22}$$

where

$$\chi \equiv 1 - \frac{v^2\tilde{g}^2 r_3}{4M_A^2}. \tag{2.23}$$

The vector/axial masses in particular have a similar structure in all but the sign of the r_2 contribution, so it is sensible to make the replacement of m, r_2 to M_A, M_V as independent parameters of the model. Our 5-dimensional parameter space is now $(M_A, M_V, \tilde{g}, r_3, s)$.

Now considering the decay constants, we can make use of the WSRs to connect the decay constants of the model, F_A, F_V and F_π. In TC models with N_D doublets of technifermions and no scalar doublets, the pion decay constant is $F_\pi = 246\sqrt{N_D}$GeV, so as $N_D = 1$ in our NMWT model this decay constant is simply fixed at $F_\pi = 246$GeV. Perhaps one may wish to express the pion decay constant in terms of constants of nature, for these readers we express F_π as

$$F_\pi = \sqrt{\frac{1}{\sqrt{2}G_F}}, \tag{2.24}$$

where G_F is the Fermi coupling constant. Combining the definitions in 2.22 the decay constants are related by the equation

$$F_\pi^2 = (1 + 2\omega)F_V^2 - F_A^2, \tag{2.25}$$

where we define this new ω parameter as the combination

$$\omega \equiv \frac{v^2\tilde{g}^2}{4M_V^2}(1 - r_3 + r_2). \tag{2.26}$$

Equation 2.25 looks very similar to the 1st WSR in equation 2.18, with a modification from the ω parameter. If NMWT is constrained such that there is no deviation from the 1st WSR, then we recover equation 2.18 and enforce the constraint $\omega = 0$, leading to the relation

$$r_2 = r_3 - 1. \tag{2.27}$$

We want the S parameter to replace one of the Lagrangian variables, r_3, as an independent parameter, which can be achieved by inspecting the dependence of χ on S. Using the result for the 0th WSR (equation 2.20) combined with the above definitions for $F_{V/A}$, we can write the S parameter as

$$S = \frac{8\pi}{\tilde{g}^2}(1 - \chi^2), \tag{2.28}$$

thus χ can be written as

$$\chi = \sqrt{1 - \frac{\tilde{g}^2 S}{8\pi}}. \tag{2.29}$$

Combining this definition of χ with equation 2.23, r_3 as a function of independent parameters is then

$$r_3 = \frac{4M_A^2}{v^2\tilde{g}^2}\left(1 - \sqrt{1 - \frac{S\tilde{g}^2}{8\pi}}\right). \tag{2.30}$$

Thus making the replacement of $r_2 \to M_A - M_V$ and $r_3 \to S$, the NMWT parameter space is now defined in terms of $(M_A,\ M_V,\ S,\ \tilde{g},\ s)$[4].

It is expected that the vector and axial masses cannot be independently defined, making this connection the NMWT parameter space is reduced by one degree of freedom. Let us choose M_A to be the independent parameter. Substituting the expressions for $F_{V/A}$ in terms of $M_{V/A}$ into the 1st WSR (equations 2.22 and 2.18 respectively),

$$M_V^2 = M_A^2\chi^2 + \frac{\tilde{g}^2}{2}F_\pi^2. \tag{2.31}$$

---

[4] For the curious reader, I present the full derivation of all dependent parameters in the full 5-D parameter space in Appendix A

With the definition of χ in equation 2.29 we can write the vector mass as a function of independent parameters,

$$M_V^2 = M_A^2\left(1 - \frac{\tilde{g}^2 S}{8\pi}\right) + \frac{\tilde{g}^2}{2}F_\pi^2. \tag{2.32}$$

The 4-D independent parameter space of NMWT is now defined as

$$M_A, \quad \tilde{g}, \quad S, \quad s. \tag{2.33}$$

2.3.1 Constraints on S from Electroweak Precision Data

The S parameter is of particular importance in this model. In terms of physical parameters, S represents the mass splitting between the vector and axial masses (equation 2.20), thus defining the level of degeneracy between the Z' and Z'' vector mesons. Further to this, identifying S as the oblique electroweak parameter, S, established by Peskin and Takeuchi[11], places significant experimentally motivated restrictions on NMWT.

The S, T, and U parameters classify vacuum polarisations in the electroweak sector, effectively providing quantifiable corrections to weak sector parameters such as the W and Z masses. Collider experiments measure the properties of the weak bosons ever more precisely, providing constraints on these Peskin-Takeuchi parameters and therefore being sensitive to additional contributions to the EW sector from new physics. Any new gauge sector that couples to the EW bosons will contribute in the form of radiative corrections at one-loop level to the W and Z self-energies. In the case of technicolor models (and assorted BSM models), the U parameter receives negligible contributions from new physics at the Λ_{TC} energy scale, so the usual assumption of $U = 0$ is universally applied in NMWT.

The T parameter provides a measure of weak-isospin breaking effects, whereas S is a measure of chiral symmetry breaking effects so is more sensitive to additional neutral currents from new physics in the EW sector. Precision experiments such as LEP provide the best measurements of EW parameters, from which global fits can be performed to provide the simultaneous constraints on the S and T parameters[2]. The recent constraints provided by the GFITTER group are shown in Figure 2.1

Interpreting the experimental constraints on T and S in the context of NMWT, let us first apply the assumption that the contribution from the

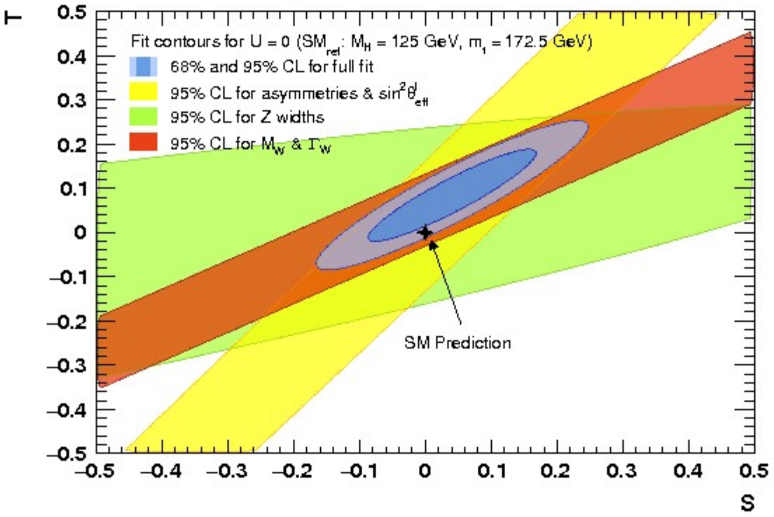

Figure 2.1: Global fits of S and T oblique electroweak parameters from electroweak precision data (EWPD)[1], with $U = 0$. Figure from GFITTER group[2].

TC sector to weak isospin breaking is minimal, so $T = 0$. Then from Figure 2.1 the limits on S can be easily determined, as such the level of degeneracy between the neutral TC gauge mesons must be highly constrained in accordance with equation 2.20. A unique feature of Technicolor models is that the S parameter can in fact be negative, as the relative size of the vector and axial pion correlators can be ordered in such a way as to re-order the lowest neutral mesons. For the NMWT parameter space, S is an independent parameter which we restrict to take any value within the constraints from electroweak precision data (EWPD).

2.3.2 Theoretical Constraint on M_A from the 2nd WSR

This parameter space discussion thus far has consisted of parameters and relationships directly from the gauge sector Lagrangian, however we must note that an additional parameter arises indirectly as a result of the 2nd WSR. This is the dimensionless a parameter (equation 2.19), which defines the level of deviation from the 2nd WSR coming from the near-conformal region.

The a parameter depends on the group representation dimension $d(R)$ of the techni-fermions in the model, and in NMWT there is a single techni-quark doublet of two Dirac fermions in the two-index symmetric representation, where $d(R) = 6$.

Combining the 1st and 2nd WSRs, the a parameter in NMWT is then

$$a = \frac{3}{2\pi^2 F_\pi^4 \tilde{g}^2}(M_V^4 - M_A^4\chi^2), \tag{2.34}$$

so the a parameter contributes to the mass splitting of vector and axial states, thus it contributes to the already constrained S parameter.

Initially we stated that a is expected to be positive, but in principle the sign of a could be negative. However if we consider that the S parameter must be small due to EWPD then it stands to reason that a should contribute negatively to S, which occurs in the case where $a > 0$.

Furthermore, in a QCD-like theory one would expect the 2nd WSR to hold exactly such that $a = 0$, while the modified dynamics of a walking coupling introduces a near-conformal region which contributes positively to the 2nd WSR, so we expect $a > 0$[72]. The implications of a positive a on the near-degeneracy of the vector and axial mesons appears to be conform to the results of various Schwinger-Dyson analyses of walking dynamics [73, 74]. Throughout this work, $a > 0$ is taken to be a strict condition necessary for the walking dynamics of NMWT. We can then set a limit on the model such that $a < 0$ corresponds to non-walking dynamics and is therefore excluded. Setting $s = 0$ and choosing discrete values of S, we can project a in the 2-dimensional $M_A, \tilde{g}$ parameter space (Figure 2.2). Here we see that there is an S dependent upper limit on the mass scale of Technicolor, so if one considers the restriction $a > 0$ to be concrete then NMWT can be bounded from above in M_A. This offers exciting implications for the eventual exploration of the entire NMWT parameter space at experiments, as will be discussed in later chapters.

2.3.3 Further Theoretical Constraints on NMWT

As stated in section 2.1, the NMWT gauge sector Lagrangian $\mathcal{L}_{boson}$ (equation 2.5) is written in a ‘mixed’ gauge, where the $A_{L/R}$ fields have absorbed their corresponding pions and are already massive gauge fields. While we do not derive this Lagrangian explicitly in this work (see [70]), it is useful to note that the vev for the TC sector, f,

$$f = \frac{2m}{\tilde{g}}, \tag{2.35}$$

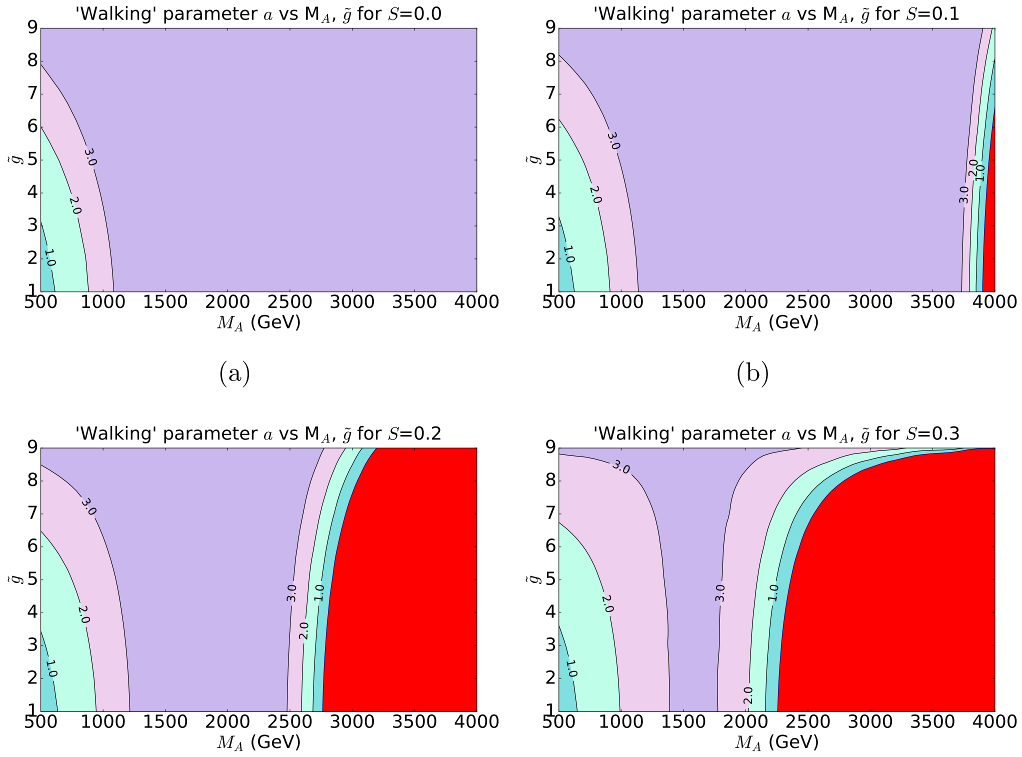

(a)

(b)

(c)

(d)

Figure 2.2: Contour levels for a parameter in $(M_A,\tilde{g})$ NMWT plane for various values of S and fixed $s = 0$. The red-shaded region corresponds to excluded $a < 0$ space.

defined in terms of the ratio between the mass and coupling Lagrangian parameters in the TC sector. This is no surprise, however if we redefine this in terms of the independent NMWT parameters then a useful feature of the model parameter space from can be easily derived;

$$f = \frac{\sqrt{4M_A^2 - \tilde{g}^2(r_2 + s)v^2}}{\tilde{g}}. \tag{2.36}$$

In order for the theory to remain physical, this TC vev then enforces a model-dependent upper bound on the Higgs to EW/TC coupling parameter

s,

$$s < \frac{4M_A^2}{\tilde{g}^2 v^2} - r_2. \tag{2.37}$$

In part this forbids the theory to have a mass scale that is too low to generate the TC scale symmetry breaking, and restores the hierarchy of masses between the Higgs and EW scale gauge bosons with the TC gauge mesons.

Furthermore there is an upper bound on the TC effective coupling $\tilde{g}$ enforced by the definition of F_A. Combining the F_A definition of equation 2.22 with χ as defined in equation 2.29, the limit is

$$\tilde{g} < \sqrt{\frac{8\pi}{S}}. \tag{2.38}$$

This is a theoretical hard limit on the decoupling of the TC sector from the EW sector, ensuring that all decay constants (in particular the axial-vector decay constant) are strictly real. The tightest constraint comes from the case in which the degeneracy of the vector and axial modes is minimised with respect to the EWPD parameter S. Although EWPD already rules out values as high as $S = 0.3$, historically this has been the benchmark value for early WTC studies, so for direct comparison with [66] the upper limit in this case is $\tilde{g} \leq 9.15$. Despite the updated benchmark of $S = 0.1$, where the upper limit is $\tilde{g} \leq 15.85$, we present the parameter space up to $\tilde{g} = 9$ (as in Figure 2.2) in order to avoid presenting an unphysical parameter space as we explore the phenomenology of $S \neq 0.1$.

Chapter 3

Physical Spectrum of NMWT

3.1 Mass Matrices in NMWT

The physical spectrum of NMWT at the symmetry breaking scale consists of the EW gauge bosons $\gamma, Z, W^{\pm}$, the composite Higgs, and the gauge meson triplets $Z', W'^{\pm}$ and $Z'', W''^{\pm}$, which arise from the basis transformation from the gauge eigenbasis to the mass eigenbasis. The interaction terms of the Lagrangian $\mathcal{L}_{boson}$ (equation 2.5) contain 2-point interactions between the $A_{L/R}$, $\tilde{W}_\mu$, and $\tilde{B}_\mu$ fields. As such we can construct a mass-term Lagrangian for the gauge fields in the gauge eigenbasis as

$$\mathcal{L}_{mass} = \begin{pmatrix} \tilde{W}^-_\mu & A^-_{L\mu} & A^-_{R\mu} \end{pmatrix} \mathcal{M}^2_C \begin{pmatrix} \tilde{W}^{+\mu} \\ A^{+\mu}_L \\ A^{+\mu}_R \end{pmatrix} + \frac{1}{2} \begin{pmatrix} \tilde{B}_\mu & \tilde{W}^0_\mu & A^0_{L\mu} & A^0_{R\mu} \end{pmatrix} \mathcal{M}^2_N \begin{pmatrix} \tilde{B}^\mu \\ \tilde{W}^{0\mu} \\ A^{0\mu}_L \\ A^{0\mu}_R \end{pmatrix}, \tag{3.1}$$

where $\mathcal{M}^2_C$ and $\mathcal{M}^2_N$ are the charged and neutral sector mixing matrices which diagonalise to the mass eigenbasis.

In the broken phase of the chiral theory, this low-energy NMWT is broken to a vector/axial gauge group, so it is useful to translate the L/R fields in the bosonic Lagrangian to V/A fields. The L/R fields are then simple linear combinations of vector and axial fields V_μ and A_μ,

$$A^a_{L\mu} = \frac{V^a_\mu + A^a_\mu}{\sqrt{2}}, \quad A^a_{R\mu} = \frac{V^a_\mu - A^a_\mu}{\sqrt{2}}, \tag{3.2}$$

where $a = +, -, 0$ correspond to the electric charge assignments of the components of the vector (axial) triplet.

Let us now redefine the mass-mixing Lagrangian in terms of the vector/axial fields

$$\mathcal{L}_{mass} = \begin{pmatrix} \tilde{W}^{-}_{\mu} & A^{-}_{\mu} & V^{-}_{\mu} \end{pmatrix} \mathcal{M}^2_C \begin{pmatrix} \tilde{W}^{+\mu} \\ A^{+\mu} \\ V^{+\mu} \end{pmatrix} + \frac{1}{2} \begin{pmatrix} \tilde{B}_{\mu} & \tilde{W}^0_{\mu} & A^0_{\mu} & V^0_{\mu} \end{pmatrix} \mathcal{M}^2_N \begin{pmatrix} \tilde{B}^{\mu} \\ \tilde{W}^{0\mu} \\ A^{0\mu} \\ V^{0\mu} \end{pmatrix}, \tag{3.3}$$

where now the charged/neutral mixing matrices are formed of the two-point functions of the bosonic Lagrangian *after* the substitution in equation 3.2 is made.

If one makes the usual parameterisation of Lagrangian coefficients in terms of vector and axial masses $M_{V/A}$, these mixing matrices in the gauge eigenbasis are then

$$\mathcal{M}^2_C = \begin{pmatrix} \frac{g_2^2}{\tilde{g}^2} M_V^2 & -\frac{g_2}{\sqrt{2}\tilde{g}} M_A^2 \chi & -\frac{g_2}{\sqrt{2}\tilde{g}} M_V^2 \\ -\frac{g_2}{\sqrt{2}\tilde{g}} M_A^2 \chi & M_A^2 & 0 \\ -\frac{g_2}{\sqrt{2}\tilde{g}} M_V^2 & 0 & M_V^2 \end{pmatrix}, \tag{3.4}$$

$$\mathcal{M}^2_N = \begin{pmatrix} \frac{g_1^2}{\tilde{g}^2} M_V^2 & 0 & \frac{g_1}{\sqrt{2}\tilde{g}} M_A^2 \chi & -\frac{g_1}{\sqrt{2}\tilde{g}} M_V^2 \\ 0 & \frac{g_2^2}{\tilde{g}^2} M_V^2 & -\frac{g_2}{\sqrt{2}\tilde{g}} M_A^2 \chi & -\frac{g_2}{\sqrt{2}\tilde{g}} M_V^2 \\ \frac{g_1}{\sqrt{2}\tilde{g}} M_A^2 \chi & -\frac{g_2}{\sqrt{2}\tilde{g}} M_A^2 \chi & M_A^2 & 0 \\ -\frac{g_1}{\sqrt{2}\tilde{g}} M_V^2 & -\frac{g_2}{\sqrt{2}\tilde{g}} M_V^2 & 0 & M_V^2 \end{pmatrix}, \tag{3.5}$$

where the constraint $\omega = 0$ has been applied to achieve the 4-D parameterisation of NMWT as described in section 2.3. A fully independent and generalised form of these matrices is given in Appendix A.

A few notes should be discussed regarding these matrices, firstly one can easily identify that the charged mixing matrix $\mathcal{M}^2_C$ is exactly the lower 3×3 block of the neutral $\mathcal{M}^2_N$. This reflects the lack of hypercharge mixing in the charged sector as well as the indistinguishable mixing of the purely $SU(2)$ components in the gauge eigenbasis. There is also the interesting feature of zero mixing between the neutral component of $\tilde{W}_{\mu}$ with the $\tilde{B}_{\mu}$ field in this basis, contrary to the equivalent mixing in the SM. There is also the feature of a strictly diagonal gauge mixing sector for purely TC gauge interactions. This ensures that before diagonalisation, the TC sector is formed of purely axial and purely vector fields.

An important note is that we assert that the mass ordering of the resonances Z' and Z'' must be such that $M_{Z'} < M_{Z''}$. In the regime in which the *axial-vector* resonance has the heavier mass, the 3rd and 4th columns/rows of the matrices 3.5 should be switched (as well the V_μ and A_μ fields in the vectors of 3.3). The process of diagonalisation in such a regime will of course produce an entirely different phenomenology with respect to the physical resonances and their interactions. The analytic results in the regime $M_A > M_V$ are discussed in Appendix B.

The gauge sector in the gauge and mass eigenbases are related through the elements of the matrices $\mathcal{N}/\mathcal{C}$ that diagonalise the $\mathcal{M}^2_{N/C}$ mixing matrices respectively. In the regime $M_A < M_V$, the linear combinations of physical gauge mediators γ, Z, Z', Z'' in the neutral sector are

$$\begin{aligned}
\tilde{B} &= N_{11}\gamma + N_{12}Z + N_{13}Z' + N_{14}Z'' \\
\tilde{W}^0 &= N_{21}\gamma + N_{22}Z + N_{23}Z' + N_{24}Z'' \\
A^0 &= N_{31}\gamma + N_{32}Z + N_{33}Z' + N_{34}Z'' \\
V^0 &= N_{41}\gamma + N_{42}Z + N_{43}Z' + N_{44}Z'',
\end{aligned} \tag{3.6}$$

in the charge sector the gauge fields as linear combinations of $W^\pm$, $W'^\pm$ and $W''^\pm$ are

$$\begin{aligned}
\tilde{W}^\pm &= C_{11}W^\pm + C_{12}W'^\pm + C_{13}W''^\pm \\
A^\pm &= C_{21}W^\pm + C_{22}W'^\pm + C_{23}W''^\pm \\
V^\pm &= C_{31}W^\pm + C_{32}W'^\pm + C_{33}W''^\pm.
\end{aligned} \tag{3.7}$$

The picture in the $M_A > M_V$ regime also swaps the order of the vector and axial fields such that for $A^{\pm(0)}$, $C_{2j} \to C_{3j}$ ($N_{3j} \to N_{4j}$) and vice versa for $V^{\pm(0)}$.

3.2 Analytic Diagonalisation of Mixing Matrices

The elements $N_{ij}(C_{ij})$ provide important insight into the mixing between the neutral(charged) fields, including the structure and contributions to coupling strengths and the composition of the neutral resonances. The $\mathcal{N}(\mathcal{C})$ matrices are calculated by diagonalising the bosonic mixing matrices 3.5, however the explicit diagonalisation of $\mathcal{M}^2_{N/C}$ yields complicated analytic forms for the $\mathcal{N}$ and $\mathcal{C}$ matrices. As such we calculate $N_{ij}(C_{ij})$ by performing a perturbative analysis in orders of $1/\tilde{g}$, calculating the eigenvalues and eigenvectors of $\mathcal{N}(\mathcal{C})$ order by order up to $\mathcal{O}(1/\tilde{g}^2)$.

Let us first perform the perturbative diagonalisation of the neutral sector. Rephrasing the χ and M_V^2 parameters in terms of the independent parameter space (equations 2.29 and 2.32 respectively), we can rewrite the gauge mixing matrices in a fully independent way. The matrix $\mathcal{M}_N^2$ is then

$$\mathcal{M}_N^2 = \begin{pmatrix} \frac{g_1^2 M_A^2}{\tilde{g}^2}(1-\frac{\tilde{g}^2 S}{8\pi}+\frac{F_\pi^2\tilde{g}^2}{2M_A^2}) & 0 & \frac{g_1 M_A^2}{\sqrt{2}\tilde{g}}\sqrt{1-\frac{\tilde{g}^2 S}{8\pi}} & -\frac{g_1 M_A^2}{\sqrt{2}\tilde{g}}(1-\frac{\tilde{g}^2 S}{8\pi}+\frac{F_\pi^2\tilde{g}^2}{2M_A^2}) \\ 0 & \frac{g_2^2 M_A^2}{\tilde{g}^2}(1-\frac{\tilde{g}^2 S}{8\pi}+\frac{F_\pi^2\tilde{g}^2}{2M_A^2}) & -\frac{g_2 M_A^2}{\sqrt{2}\tilde{g}}\sqrt{1-\frac{\tilde{g}^2 S}{8\pi}} & -\frac{g_2 M_A^2}{\sqrt{2}\tilde{g}}(1-\frac{\tilde{g}^2 S}{8\pi}+\frac{F_\pi^2\tilde{g}^2}{2M_A^2}) \\ \frac{g_1 M_A^2}{\sqrt{2}\tilde{g}}\sqrt{1-\frac{\tilde{g}^2 S}{8\pi}} & -\frac{g_2 M_A^2}{\sqrt{2}\tilde{g}}\sqrt{1-\frac{\tilde{g}^2 S}{8\pi}} & M_A^2 & 0 \\ -\frac{g_1 M_A^2}{\sqrt{2}\tilde{g}}(1-\frac{\tilde{g}^2 S}{8\pi}+\frac{F_\pi^2\tilde{g}^2}{2M_A^2}) & -\frac{g_2 M_A^2}{\sqrt{2}\tilde{g}}(1-\frac{\tilde{g}^2 S}{8\pi}+\frac{F_\pi^2\tilde{g}^2}{2M_A^2}) & 0 & M_A^2(1-\frac{\tilde{g}^2 S}{8\pi}+\frac{F_\pi^2\tilde{g}^2}{2M_A^2}) \end{pmatrix}. \tag{3.8}$$

At 0th order in $1/\tilde{g}$, the mass squared terms for the neutral bosons are

$$M_\gamma^2 = 0, \quad M_Z^2 = 0, \quad M_{Z'}^2 = M_A^2, \quad M_{Z''}^2 = M_A^2(1-\frac{\tilde{g}^2 S}{8\pi}) + \frac{1}{2}\tilde{g}^2 F_\pi^2. \tag{3.9}$$

At this order, the eigenvalues for the γ, Z are degenerate and $m_\gamma^2, m_Z^2 = 0$, so the eigenvectors cannot be uniquely defined at this stage. To resolve this degeneracy we introduce a generic parameter x will be fixed at higher order in the expansion. The 0th order eigenvectors are then

$$\bar{v}_0 = \begin{pmatrix} \frac{x}{\sqrt{1+x^2}} & \frac{1}{\sqrt{1+x^2}} & 0 & 0 \\ \frac{1}{\sqrt{1+x^2}} & -\frac{x}{\sqrt{1+x^2}} & 0 & 0 \\ 0 & 0 & 1 & 0 \\ 0 & 0 & 0 & 1 \end{pmatrix}. \tag{3.10}$$

We can now construct the higher order corrections order by order. To calculate the 1st order corrections, we consider the eigenvalue equation

$$M\bar{v} = \lambda\bar{v} \tag{3.11}$$

where $M = M_0 + M_1 + M_2 + \ldots$ is the mixing matrix $\mathcal{M}^2_{N(C)}$ in orders of $1/\tilde{g}$, $\bar{v} = \bar{v}_0 + \bar{v}_1 + \bar{v}_2 + \ldots$ are the eigenvectors of M, and $\lambda = \lambda_0 + \lambda_1 + \lambda_2 + \ldots$ are the eigenvalues of M. At first order we have

$$\begin{aligned}
&(M_0 + M_1)(\bar{v}_0 + \bar{v}_1) = (\lambda_0 + \lambda_1)(\bar{v}_0 + \bar{v}_1)\\
&M_0\bar{v}_1 + M_1\bar{v}_0 + M_1\bar{v}_1 = \lambda_0\bar{v}_1 + \lambda_1\bar{v}_0 + \lambda_1\bar{v}_1\\
&\lambda_1 = \bar{v}_0^T(M_0 - \lambda_0)\bar{v} + \bar{v}_0^T M_1\bar{v}_0\\
&\lambda_1 = \bar{v}_0^T M_1\bar{v}_0,
\end{aligned}$$

where we have used the 0th order eigenvalue equation $M_0\bar{v}_0 = \lambda_0\bar{v}_0$ to remove 0th order terms, and have discarded terms of order > 1.

We can immediately see that the 1st order eigenvalues are $\lambda_1^i = 0$ for all $i = 1, \ldots, 4$, as $\mathcal{M}^2_N$ does not have any diagonal components at order $1/\tilde{g}$. Further to this, there should not be corrections to the squared masses of the vector bosons at odd order in $1/\tilde{g}$ as this would result in mass terms dependent on fractional powers in the coupling.

The first order eigenvectors and in terms of model parameters and the unknown x are

$$\bar{v}_1 = \begin{pmatrix}
0 & 0 & \frac{g_2 - g_1 x}{\sqrt{2}\tilde{g}\sqrt{1+x^2}}\sqrt{1 - \frac{\tilde{g}^2 S}{8\pi}} & \frac{g_2 + g_1 x}{\sqrt{2}\tilde{g}\sqrt{1+x^2}}\\
0 & 0 & -\frac{g_1 + g_2 x}{\sqrt{2}\tilde{g}\sqrt{1+x^2}}\sqrt{1 - \frac{\tilde{g}^2 S}{8\pi}} & \frac{g_1 - g_2 x}{\sqrt{2}\tilde{g}\sqrt{1+x^2}}\\
\frac{g_1}{\sqrt{2}\tilde{g}}\sqrt{1 - \frac{\tilde{g}^2 S}{8\pi}} & -\frac{g_2}{\sqrt{2}\tilde{g}}\sqrt{1 - \frac{\tilde{g}^2 S}{8\pi}} & 0 & 0\\
-\frac{g_1}{\sqrt{2}\tilde{g}} & -\frac{g_2}{\sqrt{2}\tilde{g}} & 0 & 0
\end{pmatrix}. \tag{3.12}$$

To find the 2nd order eigenvalues, we follow the same procedure as above, and keeping only 2nd order terms we find

$$\lambda_2 = \bar{v}_0^T M_1\bar{v}_1 + \bar{v}_0^T M_2\bar{v}_0 - \bar{v}_0^T\lambda_1\bar{v}_1, \tag{3.13}$$

where we use the fact that $\lambda_1 = 0$ to reduce this to

$$\lambda_2 = \bar{v}_0^T M_1 \bar{v}_1 + \bar{v}_0^T M_2 \bar{v}_0. \tag{3.14}$$

At this order we can now fix x, which turns out to be $x = g_2/g_1$, and we arrive at the 2nd order corrections to the neutral vector boson masses;

$$M_\gamma^2 = 0, \quad M_Z^2 = \frac{1}{4}(g_1^2 + g_2^2)F_\pi^2, \quad M_{Z'}^2 = \frac{g_1^2 + g_2^2}{2\tilde{g}^2} M_A^2 (1 - \frac{\tilde{g}^2 S}{8\pi}), \tag{3.15}$$

$$M_{Z''}^2 = \frac{g_1^2 + g_2^2 + 2\tilde{g}^2}{2\tilde{g}^2} M_A^2 (1 - \frac{\tilde{g}^2 S}{8\pi} + \frac{F_\pi^2 \tilde{g}^2}{2M_A^2}). \tag{3.16}$$

Finally, the rotation matrix $\mathcal{N}$ can be constructed from the transpose of the sum of 0th, 1st and 2nd order eigenvectors;

$$\mathcal{N} = \begin{pmatrix} \frac{g_2}{\sqrt{g_1^2+g_2^2}} & \frac{g_1}{\sqrt{g_1^2+g_2^2}} & \frac{g_1\chi}{\sqrt{2}\tilde{g}} & -\frac{g_1}{\sqrt{2}\tilde{g}} \\ \frac{g_1}{\sqrt{g_1^2+g_2^2}} & -\frac{g_2}{\sqrt{g_1^2+g_2^2}} & -\frac{g_2\chi}{\sqrt{2}\tilde{g}} & -\frac{g_2}{\sqrt{2}\tilde{g}} \\ 0 & -\frac{\sqrt{g_1^2+g_2^2}\chi}{\sqrt{2}\tilde{g}} & 1 & -\frac{(g_1^2-g_2^2)(2M_A^2\chi^2+\tilde{g}^2F_\pi^2)\chi}{\tilde{g}^2M_A^2(4\chi^2-1)+2\tilde{g}^4F_\pi^2} \\ \frac{\sqrt{2}g_1g_2}{\sqrt{g_1^2+g_2^2}\tilde{g}} & \frac{(g_1^2-g_2^2)}{\sqrt{2}\tilde{g}\sqrt{g_1^2+g_2^2}} & \frac{4(g_1^2-g_2^2)M_A^2\chi}{2\tilde{g}^2M_A^2(\chi^2-4)+\tilde{g}^4F_\pi^2} & 1 \end{pmatrix}, \tag{3.17}$$

where we have replaced the function χ for a more concise expression.

Repeating this process in the charged sector we find $\mathcal{C}$ to second order,

$$\mathcal{C} = \begin{pmatrix} 1 & -\frac{g_2\chi}{\sqrt{2}\tilde{g}} & -\frac{g_2}{\sqrt{2}\tilde{g}} \\ \frac{g_2\chi}{\sqrt{2}\tilde{g}} & 1 & \frac{g_2\chi}{\sqrt{2}\tilde{g}}(1 + \frac{2M_A^2}{2M_A^2(3\chi^2-1)+3\tilde{g}^2F_\pi^2}) \\ \frac{g_2}{\sqrt{2}\tilde{g}} & -\frac{3g_2^2M_A^2\chi}{2\tilde{g}^2M_A^2(\chi^2-3)+\tilde{g}^4F_\pi^2} & 1 \end{pmatrix}, \tag{3.18}$$

and the charged resonance masses up to $\mathcal{O}(\tilde{g}^{-2})$ are

$$M_W^2 = \frac{F_\pi^2 g_2^2}{4}, \quad M_{W'}^2 = M_A^2\left(1+\frac{g_2^2}{2\tilde{g}^2}\chi^2\right), \quad M_{W''}^2 = M_A^2\left(1+\frac{g_2^2}{2\tilde{g}^2}\right)\left(\chi^2+\frac{F_\pi^2\tilde{g}^2}{2M_A^2}\right). \tag{3.19}$$

The diagonalising matrices $\mathcal{N}$ and $\mathcal{C}$ will change significantly in the region of parameter space where $M_A > M_V$, so the calculation is repeated with the columns/rows of $\mathcal{M}_N^2$ and $\mathcal{M}_C^2$ switched as described in section 3.1. As $\mathcal{N}$ and $\mathcal{C}$ are simply constructed of eigenvectors of the mixing matrices, they are again related to equations 3.17 and 3.18 by switching the order of the final two columns/rows.

3.3 Solving for EW couplings

The gauge couplings for the EW sector, g_1 and g_2, are no longer independent parameters as in the SM, as such there exist analytic formulae for g_1 and g_2 in terms of the independent parameters of NMWT. These couplings can be derived as roots of the characteristic equation for the Z boson eigenvalue, i.e we can solve the equation $\det[\mathcal{M}_N^2 - \mathbb{1}M_Z^2] = 0$. Taking the absolute values of the roots, we find two solutions to this equation which correspond to the couplings g_2 and g_1 respectively,

$$g_2 = \tilde{g}\sqrt{\frac{(\tilde{g}^2 - 2e^2)abM_Z^2 + \sqrt{abM_Z^2(2e^2M_Z^2 + \tilde{g}^2b)(a(\tilde{g}^2M_Z^2 - 2e^2b) + 2e^2M_A^4\chi^2)}}{M_V^2a(4e^2 + \tilde{g}^2(b - M_Z^2)) - M_A^4\chi^2(2e^2M_Z^2 + \tilde{g}^2b))}} \tag{3.20}$$

$$g_1 = \tilde{g}\sqrt{\frac{(\tilde{g}^2 - 2e^2)abM_Z^2 - \sqrt{abM_Z^2(2e^2M_Z^2 + \tilde{g}^2b)(a(\tilde{g}^2M_Z^2 - 2e^2b) + 2e^2M_A^4\chi^2)}}{M_V^2a(4e^2 + \tilde{g}^2(b - M_Z^2)) - M_A^4\chi^2(2e^2M_Z^2 + \tilde{g}^2b))}} \tag{3.21}$$

where $a = (M_A^2 - M_Z^2)$, $b = (M_V^2 - M_Z^2)$, e is the electromagnetic coupling which is fixed to its SM value. Again we have not replaced M_V and χ with their explicit functions of independent parameters, as this does not provide much useful insight for these gauge couplings.

3.4 CalcHEP Implementation of Diagonalisation

The NMWT model has already been implemented in the CalcHEP framework by Frandsen *et al*[70, 66], with the reduced set of independent parameters $(M_A, \tilde{g}, S)$. This model requires external functions interfaced with the

CalcHEP model that perform the diagonalisation of mass matrices and numerical evaluation of g_2 respectively. We have since updated the model to encapsulate the full 5D $(M_A, \tilde{g}, S, s, \omega)$ parameter space, as well as scripting inbuilt mass-matrix diagonalisation and analytic form of g_2 such that the model is self-contained. The details of these extensions are briefly detailed here.

The extension of the model to a fully 5D parameter space was trivial to implement at the level of the LanHEP formulation of the Lagrangian parameters, the addition of the s parameter was already in place so we simply set s to be a variable parameter rather than hard-coded to $s = 0$ as in the original model. The ω parameter was implemented in the context of the r_2 and r_3 parameters. Using the relationship found in equation 2.26 we redefine the model parameters such that

$$r_2 = r_3 - 1 - \tilde{\omega}, \tag{3.22}$$

where $\tilde{\omega}$ is a placeholder parameter that defines the actual ω parameter

$$\omega = \frac{v^2 \tilde{g}^2 \tilde{\omega}}{4 M_V^2}. \tag{3.23}$$

This has now fully parameterised the NMWT model in 5 dimensions, as the remaining variables are written in terms of r_2 and r_3 which implicitly contain the independent parameter ω.

Where the previous model relied on an external C/FORTRAN script to calculate g_2 in a model-dependent way, this was purely a numerical approximation. As we have analytically evaluated the g_1 and g_2 parameters in terms of the NMWT parameter space in the previous section 3.3, we simply write in these analytic functions (equations 3.20 and 3.20) directly into the LanHEP model.

Finally, we replace the external mass matrix diagonalisation script with inbuilt SLHA functions written at the level of the LanHEP model. The SLHA+ library [75] provides routines for diagonalisation that are inbuilt into the CalcHEP and LanHEP programmes. A sample of the code is shown in Figure 3.1, where the full code for the neutral sector is included. These built in functions allow the CalcHEP model outputted from the LanHEP implementation to be fully self-contained.

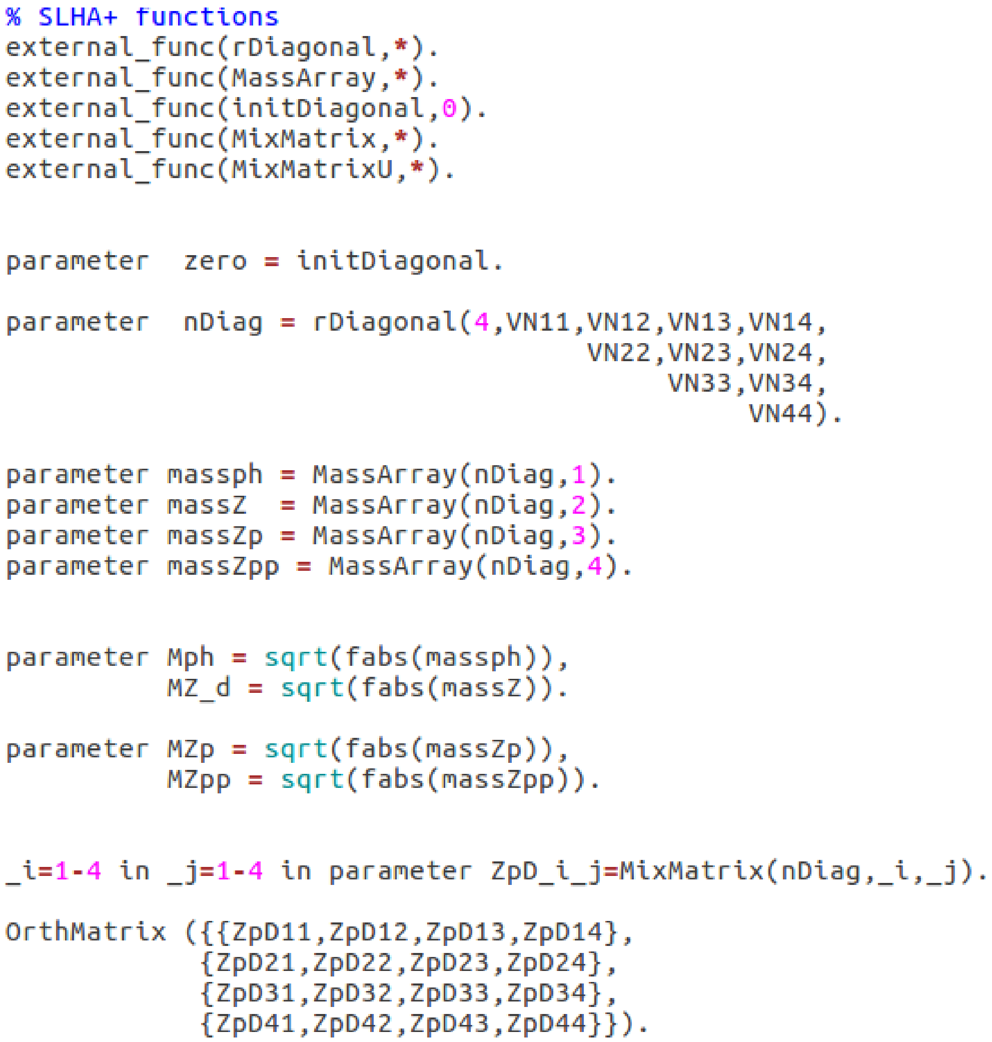

```
% SLHA+ functions
external_func(rDiagonal,*).
external_func(MassArray,*).
external_func(initDiagonal,0).
external_func(MixMatrix,*).
external_func(MixMatrixU,*).


parameter  zero = initDiagonal.

parameter  nDiag = rDiagonal(4,VN11,VN12,VN13,VN14,
                                    VN22,VN23,VN24,
                                         VN33,VN34,
                                              VN44).

parameter massph = MassArray(nDiag,1).
parameter massZ  = MassArray(nDiag,2).
parameter massZp = MassArray(nDiag,3).
parameter massZpp = MassArray(nDiag,4).


parameter Mph = sqrt(fabs(massph)),
          MZ_d = sqrt(fabs(massZ)).

parameter MZp = sqrt(fabs(massZp)),
          MZpp = sqrt(fabs(massZpp)).


_i=1-4 in _j=1-4 in parameter ZpD_i_j=MixMatrix(nDiag,_i,_j).

OrthMatrix ({{ZpD11,ZpD12,ZpD13,ZpD14},
            {ZpD21,ZpD22,ZpD23,ZpD24},
            {ZpD31,ZpD32,ZpD33,ZpD34},
            {ZpD41,ZpD42,ZpD43,ZpD44}}).
```

Figure 3.1: SLHA+ procedure for diagonalising the neutral gauge sector of the NMWT model in LanHEP

Chapter 4

Phenomenology of Z's in NMWT

The physical spectrum of NMWT is rich with new resonances to discover in the LHC accessible energy range, with the unique and interesting signature of a pair of distinct neutral TeV-scale resonances. The potential for discovery of two new neutral gauge particles depends on their properties, which can be fully explored and categorised with Matrix Element Generator tools. The phenomenology of the NMWT model is explored using the CalcHEP package [76] which allows us to perform a simple and robust analysis of tree-level $2 \to n$, $n = 1, \ldots 6$, cross sections and simulation of such events at colliders. The Lagrangian for NMWT was implemented using LanHEP [77], from which all interaction vertices are generated for use in CalcHEP. The model implementation is similar to the original implementation from Frandsen *et al*[70], with the addition of the features described in section 3.4.

We focus on the phenomenology of the neutral heavy spin-1 resonances in the NMWT parameter space presented in 2.33, with the additional restriction of $s = 0$. Where Higgs interactions are involved, we will loosen this constraint, however outside of this it is sufficient to consider the 3-dimensional M_A, $\tilde{g}$, S parameter space. The results are presented in the $M_A, \tilde{g}$ parameter space for discrete values of S in the range $S = -0.1, 0.0, \ldots, 0.3$, where $S = 0.3$ provides direct comparison to the previous work [66]. The remaining limits of the scan over S ensure that the tension with EWPD is minimised (for the zero T-paramter). The results in the benchmark case of $S = 0.1$ are presented here, and results for $S \neq 0.1$ are presented in Appendix C.

The purpose of this phenomenological study is to explore the potential for

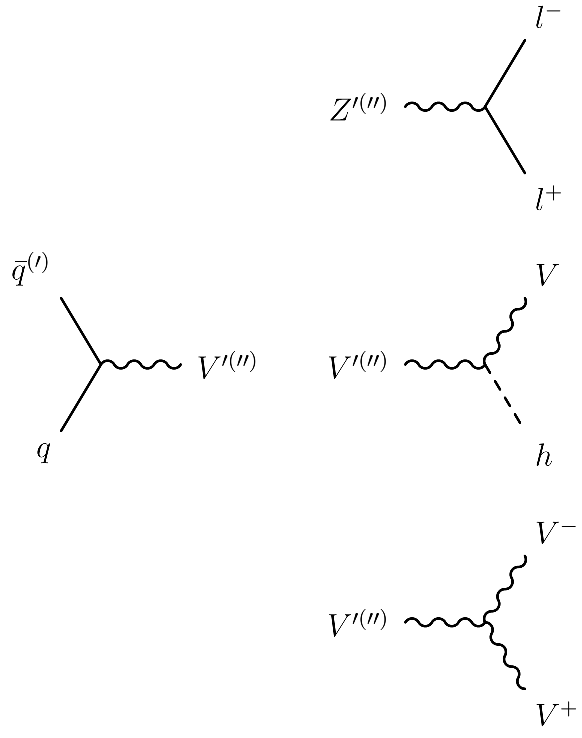

Table 4.1: Drell Yan production of heavy resonance (left) Dilepton, VV and Vh decay modes (right), where $V' = Z', W'^{+}, W'^{-}$ ($V'' = Z'', W''^{+}, W''^{-}$)

probing NMWT with heavy resonance searches at the LHC and future colliders. To this end, the set of diagrams we are interested in are those of Drell-Yan produced heavy resonances that subsequently decay via dilepton, vector-vector, and vector-Higgs channels. The full set of Feynman diagrams we are interested in are given in Figure 4.1.

The mass spectra of the Z'/Z'' are presented in section 4.1, the coupling strength of Z'/Z'' vertices in section 4.2, followed by a discussion of the total widths and dilepton branching ratios in section 4.3, production and total cross sections for DY processes of Z'/Z'' are given in section 4.4, section 4.5 explores the interference between the neutral resonances and discusses the validity of reinterpreting LHC constraints for the NMWT model.

4.1 Mass Spectrum

Following from the analytic diagonalisation performed in section 3.2, analytic mass terms for the neutral resonances can be constructed. Note that we first discuss here the regime with mass ordering $M_A < M_V$. The 0th and 2nd order corrections to the Z' and Z'' derived in section 3.2 (equation 3.16) combine to give the masses

$$M_{Z'}^2 = M_A^2 \left(1 + \frac{g_1^2 + g_2^2}{2\tilde{g}^2}\chi^2\right), \tag{4.1}$$

$$M_{Z''}^2 = M_A^2 \left(1 + \frac{g_1^2 + g_2^2}{2\tilde{g}^2}\right)\left(\chi^2 + \frac{\tilde{g}^2 F_\pi^2}{2M_A^2}\right), \tag{4.2}$$

up to $\mathcal{O}(\tilde{g}^{-2})$. It is clear from equation 4.1 that at 0th order in $\tilde{g}^{-1}$, $M_{Z'}$ is exactly equivalent to M_A, so the mass scale of NMWT is defined by the mass of the lighter of the new neutral resonances.

As discussed in section 3.3, the $U(1)_Y$ and $SU(2)_L$ couplings g_1, g_2 (see equations 3.21, 3.20) are functions of the NMWT parameters M_A, $\tilde{g}$, S. Both g_1 and g_2 have a very mild dependence on the model parameters, with variation in the couplings at less than 1% level across the viable parameter space. For the purpose of discussion and insight into the analytic behaviour of Z'/Z'' properties, we will consider g_1, g_2 fixed to their SM values, which in the $\bar{M}S$ scheme are $g_1 = 0.357$ and $g_2 = 0.652$[49]. Note that the properties calculated with CalcHEP use the full analytic form of these gauge couplings.

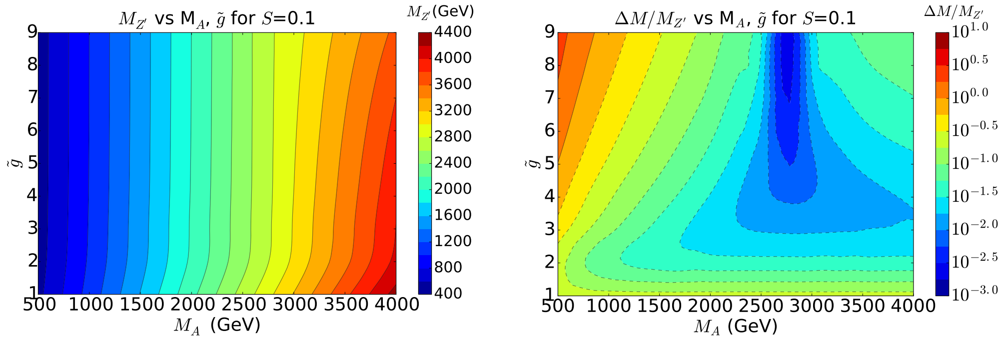

(a) (b)

Figure 4.1: (a) $M_{Z'}$(GeV) (b) $\Delta M/M_{Z'}$ as a function of M_A, $\tilde{g}$, at benchmark values of $S = 0.1$ and $s = 0$

The mass spectrum of the Z' is shown in Figure 4.1a for the mass range 500GeV$\leq M_A \leq$ 4000GeV. Again for the majority of the parameter space where $\tilde{g} \gtrsim 2$, $M_{Z'} \simeq M_A^2$ as expected from equation 4.1. In Figure 4.1b we present the spectrum for the relative mass difference, $\Delta M/M_{Z'}$, where

$\Delta M = M_{Z''} - M_{Z'}$. The behaviour of the mass splitting is due to the non-trivial dependence of $M_{Z''}$ on $\tilde{g}^2$, which arises from the χ and F_π^2/M_A^2 terms of equation 4.2. The effects of the $\tilde{g}^2$ dependence are in ‘competition’ with the S and M_A^{-2} coefficients, leading to an enhanced quadratic dependence - and as such enhanced mass splitting - in the low M_A, high $\tilde{g}$ regime.

For large M_A one can observe that Z' starts to mildly depend on $\tilde{g}$. This change in behaviour is due to a change of state of the $Z'(Z'')$ from mostly axial(vector) to mostly vector(axial)[66]. Figure 4.1b clearly reflects this mass inversion for $\tilde{g} \geq 2$ at a fixed $M_{inv} = M_A$ which to 2nd order in $\tilde{g}^{-1}$ takes the form

$$M_{inv}^2 = \left(1 + \frac{g_1^2 + g_2^2}{\tilde{g}^2}\right) \frac{4\pi}{S} F_\pi^2. \tag{4.3}$$

Using the benchmark $S = 0.1$ the mass inversion occurs at $M_A = 2760$GeV, we clearly observe this behaviour in Figure 4.1b.

The mass splitting is large at low M_A, high $\tilde{g}$, opening new decay channels such as $Z'' \to W^{+\prime} W^{-\prime}$, as is discussed further in section 4.3.

We also numerically presented the Z' and Z'' masses in Table 4.2 for a range of points in the 3D parameter space of $M_A, \tilde{g}, S$, restricting the results to the $M_A < M_{inv}$ regime. Qualitatively, one can see that varying S affects the Z'' mass spectrum, reducing $M_{Z''}$ as S increases, but increasing the mass when S becomes negative. This is due to the contribution to the χ^2 factor in $M_{Z''}$, which is proportional to $1 - \tilde{g}^2 S$. The effect of S is most prominent at large M_A, where the $F_\pi^2 \tilde{g}^2 / 2M_A^2$ is suppressed and the enhancement/suppression due to S becomes the dominant effect. The $M_{Z'}$ is only affected by S at 2nd order in $\tilde{g}^{-1}$, so away from the mass inversion where Z' is a more pure axial mode, the deviation from vector/axial degeneracy is reflected in the vector (Z'') mass behaviour.

4.2 Coupling Strengths

The couplings of the neutral resonances in fermion and gauge sector interactions are constructed from the elements N_{ij} of the diagonalisation matrix $\mathcal{N}$. Each element of N_{ij} (and C_{ij} in the charged sector) represent the mixing of the vector boson/meson states, e.g N_{24} represents a mixed $Z - Z''$ state, and components with $i = j$ represent mixing of a gauge field with itself. By inspecting the analytic behaviour of the interaction vertex couplings, features of the phenomenology of widths/branching ratios etc can be explained from

		M_A(GeV)			
S	$\tilde{g}$	1000	1500	2000	2500
-0.1	1	1080(1339)	1614(1984)	2148(2639)	2683(3296)
	3	1016(1163)	1523(1640)	2030(2138)	2536(2643)
	5	1006(1370)	1509(1808)	2012(2283)	2515(2778)
	7	1003(1642)	1505(2049)	2007(2510)	2508(3001)
	9	1002(1947)	1503(2334)	2005(2788)	2506(3280)
0.1	1	1078(1325)	1610(1976)	2144(2629)	2678(3283)
	3	1015(1130)	1520(1590)	2023(2071)	2522(2565)
	5	1005(1295)	1507(1678)	2010(2100)	2511(2543)
	7	1002(1518)	1503(1821)	2004(2175)	2505(2560)
	9	1001(1773)	1502(1998)	2002(2277)	2503(2591)
0.3	1	1075(1320)	1607(1968)	2139(2618)	2672(3270)
	3	1013(1097)	1514(1541)	1985(2034)	2452(2540)
	5	1004(1215)	1505(1537)	1898(2008)	2280(2510)
	7	1001(1382)	1502(1560)	1779(2002)	2025(2503)
	9	1000(1580)	1500(1593)	1611(2000)	1634(2500)

Table 4.2: Masses of the neutral resonances at reference points in the $M_A, \tilde{g}, S$ parameter space, displayed in the format $M_{Z'}(M_{Z''})$ in GeV for each parameter space value

a fundamental perspective. Here we discuss the analytic forms of the coupling strengths at interesting vertices, and in section 4.3 their effect on the branching ratios and widths are further explored. Ultimately, the strength of the neutral vector meson couplings will define how best to probe the parameter space of NMWT with collider observables, and inform the experimental searches on the relevant production and decay channels for the Z' and Z''.

4.2.1 Z'/Z'' Fermionic Coupling

Couplings of the heavy neutral resonances to fermions are important to understand for interpretation in collider searches, such as $Z'(Z'')q\bar{q}$ for analysis of Drell-Yan production and the charged lepton coupling for dilepton final state searches. The $Z'(Z'')e^+e^-$ coupling is composed of left and right handed pieces, which can be individually numerically explored in the NMWT parameter space. The $Z'e^+e^-$ LH and RH couplings as a ratio to their SM Ze^+e^- counterparts are presented in Figure 4.2a and 4.2b respectively. Both L and R components of the Z' dilepton coupling increase as $\tilde{g} \to 1$, however as the coupling is diluted through the mixing effects between the gauge fields, $g_{Z'l^+l^-} \geq g_{Zl^+l^-}$ is never realised.

Figures 4.3a and 4.3b show the LH and RH Z'' dielectron coupling in the $M_A, \tilde{g}$ parameter space, again presented as a ratio to the SM Ze^+e^- coupling.Similarly, the L component of the Z'' dilepton coupling grows as $\tilde{g} \to 1$, however this is not the case for the R component. The R component is suppressed in comparison to the Z' as the mixing with the photon is smaller for $\gamma - Z''$ than $\gamma - Z'$.

Figures 4.2 and 4.3 clearly confirm the switch from axial(vector) to vector(axial) $Z'(Z'')$ at the mass inversion, M_{inv}. The composition of the neutral resonances affect both LH and RH coupling strengths, suppressing the coupling as the $Z'(Z'')$ becomes mostly vector(axial).

In order to understand the relative suppression one should inspect the analytic forms for the dilepton couplings in the regimes of $M_A < M_{inv}$ and $M_A > M_{inv}$. The LH/RH dilepton couplings are constructed as

$$g^L_{Z'e^+e^-} = \frac{1}{4}(N_{13}g_1 + N_{23}g_2), \quad g^R_{Z'e^+e^-} = \frac{1}{2}N_{13}g_1, \tag{4.4}$$

where for the Z'' the mixing elements switch to $N_{i3} \to N_{i4}$.

From this equation 4.4, we see that the $Z'-$dilepton couplings are built from the mixing of the $U(1)_Y$ gauge boson with the Z' and the mixing of $Z - Z'$.

In fact, all fermionic couplings follow a similar structure, containing only off-diagonal terms of the mixing matrix $\mathcal{N}$. This mixing is the origin of the hypercharge and isospin components of the fermionic couplings, hence we can generalise the fermionic couplings of Z' and Z'' in a mass regime dependent way.

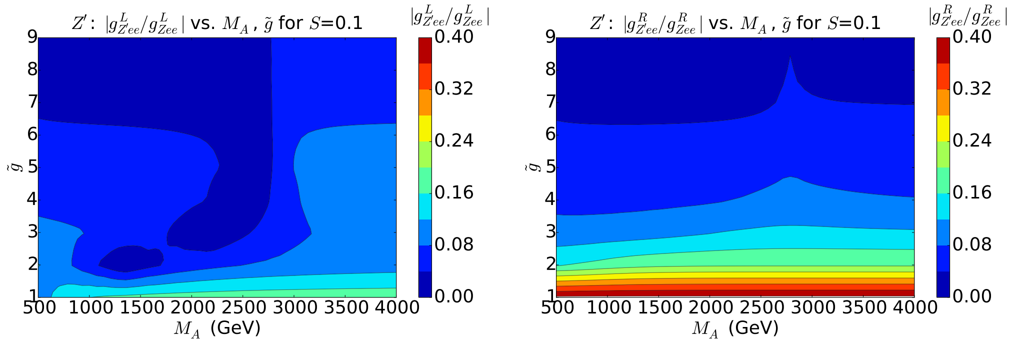

(a) (b)

Figure 4.2: Coupling of Z' to charged lepton pairs as a ratio to its SM equivalent separated into left and right handed components, (a) $\mid g^L_{Z'l^+l^-}/g_{Zl^+l^-} \mid$, (b) $\mid g^R_{Z'l^+l^-}/g_{Zl^+l^-} \mid$, as a function of M_A and $\tilde{g}$ parameters at the benchmark values of $S = 0.1$ and $s = 0$

$M_A < M_{inv}$ regime

In the mass regime $M_A < M_{inv}$, the generalised Z'/Z'' fermionic couplings $g_{Z'f\bar{f}}$ and $g_{Z''f\bar{f}}$ take the form

$$g^L_{Z'f\bar{f}} = \frac{\chi}{2\sqrt{2}\tilde{g}} \left(-I_3 g_2^2 + Y g_1^2\right), \qquad g^R_{Z'f\bar{f}} = \frac{\chi}{2\sqrt{2}\tilde{g}} q_f g_1^2, \tag{4.5}$$

$$g^L_{Z''f\bar{f}} = \frac{1}{2\sqrt{2}\tilde{g}} \left(I_3 g_2^2 + Y g_1^2\right), \qquad g^R_{Z''f\bar{f}} = \frac{1}{2\sqrt{2}\tilde{g}} q_f g_1^2, \tag{4.6}$$

where $I_3 = \pm 1/2$ is usual 3rd component of the weak Isospin for up and down-fermions respectively, $Y = q_f - I_3$ is their hypercharge, and q_f is the charge of the fermions.

Compounding the results of the numeric analysis, in the low $\tilde{g}$ region the Z'' dilepton coupling is stronger than that of the Z', due to the χ suppression in the Z' couplings. For positive S, then $\chi < 1$ across the full parameter space, so represents a small suppression where it appears in the coupling.

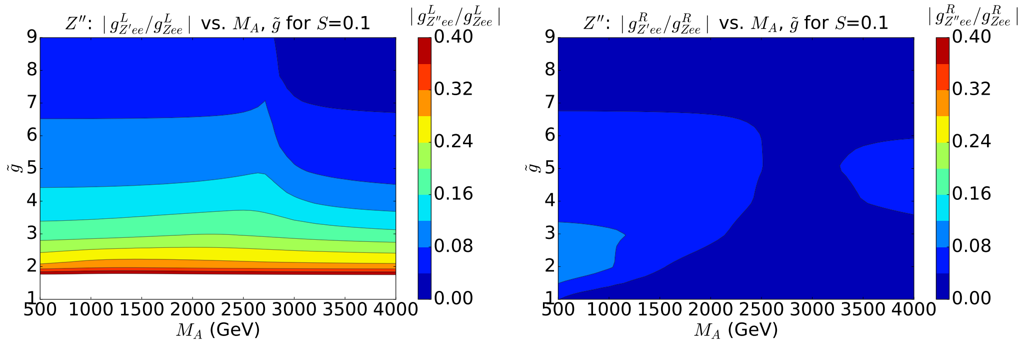

(a) (b)

Figure 4.3: Coupling of Z'' to charged lepton pairs as a ratio to its SM equivalent separated into left and right handed components, (a) $\mid g^L_{Z''l^+l^-}/g_{Zl^+l^-} \mid$, (b) $\mid g^R_{Z''l^+l^-}/g_{Zl^+l^-} \mid$, as a function of M_A and $\tilde{g}$ parameters at the benchmark values of $S = 0.1$ and $s = 0$

Thus when interpreting experimental limits in the NMWT parameter space, we would expect constraints at low $\tilde{g}$ region to be strongest from the Z''.

$M_A > M_{inv}$ regime

The couplings $g_{Z'f\bar{f}}$ and $g_{Z''f\bar{f}}$ in the $M_A > M_{inv}$ regime to order $\mathcal{O}(\tilde{g}^{-1})$ are

$$g^L_{Z'f\bar{f}} = \frac{1}{2\sqrt{2}\tilde{g}}\left(-I_3 g_2^2 + Y g_1^2\right), \qquad g^R_{Z'f\bar{f}} = \frac{1}{2\sqrt{2}\tilde{g}} q_f g_1^2, \tag{4.7}$$

$$g^L_{Z''f\bar{f}} = \frac{\chi}{2\sqrt{2}\tilde{g}}\left(I_3 g_2^2 + Y g_1^2\right), \qquad g^R_{Z''f\bar{f}} = \frac{\chi}{2\sqrt{2}\tilde{g}} q_f g_1^2. \tag{4.8}$$

The only major change in comparison to the $M_A < M_{inv}$ regime is that the factor χ is now applied to the Z'' fermion couplings. This leads to a relative suppression of the $Z''f\bar{f}$ interactions in comparison to the Z', with the greatest suppression occuring at high $\tilde{g}$ due to the structure of $\chi(\tilde{g}, S)$. This suppression of the Z'' dilepton couplings is present in Figure 4.3, especially notable for the LH coupling due to the contribution from $\gamma - Z''$ and $Z - Z''$ mixing.

4.2.2 Z'/Z'' VV/Vh Coupling

Additionally to the fermionic couplings, gauge sector interactions could play an important role in probing the NMWT parameter space at colliders. Alternatively to the Drell-Yan channel, the Z'/Z'' may be produced by Vector Boson Fusion (VBF), so one should investigate coupling to VV pairs. Interactions involving the Higgs may also provide interesting collider signatures, so we also study the Z'/Z'' coupling to Vh.

$Z'WW$

The $Z'W^+W^-$ vertex coupling has the structure

$$g_{Z'WW} = -g_2 C_{11}^2 N_{23} - \frac{\tilde{g}}{\sqrt{2}}(C_{21}^2 N_{43} + C_{31}^2 N_{43} + 2C_{21}C_{31}N_{33}). \tag{4.9}$$

Note that the $Z'WW$ vertex coupling has a linear momentum dependence, however here we present the dimensionless coupling coefficient to the momentum in this vertex.

In the $M_A > M_{inv}$ regime, substituting the elements of $\mathcal{N}$ and $\mathcal{C}$ from equations B.2 and B.3, the coupling becomes

$$g_{Z'WW} = \frac{g_2^2(1-\chi)}{\sqrt{2}\tilde{g}} - \frac{g_2^2(g_1^2 - g_2^2)M_V^2(\chi + \chi^3)}{\sqrt{2}\tilde{g}^3(M_A^2 - 4M_V^2)}, \tag{4.10}$$

which up to 2nd order in $\tilde{g}^{-1}$ simplifies to

$$g_{Z'WW} = \frac{g_2^2(1-\chi)}{\sqrt{2}\tilde{g}} + \mathcal{O}(\tilde{g}^{-3}). \tag{4.11}$$

As established previously, the SM-like gauge couplings g_1 and g_2 are minimally dependent on the WTC parameters M_A, $\tilde{g}$, and S, such that they can safely be considered constant for this discussion. With this approximation the coupling $g_{Z'WW}$ is independent of the mass scale M_A and fixed for a given $\tilde{g}$ and S.

The behaviour of $g_{Z'WW}$ as a function of $\tilde{g}$ is not obvious from equation 4.11, due to the non-trivial dependence of χ on the parameters S and $\tilde{g}$ (see equation 2.29). In the regime where both of the following conditions are met,

$$\tilde{g} \gg 1, \quad \text{and} \quad \frac{S\tilde{g}^2}{8\pi} \ll 1, \tag{4.12}$$

we can perform a Taylor expansion of χ around $\tilde{g}^{-1} = 0$,

$$\begin{aligned} \chi(gt, S) &= \sqrt{1 - \frac{S\tilde{g}^2}{8\pi}} \\ &\simeq 1 - \frac{S\tilde{g}^2}{16\pi} - \frac{S^2\tilde{g}^4}{512\pi} + \ldots . \end{aligned}$$

Taking only the leading terms and substituting into equation 4.11 we find the leading order (LO) behaviour of $g_{Z'WW}$ is

$$g^{LO}_{Z'WW} = \frac{g_2^2 S\tilde{g}}{16\sqrt{2}\pi}, \tag{4.13}$$

which in this regime (equation 4.12) describes the coupling behaviour to 1% level. Thus the $Z' \to WW$ interaction grows linearly with $\tilde{g}$ once $\tilde{g}$ is sufficiently large as to satisfy the expansion conditions.

In the $M_A < M_{inv}$ regime the Z' is the mostly axial-vector resonance, naturally one would expect this to result in the $Z'WW$ coupling being highly suppressed. Substituting the elements of $\mathcal{N}$ and $\mathcal{C}$ from equations 3.17, 3.18 into $g_{Z'WW}$ (equation 4.9), we find

$$g_{Z'WW} = \frac{g_2^2(g_1^2 - g_2^2)M_A^2\chi(1+\chi^2)}{\sqrt{2}\tilde{g}^3(4M_A^2 - M_V^2)}. \tag{4.14}$$

Immediately one can see that the coupling $g_{Z'WW}$ only contains $\mathcal{O}(\tilde{g}^{-3})$ contributions, i.e the contributions in which all particles are in a mixed state. Interestingly, the contribution from self-mixing W states ($C_{11}^2 N_{23}$ in equation 4.9) cancels *exactly* with the contribution from the self-mixing Z' state ($C_{21}C_{31}N_{33}$ in equation 4.9), leading to an overall zero contribution from the on-diagonal elements of $\mathcal{N}$ and $\mathcal{C}$.

The implication of this analysis is that the $Z'WW$ interaction becomes important in the high M_A, high $\tilde{g}$ regime. As the suppression of Z' fermionic couplings is $\tilde{g}^{-1}$ dependent, regions of the NMWT parameter space that cannot be effectively probed by fermionic couplings may be accessed through this triple vector particle coupling. The complementarity of fermionic and bosonic channels motivate the search for these new resonances at high energy colliders in both Drell-Yan (DY) and Vector-Boson Fusion (VBF) production channels.

$Z'Zh$

When the Z' is a mostly vector resonance, the dominant 3-point gauge interaction should be that of $Z'Zh$. In terms of mixing elements, the $Z'Zh$ coupling is constructed from elements of $\mathcal{N}$ in the following way;

$$\begin{aligned} g_{Z'Zh} =& \frac{v}{4}\Bigg(2g_2^2 N_{22}N_{23}(1+s) + 2g_1^2 N_{12}N_{13}(s-r_2)) + \frac{\tilde{g}^2 v}{2}(N_{32}N_{33}(r_2+s) \\ & - N_{22}N_{23}(1+r_2) + N_{42}N_{43}(s-r_2)\Bigg) \\ & + \frac{\tilde{g}v}{4}\Bigg(\sqrt{2}g_1(N_{13}N_{42}(r_2-s) + N_{13}N_{32}(s-1) + N_{12}N_{43}(r_2-s) + N_{12}N_{33}(s-1)) \\ & + \sqrt{2}g_2(N_{23}N_{32}(1-s) + N_{23}N_{42}(r_2-s) + N_{22}N_{33}(1-s) + N_{22}N_{43}(r_2-s))\Bigg), \end{aligned} \tag{4.15}$$

where we note that $g_{Z'Zh}$ has a mass dimension arising from the vev, as such it does not contain a momentum dependence as is the case for the $Z'WW$ vertex.

The form of equation 4.15 contains many terms as the coupling takes contributions from several operators in the Lagrangian 2.5, however if we apply the usual restriction of $s = 0$ this can be reduced. In the $M_A < M_{inv}$ regime, we can find an approximate asymptotic for $g_{Z'Zh}$ in terms of the 3-dimensional parameter space $(M_A, \tilde{g}, S)$,

$$g_{Z'Zh} = \frac{\tilde{g}M_A^2}{64v}\sqrt{\frac{(g_1^2+g_2^2)S}{\pi}}. \tag{4.16}$$

The key here is that the $Z'Zh$ coupling is enhanced by $\tilde{g}$ when the Z' is the mostly axial resonance, which could offer an exciting opportunity to probe the difficult to access high $\tilde{g}$ regime, where equivalent fermionic channels are suppressed by $1/\tilde{g}$. This suggests that the dominant process for the Z' at low-intermediate M_A is the decay to Zh, motivating the search for NMWT in a variety of neutral resonance searches.

4.3 Widths and Branchings

The validity of the low-energy effective Lagrangian 2.5 as a description of the NMWT parameter space is dependent on perturbativity of the model. A natural insight into whether interactions can be calculated perturbatively is the width of the neutral resonances - if the width is sufficiently small compared to the particle mass then perturbation theory holds and $\mathcal{L}_{boson}$ accurately describes the low energy behaviour of said particle. The width-to-mass ratio Γ/M for Z' and Z'' is shown in Figure 4.4.

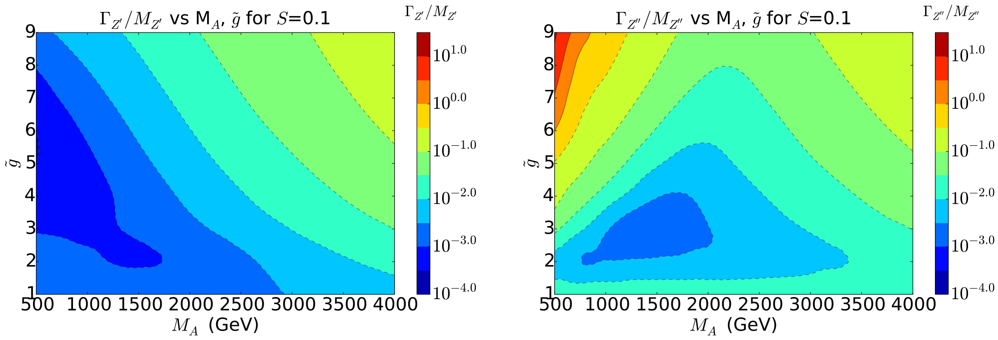

(a)

(b)

Figure 4.4: (a) $\Gamma_{Z'}/M_{Z'}$, (b) $\Gamma_{Z''}/M_{Z''}$ as a function of M_A and $\tilde{g}$ parameters at benchmark values of $S = 0.1$ and $s = 0$

One can see from Figure 4.4a that the Z' is narrow across the whole parameter space, and $\Gamma_{Z'}/M_{Z'}$ is always below 10%.

For $M_A > M_{inv}$, where the Z' is the mostly-vector resonance, its width is enhanced by the opening of the $Z' \rightarrow W^+W^-$ decay channel. $\Gamma_{Z'}$ is maximised for the high $\tilde{g}$ region of this mass regime, as we see from equation 4.13 $g_{Z'WW}$ is proportional to $\tilde{g}$. The Z' width is most narrow in the $M_A < M_{inv}$ and low $\tilde{g}$ regime, due to the suppression of the WW and Zh channels relative to the fermionic channels. In this regime, the dominant process of Drell-Yan to difermions forces the intermediate resonance to be narrow. This effect appears in the relative branching ratios of the Z', shown in Figure 4.5(a,b) for low $\tilde{g} = 3$ and high $\tilde{g} = 8$ respectively. This also occurs in

		M_A(GeV)			
S	$\tilde{g}$	1000	1500	2000	2500
-0.1	1	2.91(35.28)	4.54(52.92)	6.68(72.28)	9.76(94.34)
	3	1.29(10.79)	2.92(7.73)	7.20(12.28)	17.39(24.99)
	5	1.37(180.97)	5.10(117.65)	16.44(110.57)	44.28(143.36)
	7	2.89(932.69)	11.15(691.70)	35.46(648.36)	93.58(742.68)
	9	6.75(3028.96)	23.56(2435.70)	69.88(2375.84)	176.01(2685.93)
0.1	1	2.72(33.70)	4.02(48.98)	5.50(64.11)	7.50(79.44)
	3	0.88(4.13)	1.80(2.69)	4.74(6.40)	12.93(15.07)
	5	0.79(76.29)	3.60(19.00)	12.85(14.75)	36.46(36.86)
	7	1.99(350.34)	8.64(109.07)	28.30(46.82)	75.39(76.16)
	9	5.66(899.79)	19.44(328.60)	55.33(124.77)	134.68(135.22)
0.3	1	2.70(32.48)	4.62(47.28)	8.91(64.77)	19.03(90.61)
	3	1.87(2.75)	9.37(10.55)	34.98(37.18)	99.34(107.84)
	5	5.53(30.22)	27.87(27.69)	79.15(97.60)	197.15(288.29)
	7	18.16(108.87)	64.34(59.34)	113.87(195.62)	217.11(580.30)
	9	72.97(125.19)	160.17(109.98)	116.31(318.94)	124.76(617.72)

Table 4.3: Widths of the neutral resonances in the $M_A, \tilde{g}, S$ parameter space, displayed in the format $\Gamma_{Z'}(\Gamma_{Z''})$ in GeV for each parameter space value

the near-degenerate theory of $S \simeq 0$ as one can see from Figures C.9 and C.10 in Appendix C, where we present additional phenomenological results for $S = -0.1, 0, 0.2$ and 0.3. One should also note that for large $\tilde{g}$ and $M_A < M_{inv}$ the dominant contribution to the width is from the $Z' \to Zh$ decay channel, as shown in Figure 4.5b. The implication of the above is that the Z' decays via three important channels, dilepton, WW, Zh, which can probe complementary regions of the parameter space. As such, a fully comprehensive experimental search of the NMWT parameter space must consider these main signatures at collider experiments.

The behaviour of the Z'' width-to-mass ratio (Figure 4.4b) is qualitatively different from the Z'. For $\tilde{g} \lesssim 5$, the width also below 10% of $M_{Z''}$, however as $\tilde{g}$ grows beyond this range $\Gamma_{Z''}/M_{Z''}$ becomes very large. This is most extreme for the low M_A regime where $\Gamma_{Z''} > M_{Z''}$, due to the opening of the purely technicolor decay channel $Z'' \to W'^{+}W'^{-}$ which scales with $\tilde{g}$ (as the interaction vertex involves only technicolor gauge particles). The effect is confirmed in Figures 4.5(c,d), where for $\tilde{g} = 8$ and $M_A < 1$TeV all other channels are suppressed with respect to $Br(Z'' \to W'W')$.

For the $M_A > M_{inv}$ regime, the high $\tilde{g}$ regime is dominated by the $Z'' \to Zh$

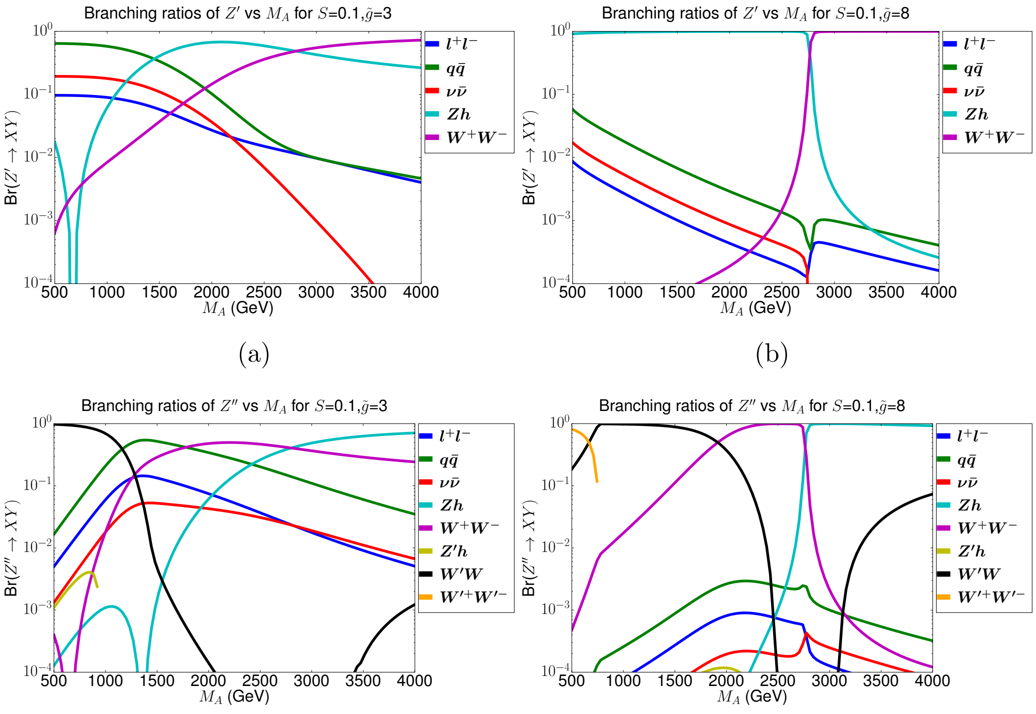

(a) (b)

(c) (d)

Figure 4.5: $Br(Z')$(a,b) and $Br(Z'')$(c,d) for all decay channels as a function of M_A at the fixed values of (a)$\tilde{g} = 3$, (b)$\tilde{g} = 8$, at benchmark values of $S = 0.1$ and $s = 0$

channel due to the $\tilde{g}$ enhancement in this coupling vertex and the axial-vector composition of the Z'' (Figure 4.5d). From Figure C.12 we see similar behaviour for $S \geq 0$, where the suppression of all other channels relative to Zh is greater for increased S, i.e as the mass separation of the Z' and Z'' is maximised. Interesting behaviour occurs for negative S (Figure C.12), where for $M_A > M_{inv}$ the dominant decay channel is $Z'' \to WW$. This is due to the definition that $M_{Z''} > M_{Z'}$ which means that to achieve a negative S, the mass ordering of M_A and M_V is switched - so at $M_A > M_{inv}$ the Z'' is the mostly-vector resonance.

The ultimate goal of this phenomenology analysis is to probe and assess the viability of the NMWT parameter space at collider experiments. The cleanest channel to explore is the charged dilepton signature, as it has a low SM background and narrow resonant peak in the invariant mass spectrum. Let us inspect the dilepton branching ratio for the Z' and Z'' resonances across the 2D (M_A, $\tilde{g}$) parameter space, presented for S=0.1 in Figure 4.6. We also present numerical results for $Br(Z' \to e^+e^-)$ and $Br(Z'' \to e^+e^-)$

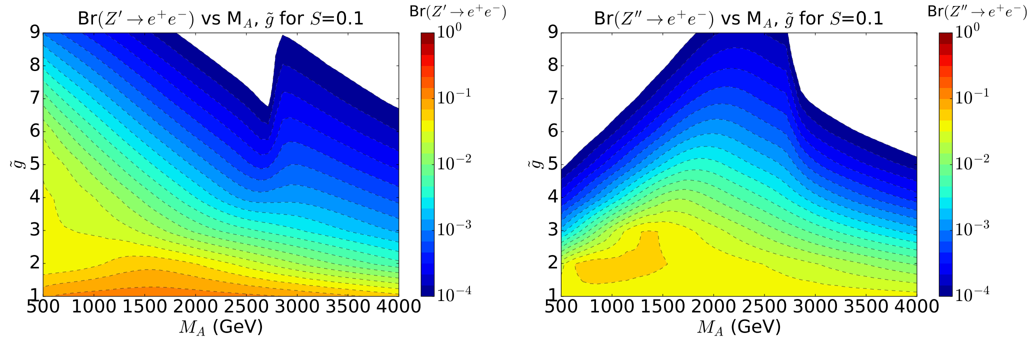

(a) (b)

Figure 4.6: (a)$Br(Z' \to e^+e^-)$, (b)$Br(Z'' \to e^+e^-)$ as a function of M_A and $\tilde{g}$ parameters at benchmark values of $S = 0.1$ and $s = 0$

at reference values across the 3D $(M_A, \tilde{g}, S)$ parameter space in Table 4.4.

The expected $1/\tilde{g}$ suppression from equations 4.5 and 4.6 is present in Figure 4.6. For low values of $\tilde{g}$ both $Br(Z' \to l^+l^-)$ and $Br(Z'' \to l^+l^-)$ are enhanced above the respective SM branching ratio $Br(Z \to l^+l^-)$ value of 3%. For example, from Table 4.4 we see that for $M_A = 1500$GeV, $S = 0.1$ and $\tilde{g} = 1$, $Br(Z' \to e^+e^-) \simeq 12.3\%$ which is ~ 4 times greater than the respective SM branching ratio. This enhancement is caused by a subtle effect in the mixing contributions to the vertex coupling, which is not evident from equation 4.5 as this equation breaks down for values of $\tilde{g} \sim 1$. A numerical analysis of the mixing contributions indicates that for $\tilde{g} \simeq 1$ the $\gamma - Z'$ mixing is enhanced, while $Z - Z'$ mixing is suppressed. This leads to a relative suppression of $Br(Z' \to \nu\bar{\nu})$ and $Br(Z' \to q_d\bar{q}_d)$ with respect to $Br(Z' \to l^+l^-)$ and $Br(Z' \to q_u\bar{q}_u)$.

Let us look beyond the dilepton channels $Br(Z' \to e^+e^-)$ and $Br(Z'' \to e^+e^-)$ to the interdependent branching ratios to VV and Vh. Along with the dominance of WW and Zh channels at high $\tilde{g}$ discussed previously, there is the presence of unusual dips in the Z' and Z'' diboson channels (Figure 4.5). These dips occur for low-intermediate $\tilde{g}$ and $M_A < M_{inv}$, and are the result of the respective $Z'^{('')}WW$ and $Z'^{('')}Zh$ couplings changing sign such that at the dips the respective branching ratios go to zero. The source of the sign change in the couplings can be investigated through the mixing contributions to the coupling vertex, i.e the contributions from N_{ij} and C_{ij} elements in the coupling. From equations 4.9 and 4.15 we see that the WW and Zh couplings contain contributions from gauge kinetic terms as well as from r_2 and r_3 terms from the Lagrangian of equation 2.5. These terms combine in such a way as

		M_A(GeV)			
S	$\tilde{g}$	1000	1500	2000	2500
-0.1	1	10.941(3.963)	10.759(3.873)	9.854(3.749)	8.467(3.576)
	3	2.226(0.782)	1.377(1.572)	0.704(1.313)	0.350(0.807)
	5	0.827(0.019)	0.327(0.038)	0.134(0.052)	0.061(0.049)
	7	0.217(0.002)	0.083(0.004)	0.035(0.005)	0.016(0.005)
	9	0.062(0.000)	0.026(0.001)	0.012(0.001)	0.006(0.001)
0.1	1	11.788(4.080)	12.280(4.112)	12.084(4.154)	11.119(4.174)
	3	2.986(1.991)	1.930(4.455)	0.903(2.487)	0.502(1.229)
	5	1.171(0.042)	0.373(0.220)	0.133(0.360)	0.050(0.183)
	7	0.211(0.005)	0.072(0.021)	0.029(0.058)	0.013(0.043)
	9	0.038(0.001)	0.016(0.005)	0.008(0.014)	0.004(0.015)
0.3	1	11.988(4.162)	10.784(4.186)	7.532(4.040)	4.429(3.595)
	3	1.255(2.910)	0.356(1.077)	0.301(0.233)	0.147(0.085)
	5	0.129(0.099)	0.033(0.142)	0.058(0.016)	0.028(0.006)
	7	0.012(0.016)	0.005(0.033)	0.019(0.002)	0.012(0.001)
	9	0.000(0.009)	0.000(0.011)	0.010(0.000)	0.010(0.000)

Table 4.4: Di-electron branching fraction of Z', Z'' in the $M_A, \tilde{g}, S$ parameter space, displayed in the format $Br(Z' \to e^+e^-)(Br(Z'' \to e^+e^-))$ in %.

to partially cancel the contributions, with the sign of the coupling indicating which Lagrangian terms are the greatest contribution, as such there is some value in the parameter space at which these contributions cancel exactly - hence the dips in the branchings.

4.4 Cross Sections

The Z' and Z'' resonances can be produced via the Drell-Yan production mechanism[78], where they can subsequently decay to dileptons. This DY dilepton signature is a promising probe of NMWT at proton-proton colliders such as the LHC, as such we study the theoretical DY dilepton cross sections for the Z' and Z'' in detail here. The cross sections are directly related to the fermionic couplings and dilepton branching ratios presented in sections 4.2.1 and 4.3 respectively. The total leading order (LO) cross sections for the $pp \to Z'/Z'' \to e^+e^-$ processes at 13TeV are presented in Figure 4.7, across the 2D $(M_A, \tilde{g})$ parameter space with $S = 0.1$. Analogous results are presented in Figures C.13 and C.14 for discrete $S = -0.1, 0.0, 0.2, 0.3$ (Appendix C). We also present numerically the DY production cross sections $pp \to Z'/Z'$ in Table 4.5 for the 3D grid $(M_A, \tilde{g}, S)$.

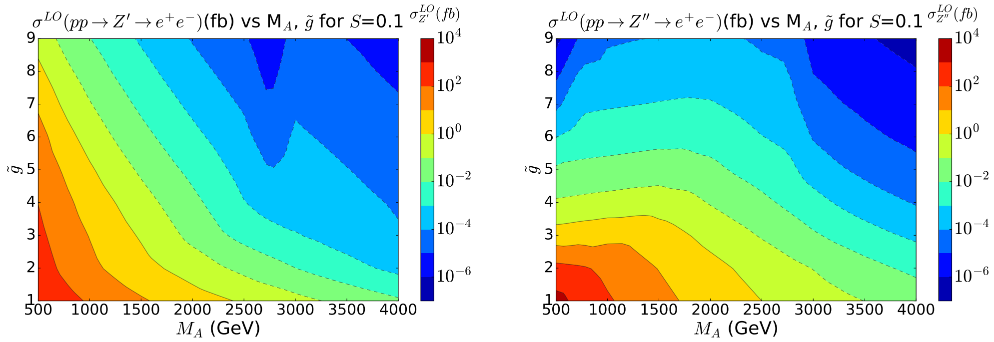

(a)

(b)

Figure 4.7: (a)$\sigma^{LO}(pp \to Z' \to e^+e^-)$ (fb)(b)$\sigma^{LO}(pp \to Z'' \to e^+e^-)$ (fb) at $\sqrt{s} = 13$TeV as a function of M_A, $\tilde{g}$ at benchmark values of $S = 0.1$ and $s = 0$

		M_A(GeV)			
S	$\tilde{g}$	1000	1500	2000	2500
-0.1	1	$6.37\times10^2(3.08\times10^3)$	$1.03\times10^2(4.29\times10^2)$	23.7(83.5)	6.54(19.1)
	3	$3.37\times10^2(2.39\times10^2)$	49.6(52.2)	10.4(14.1)	2.66(4.31)
	5	$1.43\times10^2(37.1)$	22.9(9.83)	5.29(2.84)	1.47(0.89)
	7	80.2(7.89)	13.0(2.54)	3.03(0.81)	0.85(0.26)
	9	53.9(2.00)	8.78(0.74)	2.05(0.25)	$0.58(8.59\times10^{-2})$
0.1	1	$6.39\times10^2(3.10\times10^3)$	$1.04\times10^2(4.34\times10^2)$	24.0(84.7)	6.64(19.5)
	3	$3.06\times10^2(2.72\times10^2)$	39.8(65.3)	5.79(20.0)	0.96(6.50)
	5	$1.17\times10^2(47.7)$	18.5(14.4)	4.03(4.72)	0.81(1.89)
	7	54.0(11.5)	8.75(4.70)	2.01(1.85)	0.52(0.76)
	9	27.7(3.22)	4.50(1.73)	1.05(0.85)	0.29(0.41)
0.3	1	$6.43\times10^2(3.12\times10^3)$	$1.05\times10^2(4.40\times10^2)$	24.3(85.8)	6.75(19.8)
	3	$2.70\times10^2(3.15\times10^2)$	16.1(93.9)	8.68(19.0)	3.47(4.70)
	5	90.4(63.2)	11.8(24.1)	6.98(3.82)	2.64(1.04)
	7	27.9(17.6)	4.30(10.2)	5.18(1.09)	2.64(0.31)
	9	1.35(5.65)	0.22(5.43)	$5.13(5.22\times10^{-2})$	$4.79(1.47\times10^{-2})$

Table 4.5: Cross section $\sigma(pp \to Z'/Z'')$ at LO in the $M_A, \tilde{g}, S$ parameter space at $\sqrt{s} = 13$TeV, displayed in the format $\sigma_{Z'}(\sigma_{Z''})$ in fb for each parameter space value

We evaluate the theoretical cross sections in the Narrow Width Approximation (NWA)[79] for consistency with the LHC@13TeV limits from the CMS experiment[80], which allows us to interpret the CMS limit in the NMWT parameter space. This interpretation is discussed further in chapter 5, with the relevant elements of the CMS procedure presented where appropriate here. The CMS paper itself follows the prescription of[81] to set appropriate mass window cuts around a generic resonant Z', where Accomando *et al* calculate that a cut of $M_{Z'} \pm 5\%\sqrt{s}$ produces a cross section that is within 10% of the calculation from the NWA. This discrepancy comes from the difference between a direct $2 \rightarrow 2$ cross section calculation, which does not necessarily have a sharp narrow resonance, and the $2 \rightarrow 1 \times Br(1 \rightarrow 2)$ method which forces the resonance to have a narrow width. We provide results for both procedures, where Figure 4.7 was calculated following the CMS $2 \rightarrow 2$ cross section procedure, and Table 4.5 is the $2 \rightarrow 1$ resonant production that one can apply the branching ratios from section 4.3 to create the dilepton cross section with an enforced narrow width.

Cross sections are calculated using the Matrix Element Generator package CalcHEP [76], using the platform of the High Energy Physics Model Database (HEPMDB) [82] which is linked to the Southampton based IRIDIS4 supercomputer. The PDF set used is NNPDF23 LO `as_0130_QED`[83], and we set the QCD coupling scale Q to be equal to the dilepton invariant mass, $Q = M(e^+e^-)$. To account for NNLO QCD effects we multiply the LO cross sections by a mass-dependent K-factor. This K-factor is found using the WZPROD program [84, 85, 86] which we have modified to evaluate Z' and W' cross sections, and linked to LHAPDF6 library [87] as described in [88]. These NNLO K-factors are presented in Table 4.6.

As expected, the $\tilde{g}^{-1}$ suppression from the dilepton coupling is observed for both Z' and Z'' in Figure 4.7. At high resonance mass there is also suppression of the cross section coming from the PDFs. It is important to note that for high M_A and low-intermediate values of $\tilde{g}$ the signal from the Z'' is higher than that of the Z', whereas the Z' dilepton signal is higher at low M_A and high $\tilde{g}$. This highlights the complementarity between the two resonances, indicating that the Z' and Z'' DY processes will exclude different areas of the NMWT parameter space. This motivates our study of both resonances in conjunction, as we will exclude a greater portion of the parameter space with combined searches.

$M_{Z'}$ (GeV)	K_{NNLO}
500	1.35
600	1.36
700	1.36
800	1.37
900	1.38
1000	1.39
1100	1.39
1200	1.40
1300	1.40
1400	1.41
1500	1.41
1600	1.41
1700	1.42
1800	1.42
1900	1.42
2000	1.41
2100	1.41
2200	1.41
2300	1.41
2400	1.40
2500	1.40
2600	1.39
2700	1.39
2800	1.38
2900	1.37
3000	1.36
3100	1.35
3200	1.34
3300	1.33
3400	1.32
3500	1.31
3600	1.30
3700	1.29
3800	1.28
3900	1.26
4000	1.25
4100	1.24
4200	1.22
4300	1.21
4400	1.19

Table 4.6: K-factors for NNLO QCD corrections to Drell-Yan cross sections at $\sqrt{s} = 13$TeV evaluated with the help of the modified ZWPROD program as described in the text, using NNPDF23 LO `as_0130_QED` and NNPDF23 NNLO `as_0119_QED`[3] PDFs for LO and NNLO cross sections respectively.

4.5 Z'/Z'' Interference

Following the discussion of the DY cross sections in section 4.4, it is vital to study the interference between the Z' and Z'' dilepton signatures. We will eventually interpret the LHC experimental limits on heavy neutral resonances in the context of the NMWT parameter space, where the experimental search is based on a *single* resonance in the dilepton channel. In conjunction with this, one must explore the separation of the neutral resonance peaks, their relative contributions to the dilepton signal, and their individual Γ/M ratio. As such, this section explores the validity of the single peak interpretation of experimental limits in the NMWT parameter space.

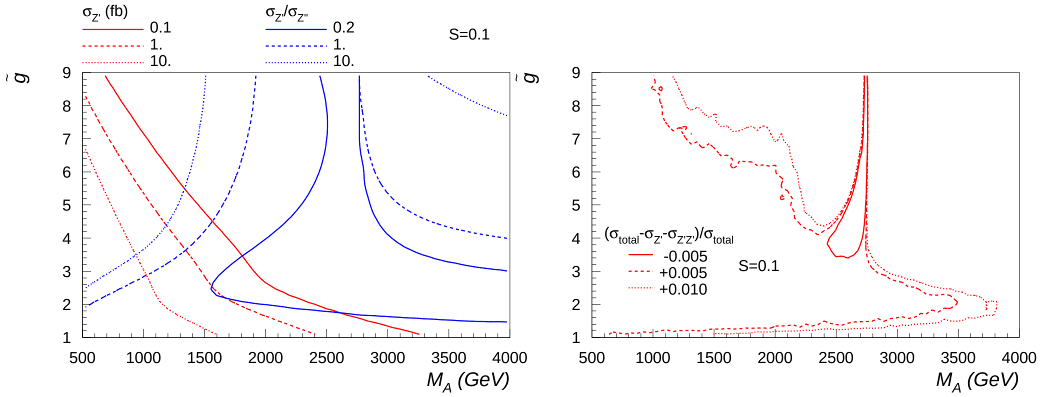

(a)

(b)

Figure 4.8: (a) Contour levels for $\sigma(pp \to Z' \to e^+e^-)$ at the $\sqrt{s} = 13$TeV and ratio of Z'/Z'' DY dilepton cross sections in $M_A, \tilde{g}$ parameter space at S=0.1. (b) Interference between Z' and Z'' contributions to the dilepton signature arising from the $pp \to Z'/Z'' \to l^+l^-$ process in $M_A, \tilde{g}$ parameter space at S=0.1.

In Figure 4.8(a) we present contour levels for $\sigma(pp \to Z' \to e^+e^-)$ at $\sqrt{s} =$ 13TeV along with the relative ratio of dilepton production via Z' vs. Z'' production for S=0.1. We calculate the cross sections with a finite width and a mass window cut around the resonance mass (following the procedure described in section 4.4), which allows us to correctly estimate the size of the Z'/Z'' interference. The pattern is qualitatively similar for varying S, so it is sufficient to explore the consequences of interference at $S = 0.1$ and apply it throughout. The result of Figure 4.8a is that the Z'' dilepton signature becomes dominant at mass regimes from $M_A > 1.5$TeV and low $\tilde{g}$, which confirms our results in section 4.4 and reaffirms the motivation to study the two resonances in parallel.

The interference between the Z' and Z'' contributions to the dilepton signature is presented in Figure 4.8b. One can clearly see that the interference is at most at the level of 1%, and can therefore be safely neglected across the whole $M_A, \tilde{g}$ parameter space at $S = 0.1$. Again, the results for $S \neq 0.1$ are qualitatively similar so the result applies for the full 3D $(M_A, \tilde{g}, S)$ parameter space.

Let us now consider the interpretation of the LHC limits in the Z' and Z'' dominated regions of the parameter space. In the region of low $M_A < 1$TeV the dominant contribution to the dilepton signature comes from the Z', so one can interpret the LHC single-resonance limits in this region of parameter space. Using similar logic, one can see that the region of $M_A > 1.5$ TeV the Z'' gives the dominant contribution to the di-lepton signature, thus one can interpret the LHC limits in this region of NMWT parameter space from the Z'' signal. Finally, in the intermediate region of 1TeV$\leq M_A \leq$ 1.5TeV the contributions from the Z' and Z'' dilepton signatures are comparable, however this does not invalidate the single peak interpretation. Recalling the relative mass ratio (Figure 4.1b), we see that the Z' and Z'' peaks are well separated in mass ($M_{Z''} > 10\% M_{Z'}$), and the width-to-mass ratios (Figure 4.4) are both at the percent level, as such the LHC limits in this region of parameter space can be applied *separately* to either the Z' or Z'' signatures.

Therefore we conclude that for the entire $(M_A, \tilde{g}, S)$ parameter space of interest, we can use signals from Z' or Z'' to independently probe complementary regions of the NMWT parameter space. In principle one can study the statistical combination of both Z' and Z'' signatures, however this is outside the scope of this thesis as it would require the experimental procedure to change. I would encourage the experimentalists to develop a procedure for a double-peak resonance search, as this may increase sensitivity to models with more than one heavy neutral resonance such as NMWT.

Chapter 5

Current LHC Limits

5.1 Set-up for LHC Limits

The potential of the LHC to probe the NMWT parameter space is dependent on the experimental set-up and assumptions used in creation of the experimental limits on new physics processes. We provide details of cuts, acceptance and efficiency functions etc. for each LHC@13TeV experimental search used for limit interpretation into the NMWT parameter space. Throughout this work the parton distribution functions used are as detailed in section 4.4. These will later be discussed in the context of probing NMWT with future colliders in chapter 7.

5.1.1 Dilepton set-up

The interpretation from experimentalists of dilepton limits in the NMWT parameter space was last provided by ATLAS at the LHC@8TeV [89]. Since this Run 1 result, experimentalists have not explicitly interpreted their own limits in the context of NMWT, so the following set-up applies for any generic Z' resonance in the DY dilepton channel, and for this study is specific to CMS[80].

The CMS limit on Z' resonances in the dilepton channel are expressed as a ratio of the DY di-electron cross section through a Z' mediator to the equivalent SM cross section through a Z mediator, $R_\sigma = \sigma(pp \to Z' \to e^+e^-)/\sigma(pp \to Z \to e^+e^-)$. Expressing the limit in this way removes the dependency of the limit on the theoretical prediction of the Z boson cross section, as well as experimental uncertainties associated with this dilepton measurement.

We simulate the limit setting procedure employed by CMS in order to validate the approach, with the projection to high energy/luminosity future colliders in mind. The following details our simulation of the CMS limits, which were found to match the CMS limit to $\sim 1\%$ level.

To reproduce these limits, the CMS mass distribution for the dilepton background is simulated using the background probability density function:

$$m^{\kappa} e^{\alpha+\beta m+\gamma m^2+\delta m^3+\epsilon m^4} \tag{5.1}$$

where $\kappa, \alpha, \beta, \gamma, \delta$ and ϵ are function parameters. This PDF describes a background distribution in the invariant di-electron mass, where the background is dominated by di-electron events produced via the Drell-Yan production mechanism. This simulated background is normalised with respect to the Z boson mass window ($60 < m_{ee} < 120$ GeV) in experimental vs. simulated data. For this reason, we set limits on the NMWT parameter space using the di-electron limits set by CMS at 13TeV and $36 fb^{-1}$.

For a given integrated luminosity L, the total number of events in the data is N_L. In this particular analysis the integrated luminosity is $L = 36 fb^{-1}$, however this procedure can be generically applied to any luminosity measured in the CMS detector. Using the PDF in equation 5.1 we generate many ($\mathcal{O}(100)$) data sets, where each data set has a total number of events equal to a varying Poisson fluctuation on N_L. For each data set, we step through invariant mass bins and set 95% confidence level (CL) limits on R_σ in each bin. To set these limits we employ an unbinned extended likelihood function using a Bayesian approach, where the likelihood function distribution is calculated as a function of the number of signal events, N_S, in a given mass bin. The signal PDF used in the likelihood analysis is a convolution of a Breit-Wigner function and a Gaussian function with exponential tails to either side, to simulate a single finite width Z' peak above the smooth background for a given mass bin. The size of the symmetric mass window is $\pm 6\Gamma_S$, where Γ_S is the width of the signal resonance, and in high invariant mass regimes this window is symmetrically enlarged to capture a minimum of 100 events within it.

We identify N_{95} as the 95% CL upper limit on the number of signal events N_S, where for a likelihood function $f(N;\theta)$ in a given mass bin, the upper limit N_{95} is the number of events at which

$$1-\alpha = 0.95 = \int_0^{N_{95}} f(N;\theta)dN. \tag{5.2}$$

In converting the upper limit N_{95} to a limit on the cross section ratio R_σ, one must consider the detector geometry and efficiency. These are modelled by the mass-bin dependent acceptance (A) and efficiency (ϵ) functions, more commonly quoted as a combined $A \times \epsilon$ function. The acceptance and efficiency are geometry dependent, and will have a different functional form for the barrel-barrel, barrel-endcap, and endcap-endcap regions of the CMS detector. The CMS detector identifies the regions of the electron calorimeter (ECAL) by the pseudo-rapidity regions $|\eta_C| < 1.44$ (ECAL barrel region) and $1.57 < |\eta_C| < 2.50$ (ECAL endcap), where the intermediate transition region $1.44 < |\eta_C| < 1.57$ between the barrel and endcap is excluded due to the physical set up of the calorimeters. We account for this in our simulations by calculating the SM background using separate CalcHEP batch mode scans for each of the regions of interest, and combining them in such a way as to accurately model the number of events N_L captured by the CMS detector in a given invariant mass window. Additionally, the selection criteria for di-electron events via a massive neutral mediator requires that the electrons both have a transverse momentum of $p_T > 35$GeV, again accounted for in the batch scan stage of our background simulation.

The cross section limit is then $N_{95}/(L \times A \times \epsilon)$. For each of the simulated data sets, we calculate a 95% CL upper limit on the cross section ratio in each mass bin. From these sets of limits we can then calculate the median 95% CL limit, as well as 1σ and 2σ standard deviations on the 95% CL limit at each invariant mass bin.

5.1.2 VV/Vh set-up

The Drell-Yan production of VV and Vh via $Z'^{(\prime\prime)}$ is simply the product of the DY production cross sections $\sigma(pp \to Z'/Z'')$ (Table 4.5) with the branching ratios $Br(Z'(Z'') \to W^+W^-)$ and $Br(Z'(Z'') \to Zh)$ (Figure 4.5). The batch mode calculation of the $2 \to 2$ process across a fine grid in $(M_A, \tilde{g}, S)$ is computationally expensive, instead one can reduce the calculation time from the $\sim \mathcal{O}$(hours) to $\sim \mathcal{O}$(seconds) by writing explicit C code interfaced with CalcHEP to produce all phenomenological results in a fine 3D grid. In this method, the production cross section is not calculated directly, rather it is reconstructed from the parton-level couplings to the $Z'(Z'')$, for example

$$\sigma(pp \to Z') = \Sigma_{q\bar{q}} \omega_{q\bar{q}}(M_{Z'}) g^2_{Z'q\bar{q}}, \tag{5.3}$$

where $\omega_{q\bar{q}}(M_{Z'})$ are the mass-dependent PDF functions for each pair of interacting quarks, and $g_{Z'q\bar{q}}$ are their coupling strengths to the Z'. The squared coupling implicitly combines left and right handed components as the sum of squares of LH and RH. The PDFs of parton processes are found by evaluating a smooth function of $\sigma(q\bar{q} \to Z'/Z'')$ with all couplings set to unity. This method was validated against the $2 \to 2$ calculation to within $\sim 1\%$ level.

One should also note that the involvement of the composite Higgs in this $V'Vh$ vertex necessitates the exploration of the parameter space with non-zero s. This additional parameter enters due to the $\mathrm{Tr}[C_{L\mu}^2 + C_{R\mu}^2]\mathrm{Tr}[MM^\dagger]$ term in the gauge sector Lagrangian (equation 2.5). For a qualitative view of how the s parameter affects the reach of LHC probes of NMWT, we will present the results in section 5.3 for $s = -1, 0, 1$.

5.2 Dilepton Limits on NMWT for LHC@13TeV

With the theory level NNLO cross sections for DY dilepton production of Z' and Z'' in section 4.4 and the CMS experimental set-up described in section 5.1.1, we can now explore the status of dilepton probes of the NMWT parameter space at Run 2 of the LHC. The 95% CL observed limit on $R_\sigma = \sigma(pp \to Z' \to e^+e^-)/\sigma(pp \to Z \to e^+e^-)$ at 13TeV and $36fb^{-1}$ can be found in Figure 3 of the CMS paper[80].

The SM NNLO cross section for the DY di-electron process is given as $\sigma(pp \to Z/\gamma^* \to e^+e^-) = 1.928\text{nb}$, which is then used to convert the ratio R_σ to a limit on $\sigma(pp \to Z' \to e^+e^-)$. This limit is then projected in the 2D $(M_A, \tilde{g})$ NMWT parameter space, interpolating the limit with di-electron invariant mass and mapping this to $M_{Z'}$ at each point in the parameter space. The 95% CL limit in the NMWT parameter space is then compared to the NNLO theoretical cross section for Z' and Z'' signals, and all regions in which the theoretical cross section is greater than the experimental limit are excluded.

The resulting exclusions on the NMWT $(M_A, \tilde{g})$ parameter space with $S = 0.1$ are presented in Figure 5.1. The power of the LHC to probe NMWT through dilepton searches is already powerful at low $\tilde{g}$, in fact for $\tilde{g} = 1$ the lower limit on the TC scale is $M_A \geq 3.5\text{TeV}$. This is also approaching the upper limit set by the a parameter, implying that the LHC could potentially completely close the parameter space for certain values of $\tilde{g}$, an exciting prospect that is explored further in the final chapter of this thesis (chapter 7). These exclusions also highlight the complementarity of the Z' and Z'', an important feature that is key to effectively probing the NMWT parameter space. As expected from the results of section 4.4, the Z' is more powerful for

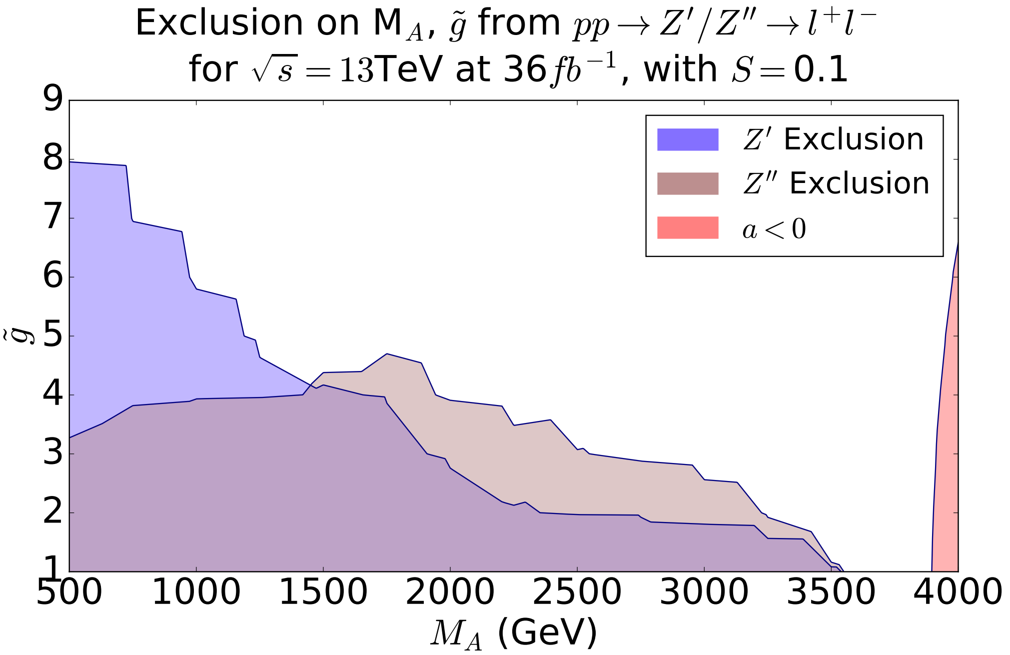

Figure 5.1: Exclusion of the $(M_A, \tilde{g})$ parameter space from Z' and Z'' DY processes in the dilepton channel at $\sqrt{s} = 13$TeV and luminosity of $36 fb^{-1}$

probing low M_A regimes up to high $\tilde{g}$, whereas the Z'' probes low-intermediate $\tilde{g}$ up to high M_A. This can also be observed for varying S, presented in Figure C.15 of Appendix C. When $S \neq 0$, the reach of the exclusions is similar in M_A but suppressed in $\tilde{g}$ to compensate for the deviation from degeneracy of the Z' and Z', whereas $S = 0$ significantly extends the exclusion region in both $\tilde{g}$ and M_A as the signal is boosted thanks to increased mixing between the near-degenerate neutral states. The a parameter limit probes lower in M_A for increasing S, so for large S the low $\tilde{g}$ regions of the parameter space can be fully excluded already, however one should keep in mind that EWPD disfavours $S \gtrsim 0.1$.

5.3 VV/Vh Limits on NMWT for LHC@13TeV

Analogously to the dilepton limits, we set the first limits on the NMWT parameter space from complementary signatures at the LHC. The analytic couplings presented in section 4.2.2 in conjunction with the relative branching ratios for Z'/Z'' decays (section 4.3) motivate the search for vector-vector (VV) and vector-Higgs (Vh) signatures. The potential for these searches to access the high $\tilde{g}$ regions of the (M_A, $\tilde{g}$) parameter space could provide a comprehensive study of the whole spectrum of possible Walking Technicolor models.

5.3.1 Drell-Yan produced Vh signatures

The Z' and Z'' can both decay to a Zh pair in complementary regions of the parameter space, with the coupling controlled by the vector/axial composition of the neutral resonance. When the Z' is the mostly axial resonance (i.e in the $M_A < M_{inv}$ regime) the Zh decay channel dominates for large $\tilde{g}$, and vice-versa for the Z'' in the $M_A > M_{inv}$ regime. DY production of Z'/Z'' remains the cleanest production mechanism, however there are a number of potential final states in which the $pp \to Z'/Z'' \to Zh$ signature can be explored at colliders. The signatures characteristic of Zh production in colliders include semi-leptonic final states, where the Higgs decays to pairs of b-jets or c-jets and the Z decays to dileptons, and the fully hadronic final states, where the Z decays to a pair of quark jets.

Here we consider the current limits on DY produced Z' in the Zh channel from the semi-leptonic ATLAS $Vh \to l\bar{l}b\bar{b}$ search at $\sqrt{s} = 13$TeV and $36fb^{-1}$[90]. This was chosen over the fully hadronic search and the equivalent CMS limits as at the time of writing, these are the strongest limits set on this channel, and the limit covers a large invariant mass range of $500 \leq M_{Zh} \leq 5000$GeV. The ATLAS limits are expressed as a limit on the cross section $\sigma(pp \to Z' \to Zh) \times Br(h \to b\bar{b}, c\bar{c})$, where the Higgs branching ratio is a sum over $b\bar{b}$ and $c\bar{c}$ decay modes and is fixed to $Br(h \to b\bar{b}, c\bar{c}) = 60.6\%$. Using this fixed branching fraction to convert the data to a limit on purely $\sigma(pp \to Z' \to Zh)$, we can then project the limit into the NMWT parameter space and compare to the theoretical $pp \to Z'/Z'' \to Zh$ cross section to produce exclusions on the model. The excluded regions from this search are given in Figure 5.2 for $s = -1, 0, 1$ and $S = 0.1$.

The first interesting observation is that the s parameter changes very little regarding the excluded regions, with the only observable effect appearing at very low $M_A < 1$TeV. In this region, the s parameter contributes negatively to the $pp \to Z' \to Zh$ cross section, boosting (suppressing) the cross section very slightly at $M_A \sim 500$GeV and $s = -1(1)$. This region of the parameter space is already excluded by the dilepton channel, so we can conclude that the $s = 0$ assumption can be safely applied for the purpose of this thesis.

Another interesting feature is the visible band of parameter space between the excluded regions that is allowed. This is due to the cancellation effect within

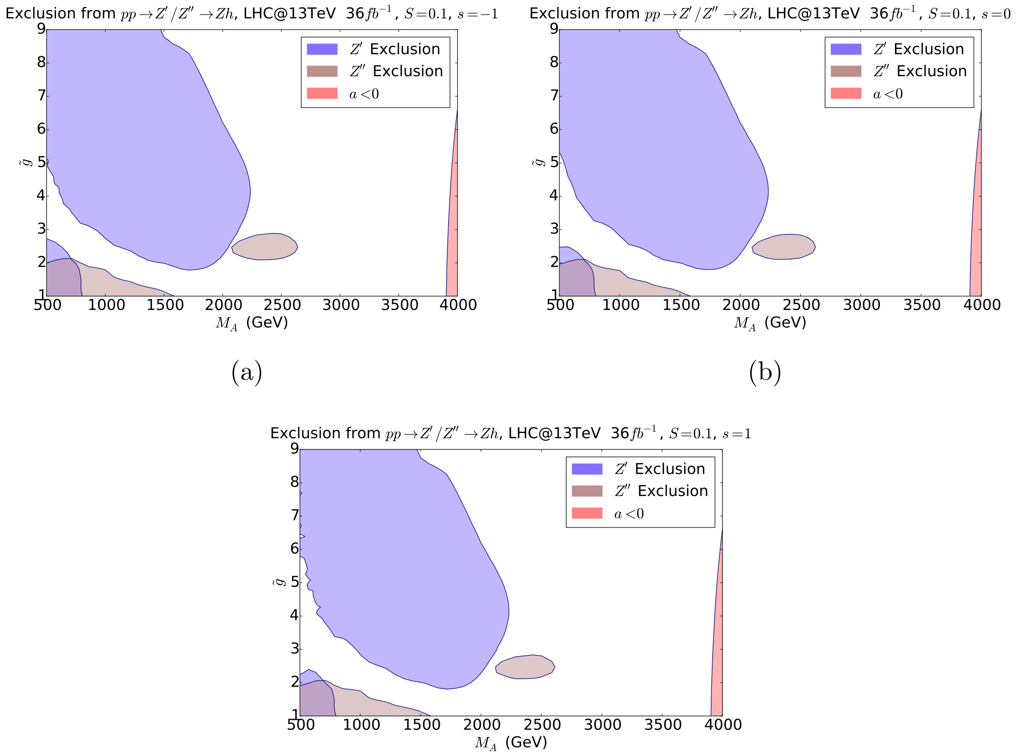

(a)

(b)

(c)

Figure 5.2: Exclusions on the $M_A, \tilde{g}$ parameter space from Z' and Z'' in the Zh channel at $\sqrt{s} = 13$TeV and $36 fb^{-1}$ with benchmark values of (a) $s = -1$, (b) $s = 0$, (c) $s = 1$, and $S = 0.1$, $\omega = 0$

the $Z'Zh$ coupling discussed in section 4.2.2, and is a 2D representation of the resulting ‘dips’ in the branching ratio (Figure 4.5).

Once can observe that the $Z' \to Zh$ in the mass regime $M_A < M_{inv}$ has the power to probe the high $\tilde{g}$ regime significantly better than the dilepton channel, again highlighting the complementarity of dilepton and Vh searches. As the Z'' is the mostly-vector resonance in the $M_A < M_{inv}$ parameter space, the Zh coupling is suppressed relative to the $Z'Zh$. However there is some small mixing between vector and axial states, so the Z'' does have some limited regions in which it can decay to Zh.

The semi-leptonic ATLAS search also sets limits on charged $V' \to Vh$ signatures in the DY production channel. Following a similar procedure to the one we employ for the $Z'^{(\prime\prime)}$, we interpret these limits in the NMWT parameter space for the W' and W'', presented in Figure 5.3. Similarly to the neutral resonance, the s parameter has only a small visible effect on the excluding power of the $W' \to Wh$ channel in the $M_A \simeq 500\text{GeV}$ regime. We can superficially note that this regime is saturated by the exclusions from DY dileptons, so the s parameter is of little import. The charged resonances increase the exclusions for the mass region $M_A \simeq 2\text{TeV}$ in comparison to their neutral counterparts. Although this complementarity is not as significant as that of the mass-ordered resonances V' and V'', this observation motivates the extension of our triple-vector searches to the charged resonances.

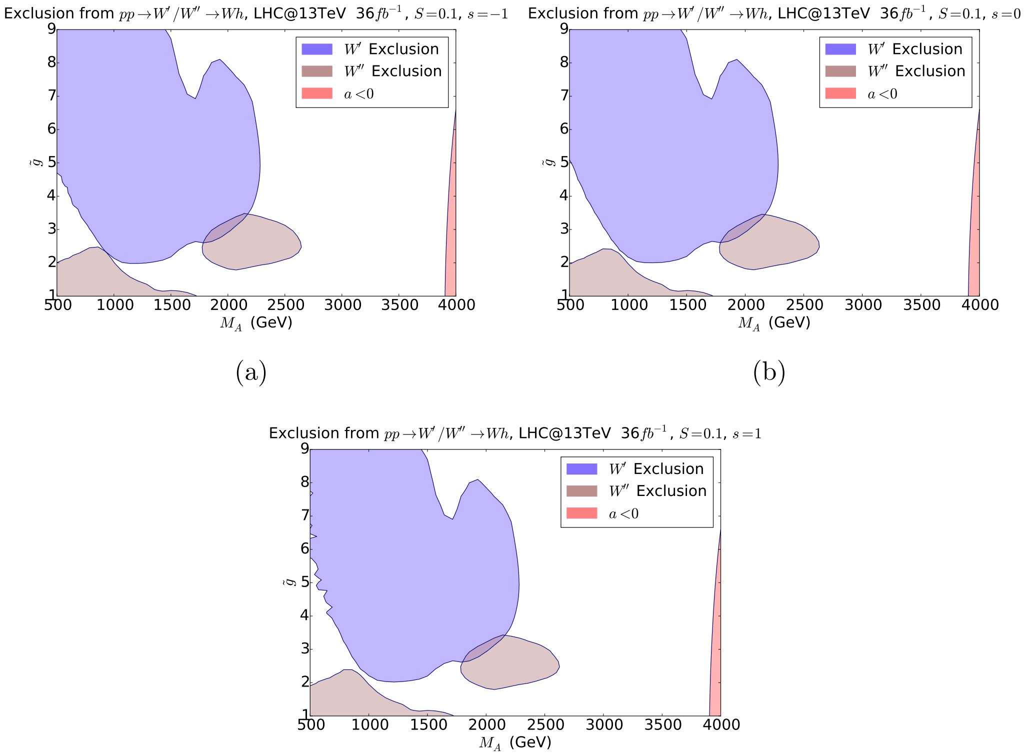

(a) (b)

(c)

Figure 5.3: Exclusions on the $M_A, \tilde{g}$ parameter space from W' and W'' in the Wh channel at $\sqrt{s} = 13\text{TeV}$ and $36 fb^{-1}$ with benchmark values of (a) $s = -1$, (b) $s = 0$, (c) $s = 1$, and $S = 0.1$, $\omega = 0$

5.3.2 Drell-Yan produced VV signatures

Analogously to the Vh channel, one can set limits on NMWT from LHC searches for heavy resonances in the DY VV channel. In the $M_A < M_{inv}$ regime the Z' coupling to W^+W^- is heavily suppressed (see section 4.2.2), so we expect that the Z' will not provide any limits in this mass regime. Although there is potential for this coupling to grow with $\tilde{g}$ when in the $M_A > M_{inv}$ regime, the cross section $\sigma(pp \to Z' \to WW)$ is inherently limited by the DY production mechanism, due to the suppression of the $Z'q\bar{q}$ coupling. One can expect that the Z'' will be able to probe the $M_A < M_{inv}$ parameter space due to its mostly-vector composition. As evident from Figure4.5c,d in section 4.3, the branching ratio to the WW channel is dominant for intermediate M_A, so we expect that this channel will be able to probe the parameter space of 1TeV$\leq M_A \leq M_{inv}$.

For the LHC@13TeV and $36fb^{-1}$, the ATLAS Collaboration provide the best current limits on W' and Z' resonances in the VV channel, again in the semi-leptonic final state $l\nu qq$ [91]. This search is sensitive to invariant mass ranges of 0.5-5TeV, so can be interpreted for the whole M_A range of interest in the NMWT parameter space. The experimental 95% CL limit is given explicitly as a limit on $\sigma(pp \to V' \to VV)$ for $Z' \to W^+W^-$ and $W' \to WZ$ respectively, to which we simply apply conversion from $fb \to pb$. We interpret this limit in the M_A, $\tilde{g}$ parameter space for neutral resonances in Figure 5.4, and charged resonances in Figure 5.5.

As expected, the Z' does not produce any limit on NMWT in the WW channel, however the W' does provide a limit in a small region of parameter space around $\tilde{g} \sim 2.5$ and $M_A \sim 1.2$TeV. Although the phenomenology is qualitatively similar between the neutral and charged technicolor resonances, in this region of parameter space $Br(W' \to WZ) \sim 10^{-2} - 10^{-1}$ as opposed to $Br(Z' \to WW) \sim 10^{-3} - 10^{-2}$. The Z' is more suppressed due to its axial-vector composition which leads to a highly suppressed WW coupling, whereas the W' is not limited by such composition as it is necessarily a vector meson. The Z'' and W'' exclude almost entirely identical regions of the parameter space, probing the $2 \leq \tilde{g} \simeq 5$ for as high as $M_A = 2.5$TeV. The reach in the low M_A regime is poor as the VV channel is suppressed relative to decays of V'' to $V'V^{(\prime)}$, whose couplings grow with $\tilde{g}$. Once these Technicolor decay channels close, the VV channel becomes the dominant one for both neutral and charged resonances. At this point the limitation is set by the DY production channel, hence the unprecedented reach in the $\tilde{g}$ regime.

5.3.3 Combined reach of VV/Vh limits on NMWT

In this section we have discussed the potential to probe the NMWT parameter space from the individual VV and Vh searches, as well as the effect of the non-zero s parameter on these exclusions. The conclusion we can draw is

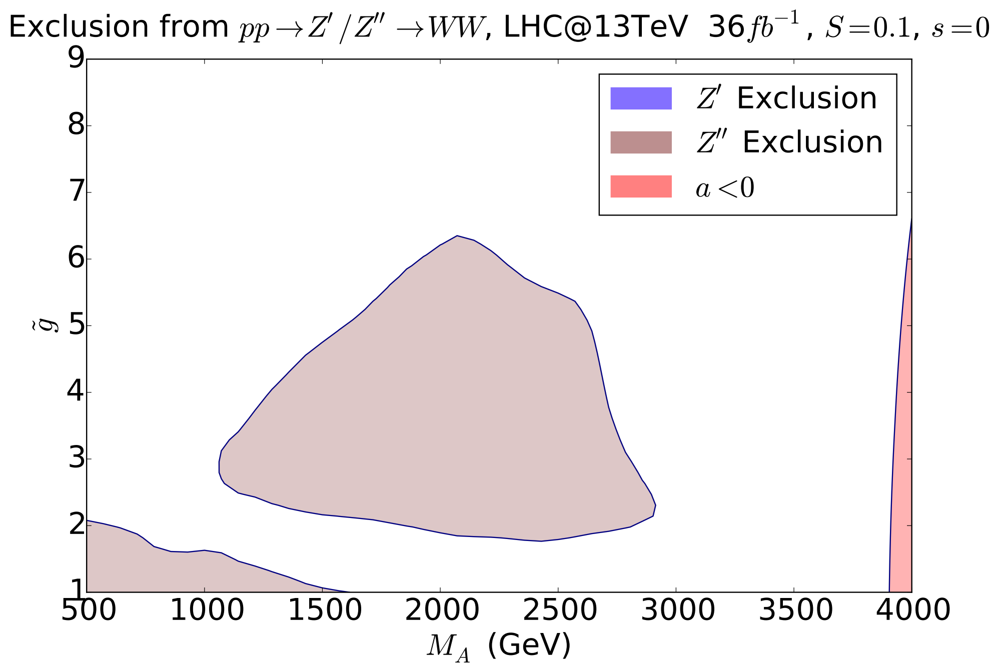

Figure 5.4: Exclusions on the $M_A, \tilde{g}$ parameter space from Z' and Z'' in the W^+W^- channel at $\sqrt{s} = 13$TeV and $36 fb^{-1}$ with benchmark values of $s = 0$, $S = 0.1$, $\omega = 0$

that $s \neq 0$ either has no effect on the overall excluded regions, or contributes to the very low $M_A \simeq 500$GeV regime. This regime is already covered by the dilepton limits presented in section 5.2, so any effect on Vh exclusions from the s parameter is saturated by complementary channels. As such, one can examine the combined reach of all DY produced VV and Vh probes at $s = 0$ without loss of generality.

The combined exclusion on the NMWT $(M_A, \tilde{g})$ parameter space is presented in Figure 5.6 for $S = 0.1$ and $s = 0$. Here the results from neutral resonances and charged resonances for a given channel are coded with the same colour, where the darkened regions for that channel represent the parameter space that is excluded by both resonances in that channel. For example, the $V' \to Vh$ exclusion region in purple has a large region of $M_A < 2$TeV parameter space that is excluded by both $Z' \to Zh$ and $W' \to Wh$, with additional complementary exclusions from the individual channels.

The full picture of the new limits we have set on the NMWT parameter space

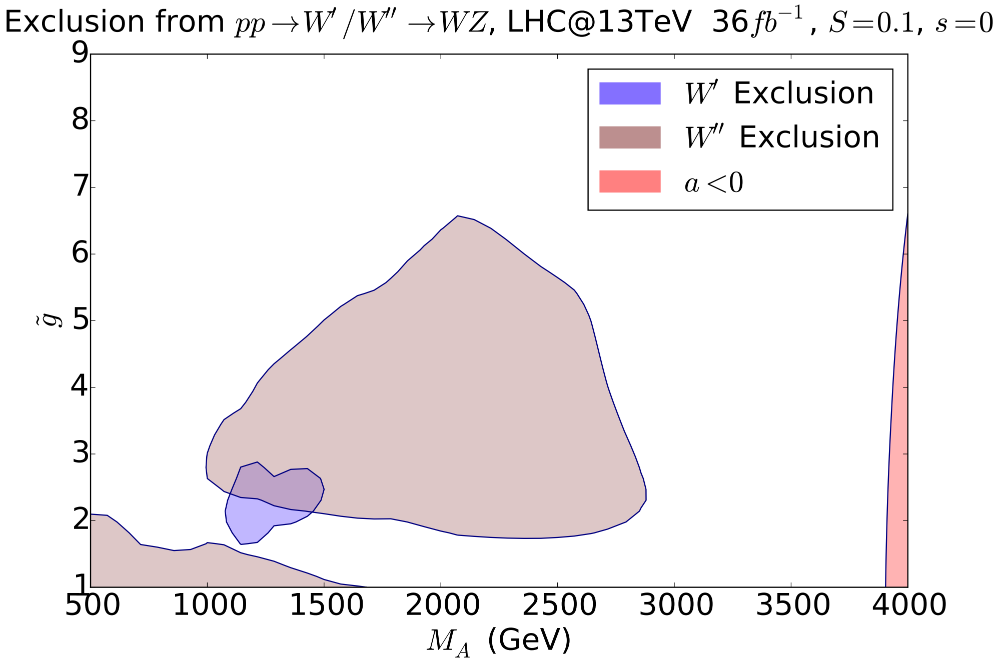

Figure 5.5: Exclusions on the $M_A, \tilde{g}$ parameter space from W' and W'' in the WZ channel at $\sqrt{s} = 13$TeV and $36fb^{-1}$ with benchmark values of $s = 0$, $S = 0.1$, $\omega = 0$

from all DY produced channels is given in Figure 5.7. The $VV + Vh$ combined channels probe the high $\tilde{g}$ region of the parameter space very effectively, with Vh limits covering all $\tilde{g} > 4$ at $M_A \leq 1.5$TeV, and VV limits can exclude up to $\tilde{g} \simeq 5$ as high as $M_A \sim M_{inv} \sim 2.7$TeV. In combination with the dilepton limits which are sensitive to the low M_A regime and low-intermediate $\tilde{g}$, this means that already with LHC@13TeV at $36fb^{-1}$ we can exclude almost the entire $M_A < M_{inv}$ parameter space[1]. Additionally, experimental limits on $\sigma(pp \to V'/V'' \to VV)$ and $\sigma(pp \to V'/V'' \to Vh)$ have never been interpreted into the NMWT parameter space previously, so we have conclusively demonstrated that the combination of complementary channels is essential in the endeavour to discover (or completely exclude) the Walking Technicolor paradigm.

---

[1] Note that this is for the benchmark value of $S = 0.1$. As discussed in the main text, the s parameter does not extend/affect the total exclusions from all channels, so we set $s = 0$.

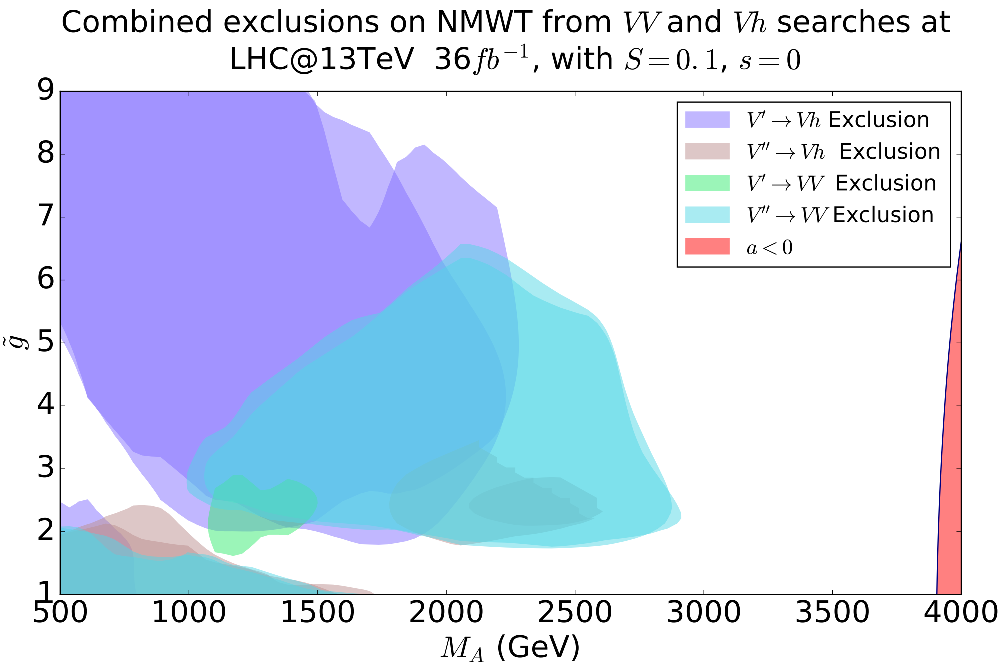

Figure 5.6: Combined exclusions on the $M_A, \tilde{g}$ parameter space from Drell-Yan $V'(V'') \to Vh$ and $V'(V'') \to VV$ channels at $\sqrt{s} = 13$TeV and $36fb^{-1}$ at benchmark values $S = 0.1$, $s = 0$, $\omega = 0$

5.4 Always Allowed/Always Excluded NMWT Limit Analysis

To explore the sensitivity of the LHC@13TeV searches for heavy resonances to the *whole* NMWT parameter space we perform scans over the full 5D $(M_A, \tilde{g}, S, s, \omega)$ parameter space, generating $\mathcal{O}(10^7)$ random points for each of the dilepton, VV, and Vh theoretical cross sections. The random scan covers the parameter space of S ranged from $(-0.1, 0.3)$, s ranged $(-1, 1)$, and ω between $(0, 0.01)$. We then project these theoretical cross sections into the usual $M_A, \tilde{g}$ plane, apply the appropriate LHC limits, and evaluate the most conservative and most optimistic limits from each individual search. For the most conservative limits, we layer the points that are allowed after applying the experimental 95% CL limits on top of those that are excluded from the Z' or Z'', such that the excluded points that remain are excluded for all possible combinations of S, s, ω. We also present the reverse of this, where the excluded points are layered on top of the allowed points, so the

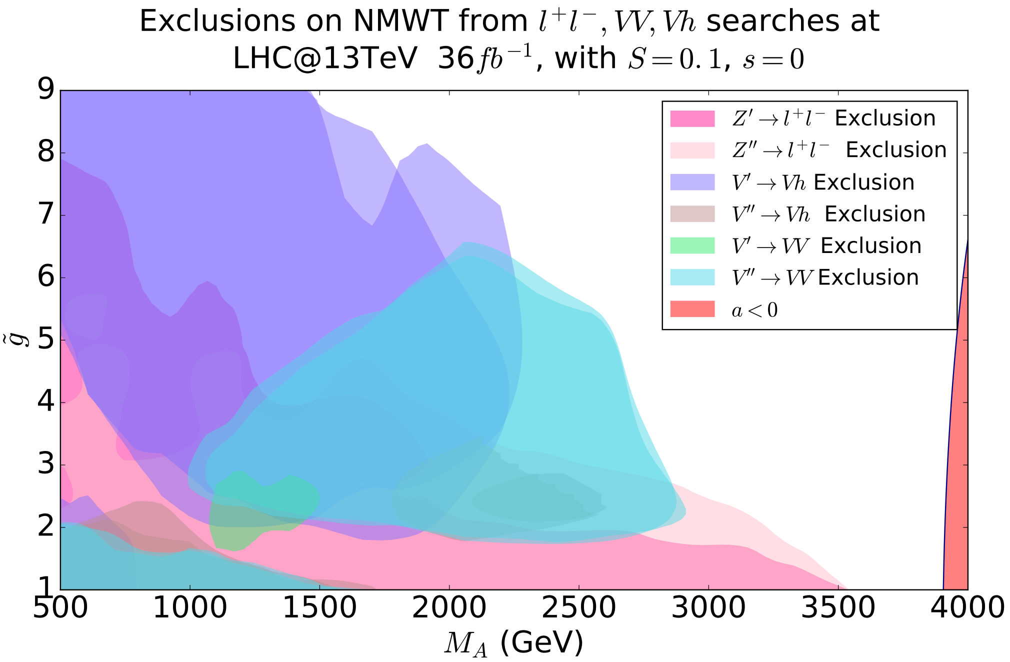

Figure 5.7: Combined exclusions on the $M_A, \tilde{g}$ parameter space from Drell-Yan $Z'/Z'' \to l^+l^-$, $V'(V'') \to Vh$, and $V'(V'') \to VV$ channels at $\sqrt{s} = 13\text{TeV}$ and $36fb^{-1}$ at benchmark values $S = 0.1$, $s = 0$, $\omega = 0$

remaining allowed points are 'always' allowed for all S, s, ω and cannot be excluded for a given LHC observed limit.

In Figure 5.8a we present the current status of LHC sensitivity in the dilepton channel, where the excluded points by the Z'' (dark grey) are layered on top of those excluded by the Z' (light grey). For this particular channel, there is minimal mixing due to the presence of no additional gauge particles and as such the ω parameter even at its largest does not affect the reach of the LHC dilepton limit. One can see that even this maximally conservative limit has the power to exclude up to $M_A \simeq 3.1\text{TeV}$ for low values of $\tilde{g}$. This limit on M_A is significantly (around 1TeV) higher than any previously limit, with the prior strongest limits set by the ATLAS collaboration[92, 89]. One should note that the previous limits from ATLAS which are set with $S = 0.3$, $s = 0$, $\omega = 0$ are actually the most optimistic limits for NMWT, as S as large as 0.3 is disfavoured by EWPD.

Figure 5.8b shows the most optimistic limits on NMWT from LHC@13TeV,

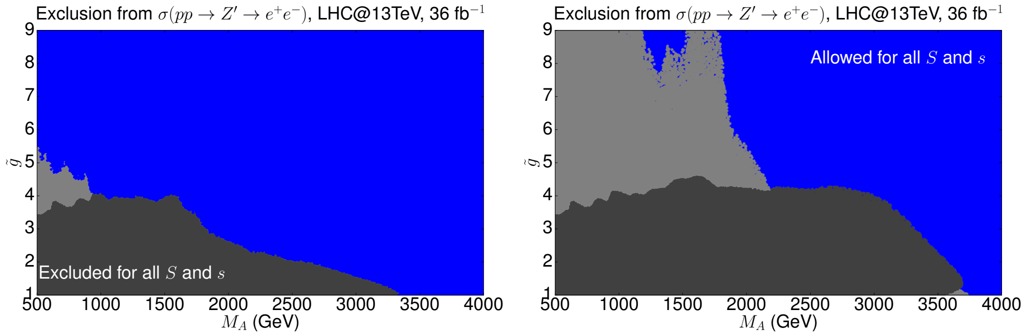

(a) (b)

Figure 5.8: Projections on $M_A, \tilde{g}$ parameter space of theoretical DY Z'/Z'' dilepton cross section showing the excluded for all S and s region (a), allowed for all S and s region (b) for the current CMS exclusion for LHC@13TeV and 36 fb^{-1} integrated luminosity. Blue points are allowed, light grey points are excluded by the Z', and dark grey points are excluded by the Z''.

$36 fb^{-1}$ dilepton searches. One can see that the most optimistic limits from DY dileptons follow the shape of the benchmark exclusion with $S = 0$, see Figure C.15b.

We repeat this process interpreting the limits on VV and Vh Drell-Yan resonances into the $M_A, \tilde{g}$ plane for both neutral and charged heavy resonances. Figure 5.9 shows the reach of the $Z'(Z'')Zh$ (a,b) and $W'(W'')Wh$ (c,d) limits. Neither the neutral or charged resonances in the Vh channel have the power to conclusively exclude regions of the $M_A, \tilde{g}$ plane for all S, s, ω, with only a very small region of low M_A and low $\tilde{g}$ excluded. For the neutral resonance, this is due to the S dependence of the axial/vector composition of the Z'/Z'', as when $S < 0$ the composition switches to a vector Z' and axial Z'' in the $M_A < M_{inv}$ regime. For the charged sector a similar switching occurs, but instead of axial and vector composition the switching is due to the mixing of the heavy resonances aligning to a mass ordering of $M_{W'} < M_{W''}$.

The optimistic reach of Vh limits (Figure 5.9(b,d)) is more promising, the neutral (charged) resonances can exclude all $\tilde{g}$ for $M_A \simeq 2$TeV(2.5TeV) for certain combinations of S, s and ω, again the main parameter controlling this is S. If EWPD can rule out negative S then the Vh processes can provide a powerful probe for the NMWT parameter space, so this result highlights the importance of EWPD in interpreting limits on Walking Technicolor.

Finally, Figure 5.10 shows the conservative and optimistic interpretations of LHC@13TeV VV limits on the NMWT parameter space for the $M_A, \tilde{g}$ projections. As with the Vh channel, the neutral and charged VV searches do not conclusively exclude any region of the M_A, $\tilde{g}$ regime. This is caused by the behaviour of the V'/V'' composition controlled by the S parameter analogously to the behaviour of the Vh 5D exclusion regions. The optimistic limits on NMWT for neutral and charged resonances, Figure 5.10(b,d) respectively, demonstrate the complementarity of the double resonance feature of NMWT as well as that of the charged and neutral searches in tandem. For certain combinations of S, s, ω, one can exclude a vast range of $M_A, \tilde{g}$ space, with the W' even providing a reach into the $M_A > M_{inv}$ regime which is untouched by the optimistic limits from other channels and resonances we have explored. Although the configuration for such complete covering of the M_A, $\tilde{g}$ plane relies heavily on the choice of S, s, ω, the regions that are 'always allowed' motivate us to combine LHC searches to fully explore the potential for discovery or total exclusion of Walking Technicolor theories.

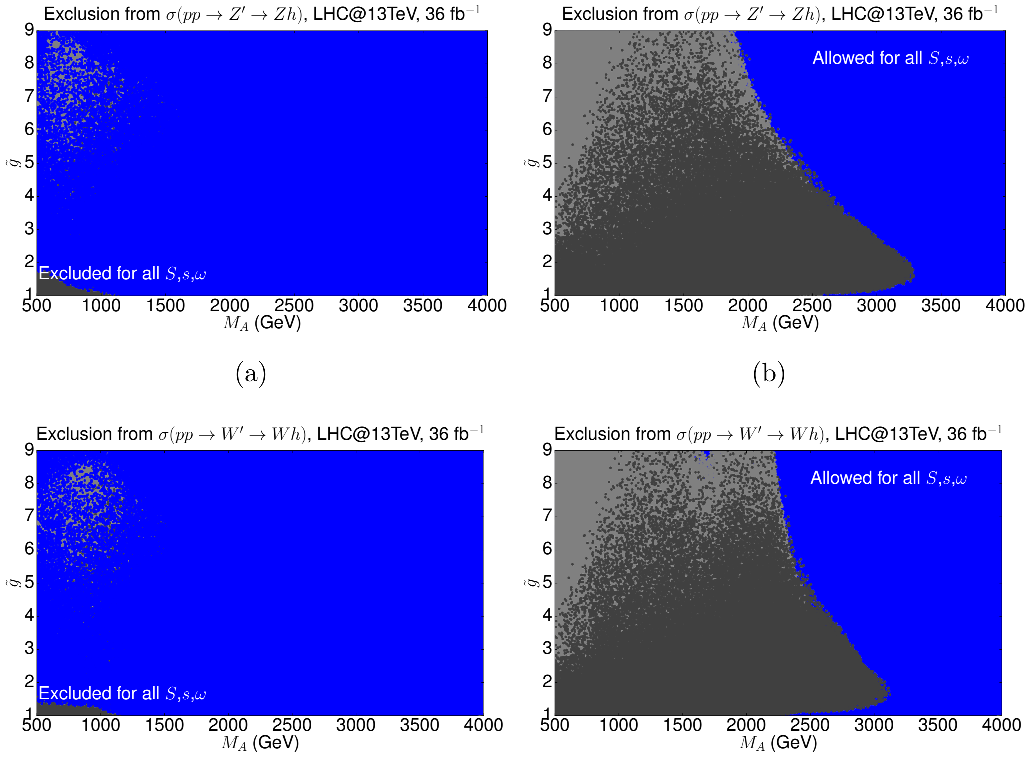

(a) (b)

(c) (d)

Figure 5.9: Projections on $M_A, \tilde{g}$ parameter space of theoretical $\sigma(pp \to Z'/Z'' \to Zh)$ showing the excluded for all S, s, ω region (a), allowed for all S, s, ω region (b) and theoretical $\sigma(pp \to W'/W'' \to Wh)$ showing the excluded for all S, s, ω region (c), allowed for all S, s, ω region (d) for the current ATLAS exclusion for LHC@13TeV and 36 fb^{-1} integrated luminosity. Blue points are allowed, light grey points are excluded by the $Z'(W')$, and dark grey points are excluded by the $Z''(W'')$.

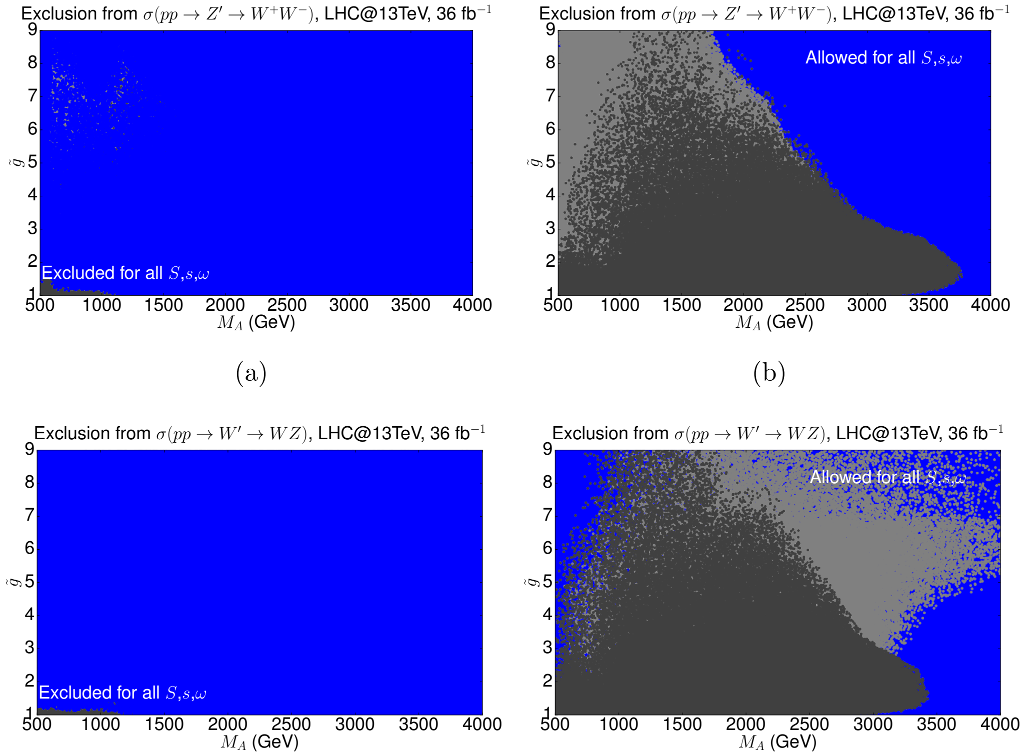

(a) (b)

(c) (d)

Figure 5.10: Projections on $M_A, \tilde{g}$ parameter space of theoretical $\sigma(pp \to Z'/Z'' \to W^+W^-)$ showing the excluded for all S, s, ω region (a), allowed for all S, s, ω region (b) and theoretical $\sigma(pp \to W'/W'' \to WZ)$ showing the excluded for all S, s, ω region (c), allowed for all S, s, ω region (d) for the current ATLAS exclusion for LHC@13TeV and 36 fb^{-1} integrated luminosity. Blue points are allowed, light grey points are excluded by the $Z'(W')$, and dark grey points are excluded by the $Z''(W'')$.

Chapter 6

NMWT Spectrum from Holography

6.1 Brief Introduction to Holography

Thus far we have studied Walking Technicolor from the perspective of its EW scale phenomenology, using a ‘bottom-up’ approach in which the Lagrangian describes the low energy behaviour of the model but does not know about the non-perturbative dynamics of the explicit Technicolour gauge dynamics. This is useful for exploring the model in the context of studies we can perform within the scope of modern particle colliders, however the method of scanning the parameter space of the low-energy theory does not provide insight from the underlying physics as to where one would naturally expect the realistic models to lie in the parameter space. Such predictions would require implementation of a ‘top-down’ approach, one in which the fundamental physics of the model would predict the low-energy physics, i.e where in the parameter space the models would be predicted to exist.

The difficulty that arises with top-down evaluations of Technicolor models is that the underlying dynamics are strongly coupled. The low-energy behaviour of weakly coupled NMWT interactions at Λ_{TC} is well defined, the phenomenological properties of the particles and their interactions can be safely calculated with perturbation theory. Strongly coupled theories such as QCD in which perturbation theory breaks down are considerably more complicated; one must look to tools in which properties of the strong dynamics can be approximated or simplified in some way. One such framework is that of Lattice Field Theory, in which space-time is discretised and calculations of QCD properties are performed on a grid (or lattice) of spacing a, such that in the limit of $a \to 0$ one recovers the continuous field theory[93]. This lattice spacing provides a UV cut-off at the scale $\Lambda_{UV} \sim \mathcal{O}(1/a)$, regularising the theory thus ensuring that the quantum field theory is finite. In principle, the Lattice Field Theory approach can be applied to any model exhibiting a non-perturbative strong dynamics, and in fact work has already begun from the lattice side on calculations within Walking Technicolor paradigms[94, 95, 96, 97, 98, 99, 100]. A major issue with lattice techniques is that they are computationally expensive even for QCD where properties such as N_c (number of colours) are well understood, so the situation quickly becomes a huge computational challenge. Lattice methods also struggle where there is a large separation in energy scales over which the coupling is strong, such as the characteristic running behaviour of Walking Technicolor theories. To explore such theories would require calculations across both long and short distance scales, which quickly becomes computationally challenging with separation of Λ_{TC} and Λ_{ETC} required for modern WTC models. A full exploration of possible WTC theories across the entire spectrum of possible N_c, N_f will take on the order of tens of years on the lattice, and even then a much larger portion of the lattice community would be required to provide the man-power and computing power needed for such an exploratory search.

The alternative for calculations within strong-coupling regimes is to exploit the AdS/CFT (Anti de Sitter/Conformal Field Theory) correspondence[101], where one can model the strongly interacting theory as living on the boundary of a weakly-interacting theory in one additional dimension. The extensive work of string theorists to provide an alternative description of Renormalisation Group (RG) flow has allowed us to glean insight on the properties of field theories with RG scale. Comprehensive literature on this construction can be found in [102, 103, 104, 105, 106], we focus here on the resulting demonstration of AdS/CFT correspondence and the idea behind the Holographic method[107].

The string theory construction of RG flow promotes a (3+1)-dimensional field theory to slices in a 5-dimensional bulk[108, 109], analogous to the description of information at the event horizon of a black hole. A pictorial view of this principle is given in Figure 6.1, where the field theory lives on planes in RG space.

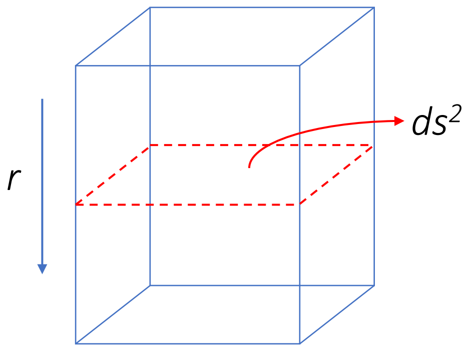

Figure 6.1: Visual analogy of RG space in which the (3+1)-dimensional field theory exists on planes in the bulk (4+1)-dimensional space, where RG scale r provides the additional length dimension.

The metric for the RG scale dependent field theory is

$$ds^2 = r^2 dx_{3+1}^2 + \frac{dr^2}{r^2}, \tag{6.1}$$

where r is the RG scale, i.e the radial direction in the 5-dimensional space (Figure 6.1). The metric must necessarily be invariant under scale transformations; for a scale transformation by a factor N the RG scale transforms as $r \to r/N$, i.e r scales as a mass ($m \to m/N$). One can clearly see then that this metric is invariant under scale transformations.

Let us inspect a scalar field ϕ in RG space, the Klein-Gordon equation for this scalar is simple to derive and is embedded in RG space via the action

$$S = \int d^4x \sqrt{-g}(\partial_\mu \phi \partial_\nu \phi g^{\mu\nu} + m^2 \phi^2), \tag{6.2}$$

where g is the determinant of the metric tensor

$$g_{\mu\nu} = \begin{pmatrix} -r^2 & 0 & 0 & 0 & 0 \\ 0 & r^2 & 0 & 0 & 0 \\ 0 & 0 & r^2 & 0 & 0 \\ 0 & 0 & 0 & r^2 & 0 \\ 0 & 0 & 0 & 0 & r^{-2} \end{pmatrix}. \tag{6.3}$$

Using this the Klein-Gordon equation for ϕ can now be recast in terms of r,

$$r^3(r^2(\partial_r\phi(r))^2 + m^2\phi^2), \tag{6.4}$$

where the factor of r^3 arises directly from the r dimensionality of $\sqrt{-g} = \sqrt{-det(g_{\mu\nu})}$. Applying the Euler-Lagrange equation, the equations of motion for this scalar field are

$$\partial_r(r^5\partial_r\phi) - r^3m^2\phi^2 = 0, \tag{6.5}$$

which has the solution

$$\phi = \frac{A}{r^\Delta}, \tag{6.6}$$

where the dimensionful exponent Δ is related to the bulk mass as

$$m^2 = \Delta(\Delta - 4). \tag{6.7}$$

Noting that the scalar field has no mass-dimension, the coefficient A must carry a mass-dimension of Δ, in fact this coefficient can be directly identified with the expectation value of operators of the (3+1)-dimensional field theory. This is a clear demonstration of the correspondence between the bulk mass in 5-dimensions with the (3+1)-dimensional field theory operators, and this result is the foundation of Holography.

Consider a strongly interacting field theory embedded in the 5D space described above, one can study the vacuum of the theory via the quark condensate $\langle\bar{q}q\rangle$. In the UV, the mass dimension of the quark condensate is 3, so from equation 6.7 the bulk mass-squared $m^2 = -3$. If we wish to study the properties of the condensate as it runs with RG scale, we can introduce a mass for the scalar particle, $\Delta m^2(r) \neq 0$, which runs with RG scale[1]. The running mass-squared now allows us insight into the running of $\langle\bar{q}q\rangle$, effectively introducing a running anomalous dimension, γ, for the quark condensate. Thus, one can perform perturbative calculations in the 5D bulk theory which inform us of the properties of the strongly interacting (3+1)-dimensional field theory.

---

[1] Note here that $\Delta m^2 = 0$ recovers the UV solution for the scalar mass

Holography provides a rigorous method of calculation for strongly interacting gauge theories that are close to a $\mathcal{N} = 4$ supersymmetric gauge theory[110, 111, 112, 113]. The advantage of using such an approach to glean information about strongly interacting theories is that it is much less computationally expensive, in fact one can already employ the holographic method to calculate top-down predictions for theories with new strong interactions.

Throughout this chapter, I will detail the work carried out in collaboration with holography experts Prof Nick Evans and Dr Marc Scott[5]. I will describe their holographic method in section 6.2 as detailed in this paper. The remainder of this chapter will detail our collaborative efforts to predict the full spectrum of WTC theories and deduce where these theories lie in the NMWT parameter space.

6.2 Holographic Model

Using the model of AdS/QCD one can calculate phenomenological properties of QCD such as masses and couplings of π, ρ, a mesons etc. from a holographic perspective[114, 115], where the simplest model inputs the dynamics of the techni-quark condensate $< \bar{q}q >$ by hand. To apply this to generic strongly coupled gauge theories one must extend the holographic model to include the dynamics of said gauge theory. The caveat is that one must still input an assumed form for the running of the anomalous dimension, γ, of $< \bar{q}q >$. Details of this Dynamic AdS/QCD model are given in [116, 117], here we present a summary of the key components of this model. One can validate the holographic model for the well established QCD spectrum (in which $N_c = N_f = 3$), where the resulting predictions are within 10% of the experimental values. Our philosophy here is to hope that this will hold true for WTC models, giving sensible predictions for at least some values of N_c, N_f. For those that, understandably, doubt the reliability of these predictions, we offer that the predicted spectra calculated using the top-down holographic method give a rough guide as to where the physical theories exist in the parameter space.

Let us make some qualitative statements regarding the physical spectrum of WTC models in the AdS/QCD context. The spectrum of physical particles looks QCD-like in that there exist heavy mesons akin to the QCD σ, ρ and A, which we can identify as the composite Higgs, Z', and Z'' of the phenomenological NMWT model respectively. Generic scaled up QCD running coupling will generate a large S and heavy σ, however the holographic model can produce a sufficiently light σ (Higgs) if one modifies the running to be near-conformal at the symmetry breaking scale. The tuning of the holographic model to small S corresponds to tuning the mass splitting of ρ and A mesons to near-degeneracy. We predict the heavy meson spectrum for a range of N_c, N_f, with the hope that at least one of them will produce the correct walking dynamics to correspond to a physical WTC theory. Although the exact spectrum will be wrong for many, if not most, of these N_c, N_f choices, we present all spectra in the parameter space to give Technicolor the best chance of survival as well as providing a guide for potentially total exclusion of the Walking Technicolor paradigm.

The action of the Dynamic AdS/QCD model is

$$S = -\int d^4x du \mathrm{Tr} u^3 \left[\frac{1}{r^2}|DX|^2 + \frac{\Delta m^2(r)}{u^2}|X|^2 + \frac{1}{2\kappa^2}(F_V^2 + F_A^2) \right], \tag{6.8}$$

where u is the holographic co-ordinate dual to the energy scale, X is a field dual to the quark condensate $\bar{q}q$, κ is a tunable parameter that controls the $V - A$ mass splitting, $\Delta m^2(r)$ is an RG scale mass term. In the models of interest here Δm^2 is fixed from the running of the gauge coupling at two-loop level, which also encapsulates the existence of IR fixed points in the running for certain N_c, N_f. The vacuum of the theory is described by the solution of the equations of motion for the quark condensate (see equation 6.5).

We choose the on-mass-shell condition $|X|(u = X_0) = X_0$ with $|X|'(X_0) = 0$. We require $|X| = 0$ in the UV to ensure that the techniquarks are massless. Fluctuations of the field dual X correspond to the σ and π fields. The vector and axial fields are described by the operators $\bar{q}\gamma^\mu q$ and $\bar{q}\gamma^\mu\gamma_5 q$ respectively, where their fluctuations describe the spectrum and couplings of the ρ and A respectively. Studying these vector and axial operators from a Holographic perspective is equivalent to studying a gauge field V_μ (A_μ for the axial field) living in the 5D space depicted in Figure 6.1.

Following from the derivation in section 6.1, the theory exists in the 5-dimensional metric

$$ds^2 = r^2 dx_{3+1}^2 + \frac{1}{r^2}du^2, \tag{6.9}$$

where we now define the radial co-ordinate r as

$$r^2 = u^2 + |\mathrm{Tr}X|^2. \tag{6.10}$$

The trace term in the radial co-ordinate represents a 'back-reaction' on the metric in the spirit of probe brane models [110, 111, 112, 113], as well as communicating the mass gap to the meson spectrum.

To calculate the spectrum of the theory, one must look at linearised fluctuations of the fields around the vacuum, where fields generically take the form $f(u)\exp^{ip.x}$ with $p^2 = -M^2$. One can also determine the decay constants for the scalar, vector, and axial mesons by substituting their respective wave functions back into the action S and integrating over u. Normalisation of these fluctuations can be achieved by matching to the expected scalar-scalar, vector-vector, and axial-axial correlators from the gauge theory in the UV[2].

The initial focus of these models is the case of a single EW doublet of techniquarks and one technicolor singlet as in the NMWT model, where the singlet is decoupled from the theory at the TC scale but can change the running of the coupling in the UV. Models with increased numbers of doublets and singlets will then be explored and their spectra calculated. For all models, we tune the running of the anomalous dimension γ in the IR such that the σ meson is generated at $m_\sigma = 125$GeV. To achieve this tuning we set a value of α_{TC} at the scale at which we deviate from the running regime of the UV theory. Below this scale, we allow N_f to be a free parameter and choose N_f^{IR} in such a way as to allow the σ meson mass to be tuned to the observed Higgs mass. One should note here that N_f^{IR} is not the true value of N_f in the theory, and in fact is $N_f^{IR} \simeq 11.43$ for all cases. Physically, this matching scale appears as a discontinuity in the running of α_{TC}, which is dealt with by performing the calculations in the two different sections (below and above the discontinuity) and matching the fields and their derivatives at this point. The matching point itself is varied between $0.3 \leq \alpha_{TC} \leq 0.7$, to give some idea of the error in the predictions of the spectrum.

In Figure 6.2 we show the running of α_{TC} for the various N_f values we explore in the case of WTC with $N_c = 3$, along with a QCD-like running for comparison. One can see that the IR running is essentially the same for all of these theories due to the tuning to the Higgs mass, which has implications we will discuss in section 6.4.

Along with the tuning to the Higgs mass, we tune the coupling κ such that the $\rho - A$ ($Z' - Z''$ in NMWT) degeneracy is sufficiently small to produce S consistent with EWPD. As is the generally identified benchmark presented in

---

[2] Note that the holographic literature expresses the dim-2 coupling of the vector meson and its source is written as F_V^2, as opposed to the WSR literature where it is written as $M_V F_V$. We follow the latter here for consistency within this thesis.

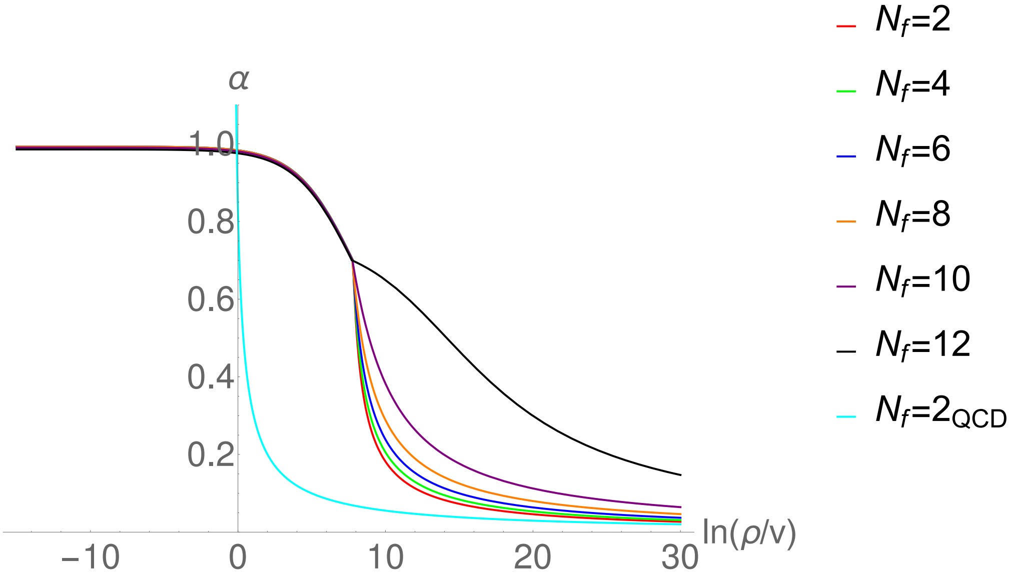

Figure 6.2: The running of α_{TC} against RG scale imposed on the holographic model with $N_c = 3$. The curve furthest to the left is for a technicolor model that is a scaled up version of QCD with the usual two loop result for the running. The next curve over is that same theory forced to have a IR fixed point to produce a light higgs (clearly we know for this theory that this assumption is wrong!). Moving further to the right we see the running as further singlet techi-quarks are added, again with N_f^{IR} chosen to give a light higgs. The IR of all such theories is shared and uniquely determined by needing the observed higgs mass.

the phenomenology of the bottom-up model (chapter 4), we choose $S = 0.1$. For most N_c, N_f theories this is almost certainly not the case and the mass splitting would be greater, however again we are invoking our philosophy of generosity towards giving WTC theories the best chance of survival. Excluding even these extremely favourable models would mean conclusive exclusion of the whole WTC paradigm. One should note that in the case of $\kappa = 0$, the Lagrangian terms for the ρ and A mesons are indistinguishable and their masses exactly degenerate. However, the first term in the action (equation 6.8) links the A meson and the symmetry breaking field X and is suppressed, and so in order to maintain the correct F_π one must raise the overall scale of the A meson.

Let us now summarise the holographic model and indicate the properties it predicts. For a theory with N_c, N_f the UV running of the coupling (and subsequently the anomalous dimension γ) is fixed at 2-loop order in perturbation theory. The overall scale is set by $F_\pi = 246\text{GeV}$ (as in the NMWT phenomenological model, equation 2.24). The IR running is modified by adjusting the effective N_f^{IR} such that the σ mass is fixed to the Higgs mass. This IR modification occurs below the matching scale α_{TC}, which is varied from 0.3 to 0.7 to approximate an error in the predicted spectrum. With all this implemented, the holographic model then predicts the spectrum in terms of M_ρ, F_ρ, M_A, F_A, which are functions of the 5D gauge coupling κ. Tuning κ to fix $S = 0.1$ removes one degree of freedom, and we can rephrase the remaining predictions as

$$M_A, \quad \tilde{g} = \frac{\sqrt{2}M_V}{F_V}, \quad \omega = \frac{1}{2}\left(\frac{F_\pi^2 + F_A^2}{F_V^2} - 1\right), \tag{6.11}$$

in order to interpret them into the NMWT parameter space. One should note here that for all of the models explored using this method we find $\omega < 0.05$. This is sufficiently low as to provide no meaningful alteration to the reach of experimental limits on the NMWT parameter space, so results presented in section 6.4 suppress this factor and can be essentially considered ω independent.

6.3 NMWT Set-up for $N_D > 1$

The phenomenological model thus far discussed is the NMWT model with $N_c = 3$ and $N_f = 2$, however one may wish to explore the phenomenology of the varying N_f and N_c Walking Technicolor models explored in the holographic method. The implementation of these models into CalcHEP is beyond the scope of this thesis, however here we detail the changes to the effective low-energy WTC model in the case of additional techni-quark doublets and singlets. We discuss the effect on the physical spectrum from symmetry breaking in the case of additional doublets and additional singlets, and the modification to the effective Lagrangian and mixing matrices for the example case of $N_D = 2$ doublets of techni-quarks.

6.3.1 WTC with Additional Doublets

Generalising the chiral symmetry of the NMWT model presented in section 2.1, the chiral symmetry $SU(N_f)_L \otimes SU(N_f)_R$ is dynamically breaks to $SU(N_f)_V$. As the additional techniquarks are doublets under the $SU(N_f)$

group the number of doublets is $N_D = 2N_f$. The generalised symmetry breaking pattern is

$$(2\oplus 2\oplus 2\oplus\dots)_L\times(2\oplus 2\oplus 2\oplus\dots)_R \to N_D^2(3)_V+(N_D^2-1)(1)_V+(1')_V, \tag{6.12}$$

which reproduces the pattern of equation 2.6 in the $N_D = 1$ case. The consequence of this is that in the broken phase there are now N_D^2 triplets of vector and axial mesons, i.e N_D^2 (Z', W') and N_D^2 (Z'', W'') mesons in the gauge sector. Note that there are also $N_D^2 - 1$ singlets (plus the lone $(1')_V$ singlet) which arise from symmetry breaking, however these are decoupled from the theory at the scale Λ_{TC} so they have no effect on the LHC phenomenology.

In terms of the gauge sector Lagrangian, the new gauge fields contribute in the same way as the A_L and A_R fields in equation 2.5. For N_D techni-quark doublets the low-energy Lagrangian is then

$$\begin{aligned}
\mathcal{L}_{boson} =& -\frac{1}{2}\mathrm{Tr}\big[\tilde{W}_{\mu\nu}\tilde{W}^{\mu\nu}\big] - \frac{1}{4}\tilde{B}_{\mu\nu}\tilde{B}^{\mu\nu} - \frac{1}{2}\sum_{i=1}^{N_D}\mathrm{Tr}[F^i_{L\mu\nu}F_L^{i,\mu\nu}+F^i_{R\mu\nu}F_R^{i,\mu\nu}] \\
&+ m^2\sum_{i=1}^{N_D}\mathrm{Tr}[(C^i_{L\mu})^2+(C^i_{R\mu})^2] + \frac{1}{2}\mathrm{Tr}[D_\mu M D^\mu M^\dagger] - \tilde{g}^2 r_2\sum_{i=1}^{N_D}\mathrm{Tr}[C^i_{L\mu}MC_R^{i,\mu}M^\dagger] \\
&- \frac{i\tilde{g}r_3}{4}\sum_{i=1}^{N_D}\mathrm{Tr}[C^i_{L\mu}(MD^\mu M^\dagger - D^\mu MM^\dagger) + C^i_{R\mu}(M^\dagger D^\mu M - D^\mu M^\dagger M)] \\
&+ \frac{\tilde{g}^2 s}{4}\sum_{i=1}^{N_D}\mathrm{Tr}[(C^i_{L\mu})^2 + (C^i_{R\mu})^2]\mathrm{Tr}[MM^\dagger] + \frac{\mu^2}{2}\mathrm{Tr}[MM^\dagger] - \frac{\lambda}{4}\mathrm{Tr}[MM^\dagger]^2,
\end{aligned} \tag{6.13}$$

Let us inspect the gauge mixing sector in the case of $N_D = 2$. There are then 4 copies of the $\rho(A)$ sector which can all mix with the electroweak gauge bosons. This means that the charged sector will have a 9×9 gauge mixing matrix, and the neutral sector a 10×10 gauge mixing matrix. Before rotation into the mass basis, we can write mixing matrices for the neutral and charged bosons in terms of the Lagrangian parameters $g_1, g_2, \tilde{g}, f, v, r_2$ and r_3, where f is the TC vev as defined in equation 2.36. The gauge mixing Lagrangian is

$$\mathcal{L}_{mass} = \begin{pmatrix} \tilde{B}_\mu & \tilde{W}_\mu & A^1_{L\mu} & A^1_{R\mu} & A^2_{L\mu} & A^2_{R\mu} & A^3_{L\mu} & A^3_{R\mu} & A^4_{L\mu} & A^4_{R\mu} \end{pmatrix} \mathcal{M}^2_N \begin{pmatrix} \tilde{B}^\mu \\ \tilde{W}^\mu \\ A^{1\mu}_L \\ A^{1\mu}_R \\ A^{2\mu}_L \\ A^{2\mu}_R \\ A^{3\mu}_L \\ A^{3\mu}_R \\ A^{4\mu}_L \\ A^{4\mu}_R \end{pmatrix}$$

$$+ \begin{pmatrix} \tilde{W}^-_\mu & A^{1-}_{L\mu} & A^{1-}_{R\mu} & A^{2-}_{L\mu} & A^{2-}_{R\mu} & A^{3-}_{L\mu} & A^{3-}_{R\mu} & A^{4-}_{L\mu} & A^{4-}_{R\mu} \end{pmatrix} \mathcal{M}^2_C \begin{pmatrix} \tilde{W}^{+\mu} \\ A^{+1\mu}_L \\ A^{+1\mu}_R \\ A^{+2\mu}_L \\ A^{+2\mu}_R \\ A^{+3\mu}_L \\ A^{+3\mu}_R \\ A^{+4\mu}_L \\ A^{+4\mu}_R \end{pmatrix} .$$

The mixing matrices $\mathcal{M}^2_N$ and $\mathcal{M}^2_C$ are

$$\mathcal{M}_N^2=\begin{pmatrix}
\frac{g_1^2}{4}(f^2+av^2) & -\frac{g_1g_2}{4}bv^2 & \frac{g_1\tilde{g}}{4\sqrt{2}}(f^2+cv^2) & -\frac{g_1\tilde{g}}{4\sqrt{2}}(f^2+dv^2) & \frac{g_1\tilde{g}}{4\sqrt{2}}(f^2+cv^2) & -\frac{g_1\tilde{g}}{4\sqrt{2}}(f^2+dv^2) & \frac{g_1\tilde{g}}{4\sqrt{2}}(f^2+cv^2) & -\frac{g_1\tilde{g}}{4\sqrt{2}}(f^2+dv^2) & \frac{g_1\tilde{g}}{4\sqrt{2}}(f^2+cv^2) & -\frac{g_1\tilde{g}}{4\sqrt{2}}(f^2+dv^2) \\
-\frac{g_1g_2}{4}bv^2 & \frac{g_2^2}{4}(f^2+av^2) & -\frac{g_2\tilde{g}}{4\sqrt{2}}(f^2+cv^2) & -\frac{g_2\tilde{g}}{4\sqrt{2}}(f^2+dv^2) & -\frac{g_2\tilde{g}}{4\sqrt{2}}(f^2+cv^2) & -\frac{g_2\tilde{g}}{4\sqrt{2}}(f^2+dv^2) & -\frac{g_2\tilde{g}}{4\sqrt{2}}(f^2+cv^2) & -\frac{g_2\tilde{g}}{4\sqrt{2}}(f^2+dv^2) & -\frac{g_2\tilde{g}}{4\sqrt{2}}(f^2+cv^2) & -\frac{g_2\tilde{g}}{4\sqrt{2}}(f^2+dv^2) \\
\frac{g_1\tilde{g}}{4\sqrt{2}}(f^2+cv^2) & -\frac{g_2\tilde{g}}{4\sqrt{2}}(f^2+cv^2) & \frac{\tilde{g}^2}{4}(f^2-dv^2) & 0 & 0 & 0 & 0 & 0 & 0 & 0 \\
-\frac{g_1\tilde{g}}{4\sqrt{2}}(f^2+dv^2) & -\frac{g_2\tilde{g}}{4\sqrt{2}}(f^2+dv^2) & 0 & \frac{\tilde{g}^2}{4}(f^2+dv^2) & 0 & 0 & 0 & 0 & 0 & 0 \\
\frac{g_1\tilde{g}}{4\sqrt{2}}(f^2+cv^2) & -\frac{g_2\tilde{g}}{4\sqrt{2}}(f^2+cv^2) & 0 & 0 & \frac{\tilde{g}^2}{4}(f^2-dv^2) & 0 & 0 & 0 & 0 & 0 \\
-\frac{g_1\tilde{g}}{4\sqrt{2}}(f^2+dv^2) & -\frac{g_2\tilde{g}}{4\sqrt{2}}(f^2+dv^2) & 0 & 0 & 0 & \frac{\tilde{g}^2}{4}(f^2+dv^2) & 0 & 0 & 0 & 0 \\
\frac{g_1\tilde{g}}{4\sqrt{2}}(f^2+cv^2) & -\frac{g_2\tilde{g}}{4\sqrt{2}}(f^2+cv^2) & 0 & 0 & 0 & 0 & \frac{\tilde{g}^2}{4}(f^2-dv^2) & 0 & 0 & 0 \\
-\frac{g_1\tilde{g}}{4\sqrt{2}}(f^2+dv^2) & -\frac{g_2\tilde{g}}{4\sqrt{2}}(f^2+dv^2) & 0 & 0 & 0 & 0 & 0 & \frac{\tilde{g}^2}{4}(f^2+dv^2) & 0 & 0 \\
\frac{g_1\tilde{g}}{4\sqrt{2}}(f^2+cv^2) & -\frac{g_2\tilde{g}}{4\sqrt{2}}(f^2+cv^2) & 0 & 0 & 0 & 0 & 0 & 0 & \frac{\tilde{g}^2}{4}(f^2-dv^2) & 0 \\
-\frac{g_1\tilde{g}}{4\sqrt{2}}(f^2+dv^2) & -\frac{g_2\tilde{g}}{4\sqrt{2}}(f^2+dv^2) & 0 & 0 & 0 & 0 & 0 & 0 & 0 & \frac{\tilde{g}^2}{4}(f^2+dv^2)
\end{pmatrix}, \tag{6.14}$$

$$\mathcal{M}_C^2=\begin{pmatrix}
\frac{g_2^2}{4}(f^2+av^2) & -\frac{g_2\tilde{g}}{4\sqrt{2}}(f^2+cv^2) & -\frac{g_2\tilde{g}}{4\sqrt{2}}(f^2+dv^2) & -\frac{g_2\tilde{g}}{4\sqrt{2}}(f^2+cv^2) & -\frac{g_2\tilde{g}}{4\sqrt{2}}(f^2+dv^2) & -\frac{g_2\tilde{g}}{4\sqrt{2}}(f^2+cv^2) & -\frac{g_2\tilde{g}}{4\sqrt{2}}(f^2+dv^2) & -\frac{g_2\tilde{g}}{4\sqrt{2}}(f^2+cv^2) & -\frac{g_2\tilde{g}}{4\sqrt{2}}(f^2+dv^2) \\
-\frac{g_2\tilde{g}}{4\sqrt{2}}(f^2+cv^2) & \frac{\tilde{g}^2}{4}(f^2-dv^2) & 0 & 0 & 0 & 0 & 0 & 0 & 0 \\
-\frac{g_2\tilde{g}}{4\sqrt{2}}(f^2+dv^2) & 0 & \frac{\tilde{g}^2}{4}(f^2+dv^2) & 0 & 0 & 0 & 0 & 0 & 0 \\
-\frac{g_2\tilde{g}}{4\sqrt{2}}(f^2+cv^2) & 0 & 0 & \frac{\tilde{g}^2}{4}(f^2-dv^2) & 0 & 0 & 0 & 0 & 0 \\
-\frac{g_2\tilde{g}}{4\sqrt{2}}(f^2+dv^2) & 0 & 0 & 0 & \frac{\tilde{g}^2}{4}(f^2+dv^2) & 0 & 0 & 0 & 0 \\
-\frac{g_2\tilde{g}}{4\sqrt{2}}(f^2+cv^2) & 0 & 0 & 0 & 0 & \frac{\tilde{g}^2}{4}(f^2-dv^2) & 0 & 0 & 0 \\
-\frac{g_2\tilde{g}}{4\sqrt{2}}(f^2+dv^2) & 0 & 0 & 0 & 0 & 0 & \frac{\tilde{g}^2}{4}(f^2+dv^2) & 0 & 0 \\
-\frac{g_2\tilde{g}}{4\sqrt{2}}(f^2+cv^2) & 0 & 0 & 0 & 0 & 0 & 0 & \frac{\tilde{g}^2}{4}(f^2-dv^2) & 0 \\
-\frac{g_2\tilde{g}}{4\sqrt{2}}(f^2+dv^2) & 0 & 0 & 0 & 0 & 0 & 0 & 0 & \frac{\tilde{g}^2}{4}(f^2+dv^2)
\end{pmatrix}, \tag{6.15}$$

where $a = (1-r_3)$, $b = (1+r_2-r_3)$, $c = (r_2-r_3)$ and $d = -r_2$.

One can see that diagonalisation of the gauge sector very quickly becomes a lengthy and difficult analytic calculation, and practical construction of phenomenological WTC models with $N_D > 1$ may be undesirable. Nevertheless, we can infer some consequences of the additional doublets; firstly the techni-pion decay constant F_π will be increased by the contribution of the additional vector and axial fields, so to counteract this the mass scale of the model, M_A, should decrease. Secondly, we expect that vertices with TC-EW interactions will be diluted by the presence of the additional gauge mesons, as the coupling structure of such vertices will be modified by the contribution from N/C_{1j} elements where $4 < j \leq N_f$. We will discuss the consequences of additional doublets in the context of the holographic predictions of the spectra in section 6.4.

6.3.2 WTC with Additional Singlets

The holographic calculation was also performed with a single techni-quark doublet with an increasing number of singlets, which requires an alternative approach to building a WTC model. The unbroken phase then consists of a single doublet of techni-quarks (so fixing $N_D = 1$) and $N_f - 2$ techni-quarks singlets. The symmetry breaking pattern of the $SU(N_f)_L \otimes SU(N_f)_R$

$$(2 \oplus 1 \oplus 1 \oplus \dots)_L \times (2 \oplus 1 \oplus 1 \oplus \dots)_R \to (3)_V + 2(N_D - 2)(2)_V + (N_f - 2)^2(1)_V, \tag{6.16}$$

along with the axial-vector copy of this physical spectrum.

This is distinctly different to the breaking pattern in equation 6.12 as there is now only a single $\rho(A)$ sector, with $2(N_f - 2)$ vector doublets arising out of the symmetry breaking instead. Again there are gauge singlets (although now there are $(N_f - 2)^2$ of them) which are considered decoupled from the theory at the scale Λ_{TC}. This could offer an interesting and unique WTC phenomenology with an extended gauge doublet sector, though the phenomenology of such models from the bottom-up perspective is yet to be explored.

As a prelude to the eventual building of such models (should anyone wish to take up this mantle), one can begin by understanding the structure of interactions in the unbroken phase of the model. Let us consider the case of

$N_f = 4$, before symmetry breaking the WTC gauge sector consists of

$$\begin{pmatrix} U \\ D \end{pmatrix}, \quad n_1, \quad n_2, \tag{6.17}$$

where n_1 and n_2 are techni-quark singlets.

The Lagrangian for techni-quark mixing in the unbroken phase is

$$\mathcal{L}_{mixing} = \begin{pmatrix} U & D & n_1 & n_2 \end{pmatrix} \mathcal{M}^2 \begin{pmatrix} U \\ D \\ n_1 \\ n_2 \end{pmatrix}, \tag{6.18}$$

where

$$\mathcal{M}^2 = \begin{pmatrix} \sigma^i & m_1 \\ m_2 & 0 \end{pmatrix}. \tag{6.19}$$

Each of the elements in $\mathcal{M}$ is a 2×2 matrix, split up into 4 sectors defining the allowed mixing of the doublet and singlets. The σ^i are the usual Pauli matrices, m_1, m_2 are (as yet unspecified) non-zero matrices. This means that the doublet techni-quarks U and D can interact mix (i.e form bound states) with any of the other techni-quarks where their interactions are defined by the σ^i, m_1, m_2 quadrants of $\mathcal{M}$. However, there is no mixing purely between techni-quark singlets n_1 and n_2. For this case, under symmetry breaking we then have 3 states from the upper-left mixing sector which combine to form one gauge meson triplet, and 8 states from the off-diagonal mixing sectors which combine to form 4 doublets. The remaining degrees of freedom are taken up by non-interacting singlets generated by the symmetry breaking. This matches the expected spectrum in equation 6.16 for $N_f = 4$.

6.4 NMWT Spectrum from Holography

As detailed in our paper [5], Figure 6.3 presents the holographic predictions of the WTC spectrum for varying N_c, N_f projected into the usual $M_A, \tilde{g}$ parameter space, along with the exclusion region from DY dileptons at the LHC@13TeV, $36 fb^{-1}$. The limit setting procedure and results for dileptons are presented in chapter 5.2. The holographic spectra are presented for WTC models with a global $SU(N_c)$ symmetry where $N_c = 3, 4, 5$. For each N_c, the models with a single doublet and additional techni-quark singlets are calculated for $N_f = 2, 4, 6, 8, 10, 12$ (all), $N_f = 14$ (for $N_c = 4, 5$) and $N_f = 16$ (for $N_c = 5$). Models with additional doublets of techni-quarks are calculated for $N_D = 1, 2, 3, 4, 5, 6$ doublets (all N_c), $N_D = 7$ (for $N_c = 4, 5$), and $N_D = 8$ (for $N_c = 5$). These N_D values are chosen such that $N_D < 2N_c$, as this is where the theories are assumed to enter the conformal window.

To understand the interpretation of holographic spectra in the WTC parameter space, let us first discuss the spectrum of a QCD-like Technicolor model as predicted by holography. The model itself is simply a scaled up QCD; the model has a running coupling and is built of an $SU(3)$ gauge group with $N_f = 2$, and the pion decay constant is scaled from the QCD $f_\pi = 93$MeV to the usual techni-pion decay constant $F_\pi = 246$GeV. Running such a model through the holographic calculation, the spectrum is predicted to be $M_\rho = 2.05$TeV, $M_A = 3.25$TeV, $S = 0.3$ and $\tilde{g} = 7$. Of course, one should note that the absence of a light Higgs excludes this model, and in any case the $S = 0.3$ is disfavoured by EWPD (outright excluded for $T = 0$). It is interesting to note however that due to the large M_A and $\tilde{g}$, this model is not excluded by the Z'/Z'' dilepton limit. With this in mind, let us explore the position of the Walking models in the WTC theory space and the implications for the models.

As discussed in section 6.2, one can somewhat choose the value of α_{TC} at which the coupling begins to slowly run to a conformal fixed point, here the cases of $\alpha_{TC} = 0.3$ and $\alpha_{TC} = 0.7$ as the extremities of the valid range. The most minimal model of WTC is the one with a QCD-like gauge group, i.e $N_c = 3$ and $N_f = 2$, but with deformed running in the IR (see Figure 6.2). As an example, if the IR running kicks in at $\alpha_{TC} = 0.7$, the predicted spectrum for this minimal model lies at $M_A = 4.11$TeV, $\tilde{g} = 8.49$ (along with $\omega = 0.047$, although as previously discussed this parameter is negligible), where we have tuned κ such that $S = 0.1$. This model appears in Figure 6.3 as the uppermost red point. The main observation here is that the deformation of the running coupling of a QCD-like model to produce a light Higgs pushes the model spectrum higher in both M_A and $\tilde{g}$, so moving away from the dilepton limits. This is due to the modification of the running, as from Figure 6.2 one can see that these models have a strong coupling α out to much higher energy scales than the scaled-up QCD running.

For each $SU(N_c)$ gauge group, WTC models with additional EW singlets are shown as points in Figure 6.3. The effect of the additional singlets is to move the position of the model spectrum lower in M_A, with no meaningful alteration in $\tilde{g}$ ($< 1\%$ level). These models all have very similar spectra, owing to the additional singlets only affecting the UV running. The IR running of all additional singlet models is very similar, as such the physical techni-meson spectrum feels only a very small effect necessitated by the tuning to M_h.

The WTC models with additional techni-quark doublets are represented in Figure 6.3 by the lined boxes, the width of which represent the error corresponding to the lower and upper values of the matching scale α_{TC}. The lines at the top of the spectrum along which the singlet models lie are those models where $N_D = N_f/2 = 1$. The effect of additional doublets on the mass scale M_A is somewhat intricate - on the surface the additional doublets increases F_π by $\sqrt{N_f}$ hence reducing M_A. However, the S parameter naturally grows with N_f, so to maintain $S = 0.1$ one has to tune κ and consequently increase the mass scale of the theory. These two effects combine to slightly reduce M_A, with an overall difference in M_A between minimal to maximal N_D models at $\Delta M_A < 0.5$TeV. The effect on the gauge coupling $\tilde{g}$ is much more pronounced, as the axial decay constant F_A also scales as $\sqrt{N_f}$ causing $\tilde{g}$ to decrease as N_D increases.

A notable feature amongst the holographic predictions is that all models lie on or around the line at which the phenomenological parameter a (see equation 2.34), associated with the 2nd WSR, is $a = 0$. This is caused by the relationship between the a parameter and the degeneracy of ρ, A (or Z', Z'' in the phenomenological model), as similarly to S this a parameter naturally grows with increasing $\rho - A$ degeneracy. By forcing S to be small one subsequently causes a towards zero, as the tuning of κ physically corresponds to a complicated tuning of the vector/axial masses and decay constants to achieve $S = 0.1$. Although it is unclear whether these tunings are realistic or even achievable in a UV complete model, we cite our philosophy of allowing predictions even for unrealistic WTC models.

One can clearly see from Figure 6.3 that the current reach of dilepton searches at the LHC is insufficient to rule out any of the holographic models. Comparing to the VV/Vh limits in Figure 5.6, even the addition of these alternative channels does not probe the parameter space occupied by the holographic models. The models closest to the current exclusions are those of maximal N_D for a given N_c, with the $SU(5)$, $N_D = 8$ model offering the most likely chance of exclusion from future results as comparatively to prior results, the Z'/Z'' dilepton limits have increased in M_A for low $\tilde{g}$.

Along with the dilepton limit, we also present a signal-to-background ratio characteristic of this channel at which $S/B = 1\%$, at which point the systematic uncertainty of the detector would saturate any potential signal. This is represented by a dashed line in Figure 6.3, above which the dilepton channel would no longer be effective for these neutral resonance searches. The S/B is a useful tool to explore the maximal potential reach of experimental searches, as the ratio is expected to stay the same for a given channel regardless of collider energy/luminosity. The limit for dileptons of $S/B > 1\%$ arises from the extent to which one can reduce the statistical uncertainty in measuring the dilepton background. This statistical uncertainty reaches a minimum when it reaches the limits of the systematics of (in our case) the CMS detector [118]. Even in the case of very high statistics for measuring the dilepton background, there is some irreducible uncertainty around the level of 1%, hence the choice of $S/B \sim 0.1$ as a systematic limit independent of collider energy. The positive thing to note here is that the signal is saturated only at large $\tilde{g}$, so one could feasibly use the dilepton channel to probe the parameter space of multi-doublet holographic models in future collider experiments. Of course, strictly speaking the experimental limits have been generated only for a single doublet case, however the interpretation of holographic predictions in the theory space still provides a useful guide to both theorists and experimentalists wishing to explore/exclude the WTC paradigm.

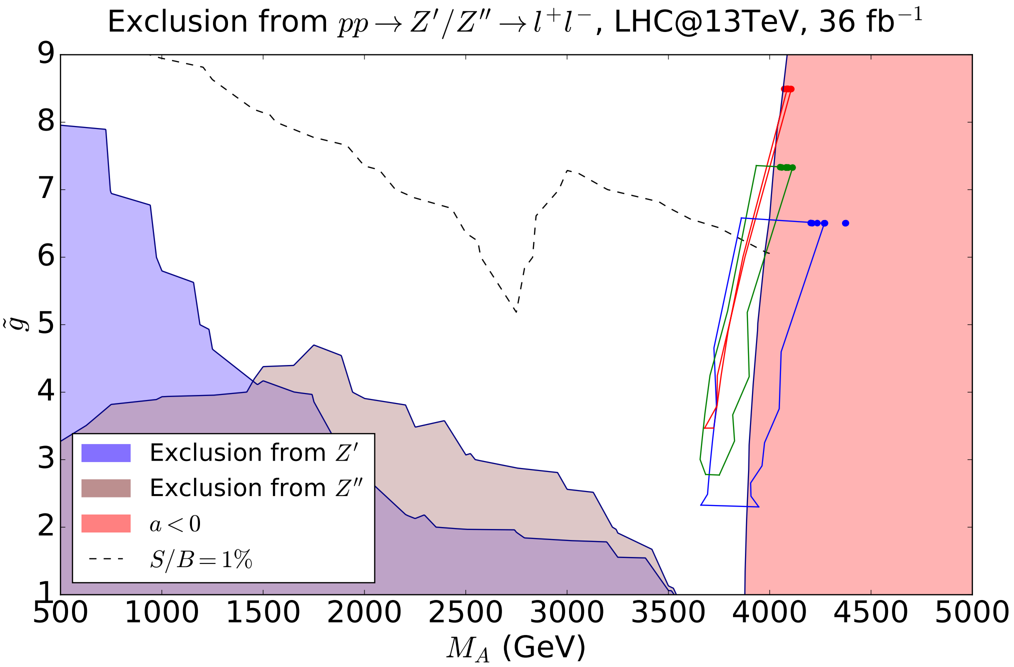

Figure 6.3: Excluded regions are 95% CL limit from neutral resonance dilepton searches at LHC@13TeV, $36 fb^{-1}$ in the $(M_A, \tilde{g})$ parameter space for Z', Z''. Limit on potential reach of dilepton searches from systematics is presented as the point at which Signal/Background¡0.01 (see 7.2). The predictions of the holographic model (tuned at each N_c, N_f to give S=0.1 and the correct higgs mass) are overlaid. The predictions are colour coded for the different N_c models; $N_c = 3$ is red, $N_c = 4$ is green, and $N_c = 5$ is blue. The top edge of the box in each case is the one electroweak doublet theory result with the width representing an estimate of the theoretical error (see section 6.2). The points correspond to the motion of the right hand point on that line as the number of singlets is changed to vary the UV running - the effect is small because the theories share much the same IR running to generate M_h. Moving down in the box corresponds to increasing the number of electroweak techni-doublets from one to $2N_c$ where the theories are assumed to enter the conformal window. Parameter a from the phenomenological model (equation 2.34), is related to $\rho - A$ degeneracy and the holographic points lie near the line $a = 0$ as a result of tuning to a small S parameter.

Chapter 7

The Future of NMWT at Colliders

7.1 Future High Energy Collider Experiments

Thus far we have established the up-to-date experimental limits on the NMWT parameter space from DY produced dilepton, VV, and Vh channels, as well as calculating from the top-down holographic model the spectrum of WTC theories of varying N_c, N_f which are projected into the $(M_A, \tilde{g})$ parameter space. At present, none of the DY produced neutral resonance searches at the LHC can probe the parameter space occupied by these holographic models, but will future collider experiments be able to explore this regime? How will the landscape of Walking Technicolor models change with the ever increasing capabilities of high energy physics experiments? Might it be possible to exclude or discover Walking Technicolor within our lifetime?

We begin the task of answering these important questions here, exploring the predicted reach of dilepton searches in the NMWT parameter space up to the proposed end point of the LHC[4], and in potential/planned future high energy collider experiments[5]. Plans for the HLLHC upgrades in beam energy and luminosity are detailed in [119], along with potential plans for both 27TeV and 100TeV colliders to be built in the LHC tunnel post-HLLHC. Section 7.2 describes the method of predicting experimental limits on neutral resonance dilepton searches, predicted exclusions on the NMWT parameter space are presented for several benchmark HLLHC points in section 7.3, and finally predicted exclusions on NMWT for 27TeV and 100TeV collider experiments are presented in section 7.4.

7.2 Recreating CMS 13TeV Dilepton Limits

Thus far the observed 95% CL limits have been used to set limits on the viable parameter space of NMWT, now we wish to emulate the limit setting procedure in order to predict analogous limits on NMWT at future experiments. We focus on predicting the limits of neutral resonances in dilepton searches due to its clean and simple to control background, allowing us to model the signal and background effectively without complications from jets/QCD processes as would appear in VV/Vh searches. The analysis is being extended to these channels with their more complicated background structure, which is the subject of our upcoming work [6].

Building from the CMS procedure for the observed dilepton limit as outlined in section 5.1.1, we design a procedure to simulate the expected CMS limit. One should note that our analysis method employs a *binned* likelihood method, as opposed to the CMS unbinned likelihood analysis. Our analysis is divided into two statistical regimes; where the number of background events is $N_{bg} > 10$ we model the signal as a Gaussian fluctuation over the background, and where $N_{bg} \leq 10$ we instead use Poisson statistics to model the signal. The background is modelled as smoothly falling with invariant dilepton mass, where the smooth distribution has been generated from many distributions in the invariant mass windows of interest. We assume that the resonance width for a generic Z' signal, $\Gamma_{Z'}$, is sufficiently narrow such that we can model the resonance using the Gaussian-smearing effect of the finite detector resolution. In the $N_b > 10$ regime the signal probability distribution function (PDF) is thus defined by a Gaussian peak of width $\Gamma_{Z'} = 1.2\% M_{Z'}$ (i.e equal to detector resolution), and in the $N_b \leq 10$ regime is modified by a signal strength modifier μ. In the Poisson regime we employ the CL_s method to evaluate the expected upper limit, where the background PDF is evaluated using a toy Monte-Carlo model.

To validate this method we generate the 95% CL limit for the LHC@13TeV and $36 fb^{-1}$ and compare it to the expected limit from CMS[80]. Figure 7.1 shows the limits we already have established from the current CMS dilepton resonance search, along with solid and dashed lines representing the *expected* limit from CMS and from our maximal binned likelihood analysis. The CMS expected limit closely follows that of the observed limit, with some deviation from statistical fluctuations at the experimental level. Our predicted limit is within % level agreement with the CMS limit setting procedure, so we conjecture that this method should reliably reproduce the CMS expected limits at higher energy and luminosity. We must make a few assumptions, such as that the detector resolution will remain around 1.2%, and that acceptance/efficiency functions ($A\times\epsilon$) will not change significantly at the HLLHC.

One should also note that the signal-to-background ratio S/B is not expected to change with the increase of the collider energy as the signal will scale the same way as the irreducible dilepton background for increasing $\sqrt{s}$, hence the limit on dileptons from the systematics will remain as presented in Figure 6.3. The scope of this analysis is to give an estimate of the potential of high energy/luminosity pp colliders to probe the NMWT parameter space, and to use these predictions as a guideline for theorists and experimentalists regarding how best to approach finding/excluding Walking Technicolor models.

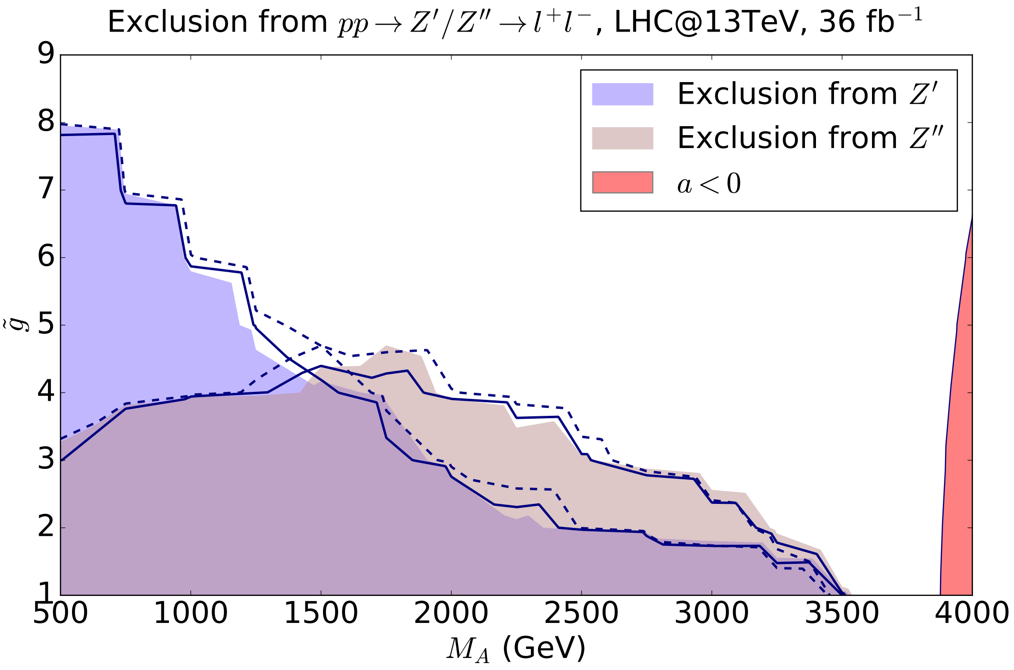

Figure 7.1: Observed 95% CL exclusion on the $M_A, \tilde{g}$ parameter space from the CMS dilepton resonance searches at the LHC@13TeV with $36 fb^{-1}$. Solid and dashed lines along the borders of the shaded area represent the expected CMS limit and our predicted limit using binned likelihood method respectively.

7.3 Prospects for Probing NMWT at HLLHC

With the set up and validation of our limit setting procedure described in section 7.2, we can now explore the potential for the LHC to probe the NMWT parameter space up to the expected end point of the High Luminosity LHC (HLLHC). To effectively explore how the increasing luminosity and centre-of-mass energy will impact the NMWT parameter space, we simulated projected limits at $\sqrt{s} = 13$TeV with $100 fb^{-1}$, $\sqrt{s} = 14$TeV with $300 fb^{-1}$, and the end-point of the HLLHC at $\sqrt{s} = 14$TeV with $3ab^{-1}$. To generate 14TeV dataset limits, the limit setting procedure (section 7.2) is repeated, but to convert the 13TeV background distribution into a 14TeV distribution the background probability density function is multiplied by an NNPDF scale factor.

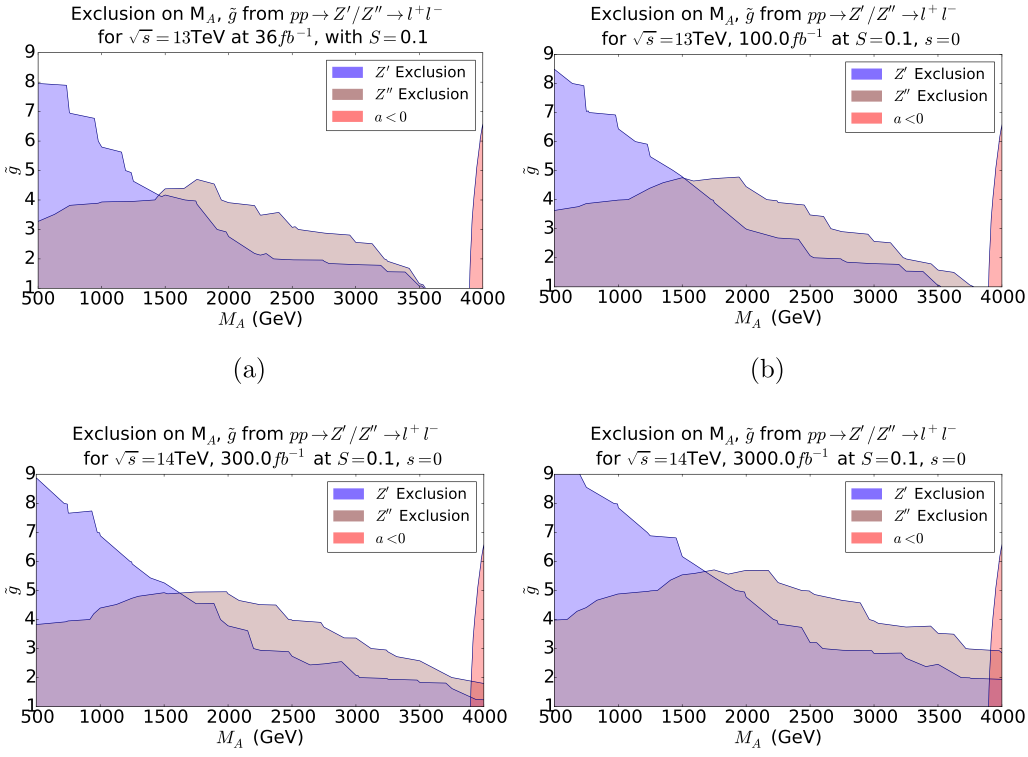

Exclusion on M$_A$, $\tilde{g}$ from $pp \rightarrow Z'/Z'' \rightarrow l^+ l^-$ for $\sqrt{s} = 13$TeV at 36fb^{-1}, with $S = 0.1$

Exclusion on M$_A$, $\tilde{g}$ from $pp \rightarrow Z'/Z'' \rightarrow l^+ l^-$ for $\sqrt{s} = 13$TeV, 100.0fb^{-1} at $S = 0.1$, $s = 0$

Exclusion on M$_A$, $\tilde{g}$ from $pp \rightarrow Z'/Z'' \rightarrow l^+ l^-$ for $\sqrt{s} = 14$TeV, 300.0fb^{-1} at $S = 0.1$, $s = 0$

Exclusion on M$_A$, $\tilde{g}$ from $pp \rightarrow Z'/Z'' \rightarrow l^+ l^-$ for $\sqrt{s} = 14$TeV, 3000.0fb^{-1} at $S = 0.1$, $s = 0$

(a)

(b)

(c)

(d)

Figure 7.2: Exclusion of the M_A-$\tilde{g}$ parameter space from Z' and Z'' DY processes at $\sqrt{s} = 13$TeV and luminosity of 36fb^{-1}(a); Predicted exclusion regions for the NMWT parameter space at (b) $\sqrt{s} = 13$TeV and $\mathcal{L} = 100 fb^{-1}$, (c)$\sqrt{s} = 14$TeV and $\mathcal{L} = 300 fb^{-1}$, (d) $\sqrt{s} = 14$TeV and $\mathcal{L} = 3000 fb^{-1}$.

The projected limit interpreted in the NMWT $(M_A, \tilde{g})$ parameter space at $S = 0.1$ is displayed in Figure 7.2, where we have also restated the current LHC@13TeV limits presented in section 5.2 for comparison. We also provide results for the projected 14TeV, $3ab^{-1}$ limits on $(M_A, \tilde{g})$ with varying $S = -0.1, 0.0, 0.2, 0.3$ in Figure C.16 of Appendix C. Already at $100fb^{-1}$ (Figure 7.2b) one can see that both the Z' and Z'' dilepton exclusions probe visibly further than the $36fb^{-1}$ limits. At low $\tilde{g}$ the Z'' probes significantly further in M_A, at $\tilde{g} = 1$ the limit improves in M_A from 3.5TeV to around 3.8TeV.

Increasing the centre-of-mass energy to $\sqrt{s} = 14$TeV and luminosity to $300fb^{-1}$ (Figure 7.2c), the bounds from dileptons at experiment and the theoretical upper limit on M_A of $a < 0$ begin to meet. In fact, for the whole region of $\tilde{g} < 2$ the NMWT model is excluded for all M_A, with the strongest exclusions coming from the Z'' in this regime. This alone is a powerful conclusion for the potential of the LHC to explore/exclude NMWT models, however looking to the end point of the HLLHC with an order of magnitude increase in the integrated luminosity (Figure 7.2d) significantly increases the exclusions on $(M_A, \tilde{g})$. The projected dilepton limit not only completely excludes NMWT models with $\tilde{g} < 3$, but also excludes up to $\tilde{g} = 9$ at low M_A.

It is notable that even at the final energy and luminosity of the HLLHC, the dilepton limit does not saturate the limit from the systematic uncertainty on $S/B < 1\%$ in this channel. This indicates that the potential of DY dileptons to probe NMWT can be even more powerful at future high energy colliders, which we discuss in the following section. The dilepton channel is powerful for excluding models outside of the high M_A, high $\tilde{g}$ regime, which motivates the projection of limits from complementary channels akin to the VV/Vh exclusions presented in section 5.3. This is the subject of our upcoming work [6].

7.4 Projected Limits for 27TeV and 100TeV Colliders

The projected limits at the end-point of the HLLHC show a promising improvement on the LHC@13TeV and $36fb^{-1}$ observed limits, however they are still insufficient to probe the important regime of high M_A and intermediate-high $\tilde{g}$. In fact, the LHC@14TeV and $3ab^{-1}$ only just begins to probe the space occupied by the most extreme top-down holographic models. For a total exclusion of the Walking Technicolor paradigm one would need to access and exclude the space of M_A from 3.5-5TeV, motivating the need for much higher collider energies. Furthermore, the most realistic top-down holographic model (the $SU(3)$ model with a single techni-quark doublet, i.e NMWT) lives in the space of $\tilde{g} \gg 1$, which given the $\tilde{g}^{-1}$ suppression of the difermion coupling is unlikely to be accessible by DY dileptons, and perhaps even inaccessible by any DY produced signature. This necessitates the projection of limits from both DY VV/Vh signatures (as in section 5.3) and VBF produced signatures.

To demonstrate and explore the limitations of DY dilepton searches, we have repeated the analysis described in section 7.2 for future colliders with $\sqrt{s} = 27, 100$TeV and integrated luminosity $15, 3ab^{-1}$ respectively. The resulting predicted exclusions in the NMWT parameter space are presented in Figure 7.3, along with the $S/B < 1\%$ systematic limit and the holographic spectra as calculated in chapter 6. The increase in energy and luminosity gives a significant improvement in sensitivity in the $M_A \sim 4$TeV, $\tilde{g} \simeq 4$ regime as compared to the HLLHC (Figure 7.2), such that between the Z'' dilepton exclusions and the theoretical limit of $a \geq 0$ all models up to this mass-coupling regime are excluded.

The 27TeV, $15ab^{-1}$ (Figure 7.3(top)) and 100TeV, $3ab^{-1}$ (Figure 7.3(bottom)) predicted exclusions are qualitatively very similar, with the main improvement by the 100TeV collider being the increased sensitivity to intermediate values of $\tilde{g}$ in the high M_A region. Dilepton searches at both of these collider energies/luminosities are able to probe top-down WTC models with a high number of techni-quark doublets, most notably for the gauge group $SU(3)$ which is inaccessible at the HLLHC. Unfortunately, the limits are still far from excluding the single doublet models at $\tilde{g} \sim 8$.

In the low-intermediate M_A regime, the dilepton limit at these higher energy/luminosity colliders begins to saturate the limit from the systematics, with complementarity of the Z' and Z'' signatures further highlighted. The dilepton limits for both 27TeV and 100TeV colliders are projected to be able to entirely exclude the regime of $M_A < 1$TeV which is useful in itself, however the lack of sensitivity and limit from systematics outside of this regime necessitates complementary experimental signatures.

One should note that VBF production of Z'/Z'' followed by VV or Vh decay are especially promising for the intermediate-high $\tilde{g}$ regime as the coupling strengths for $Z'^{('')}VV/Z'^{('')}Vh$ are not suppressed and can in fact grow with $\tilde{g}$ (see section 4.2). Already the LHC@13TeV $36fb^{-1}$ limits from DY produced VV/Vh searches (section 5.3) exclude more of the high $\tilde{g}$ regime than the dilepton counterparts, so the extension to VBF production may enhance the sensitivity in the vitally important high $\tilde{g}$, high M_A regime. This motivates exploration of these additional VV/VH signatures and VBF production channel, which could potentially cover the whole WTC parameter space[6].

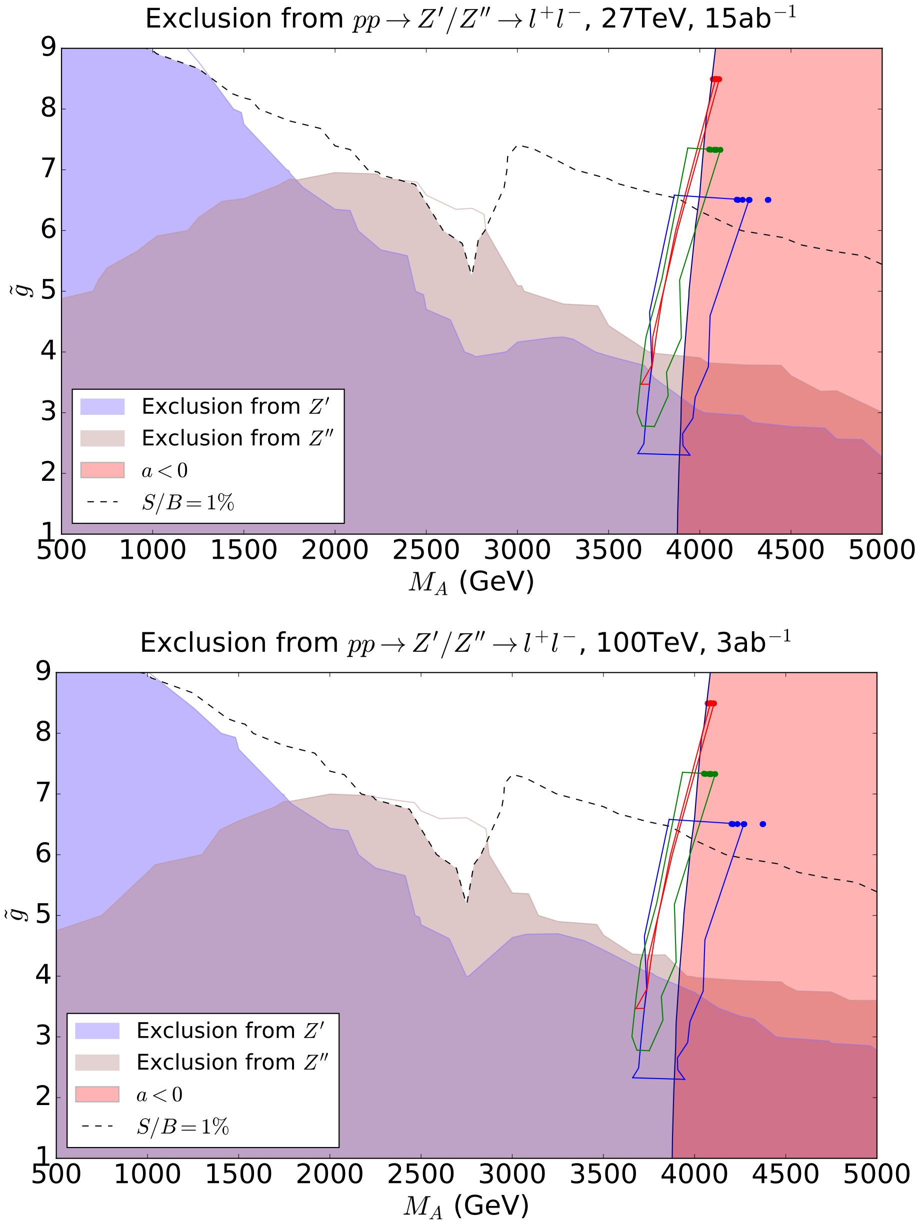

Figure 7.3: Projected 95% CL exclusion on the $M_A, \tilde{g}$ parameter space for 27TeV($15ab^{-1}$) (top) and 100 TeV ($3ab^{-1}$)(bottom) pp colliders from dilepton DY resonance searches. Notation for the holography predictions are the same as in Figure 6.3.

Chapter 8

Conclusions

The Walking Technicolor paradigm is a well motivated and phenomenologically rich BSM model, providing a dynamical origin for mass and producing a light composite Higgs consistent with experiment from a natural scale Λ_{TC}. In this thesis we have detailed the WTC model with the most minimal particle content, Next-to-Minimal Walking Technicolor (NMWT). We have connected the effective Lagrangian to the Weinberg Sum Rules, and discussed the theoretical upper limit on the axial mass M_A from the requirement of 'walking' dynamics in the 2nd WSR. We have performed and presented the first detailed analytic diagonalisation of the gauge mixing matrices, providing explicit analytic forms for the masses and couplings for the NMWT gauge particles and interactions. Constraints on the model from electroweak precision data (EWPD) are discussed through the lens of the Peskin-Takeuchi S parameter, which is sensitive to additional gauge particles in 1-loop corrections to EW gauge interactions. EWPD restricts to a small S, as such we study a range of $S = -0.1, 0, 0.1, 0.2, 0.3$, the largest of which is already strongly disfavoured however is included for comparison to previous studies for which $S = 0.3$ is the benchmark value.

We then detail a phenomenological study of NMWT, specifically in the context of new neutral resonances arising from the Technicolor dynamics. The presence of two gauge mesons, Z' and Z'', provide potential for complementary searches at colliders. These resonances exhibit a complex interdependence in terms of vector/axial vector composition, consequences of this are presented in detail. Analytic and numerical analyses of Z'/Z'' properties are explored, motivating the complementary study of both resonances and a number of decay channels at colliders. Previous studies on NMWT have utilised a 3D version of the model, presenting properties in the $(M_A, \tilde{g})$ plane with fixed $S = 0.3$. We extend this analysis for the above S values, as well as exploring the full 5D parameter space with non-zero s and ω parameters.

The $\sqrt{s} = 13$TeV, $36fb^{-1}$ LHC data is interpreted for an up-to-date view of the experimental limits on the viable NMWT parameter space. We establish new limits on the NMWT $(M_A, \tilde{g})$ parameter space from Drell-Yan produced Z' and Z'' in the dilepton final state. For this channel we provide the limits for fixed S in the usual $(M_A, \tilde{g})$ parameter space, as well as establishing the first limits from a full $(M_A, \tilde{g}, S, s)$ parameter scan from which the most optimistic and most conservative limits are established. The dilepton limit even in the most conservative case extends the limit for low $\tilde{g}$ up to $M_A \simeq 3.1$TeV, which is more than 1TeV higher than the previously established dilepton limit. In addition to the dilepton channel we have also established the first limits on NMWT from VV/Vh searches at the LHC, and demonstrate the new potential of these channels for both neutral and charged resonances to probe the intermediate-high $\tilde{g}$ regime.

We have also worked with Holography physicists to explore the Walking Technicolor paradigm from a top-down perspective. For WTC models with a range of N_c, N_f, the running behaviour of α_{TC} was modified in the IR to produce a sufficiently light Higgs, with the hope that one of these theories captures the true viable theory of WTC. The resulting holographic spectra are projected into the NMWT parameter space to explore the likely position of WTC models in theory space. The combination of top-down holography predictions with the bottom-up phenomenological model provides insight on the potential of the LHC to probe both NMWT and the WTC paradigm as a whole.

The whole idea of this thesis is to give insight on the viability of Walking Technicolor in the era of TeV scale collider experiments, and ultimately determine the future of Walking Technicolor. To this end, we develop a method for simulating expected 95% CL limits on Z'/Z'' in the DY dilepton channel, modelled after the CMS limit setting procedure. Validating our procedure to within a few % against CMS for $\sqrt{s} = 13$TeV, $36fb^{-1}$, we then simulate experimental limits for increased luminosity and energy up to the 14TeV, $3ab^{-1}$ end point of the High Luminosity LHC (HLLHC). We demonstrate that the LHC DY dilepton searches will have the power to completely exclude the NMWT model for low $\tilde{g}$, a promising result for eventual discovery/total exclusion of Walking Technicolor.

We also explore the potential of future high-energy colliders to probe the NMWT parameter space for the DY dilepton channel. For both a 27TeV, $15ab^{-1}$ collider and a 100TeV, $3ab^{-1}$ collider, the DY dileptons are projected to completely exclude NMWT for all $\tilde{g} < 4$. The projected limits also begin to cover some of the parameter space for the top-down Holographic models, however this also acts to highlight the limitations of DY dileptons. The most realistic (i.e most minimal N_c, N_f) top-down models are still far out of reach of the HLLHC and future high-energy colliders if one considers only the DY dilepton channel. To truly determine the future of Walking Technicolor, we must explore all complementary production and decay channels.

At the time of writing I am working with collaborators on developing a procedure for simulating the LHC limit setting procedure for the complementary VV/Vh channels. Procedures are being developed for both Drell-Yan and Vector Boson Fusion (VBF) production of neutral and charged V'/V'' resonances. Through this work we hope to access areas of the $(M_A, \tilde{g})$ parameter space complementary to the DY dileptons, as well as hopefully probing the regime at which the most minimal top-down models lie.

We have significantly improved upon previous exploration of and established potential of complementary searches to probe the NMWT parameter space, and the Walking Technicolor paradigm as a whole. It is my view from this work that with the additional production and decay channels, future collider experiments will conclusively exclude or discover Walking Technicolor.

Appendix A

Dependent Parameters of NMWT

Throughout the majority of this thesis we have set constraints on NMWT in the 4-D (often 3-D where the Higgs plays no role and $s = 0$) parameter space. However, if we allow deviations from the 1st WSR then we can explore a general treatment of all dependent parameters in terms of the 5 independent parameters $M_A, \tilde{g}, S, s, \omega$, where the simple replacement of $\omega = 0$ will bring these formulae into the 4-D framework that is commonly applied throughout this thesis. To clearly denote the dependent and independent parameters, here I will express all dependent parameters as functions, e.g

$$\chi(\tilde{g}, S) = \sqrt{1 - \frac{\tilde{g}^2 S}{8\pi}}. \tag{A.1}$$

We begin with the general equations 2.19 to 2.26 (inclusive). The first note is that the ω factor now appears in the coefficient of F_V^2 in the 1st WSR, so when constructing the functional form of M_V there is an additional factor of $(1 + 2\omega)$ multiplying M_V^2. Accounting for this factor and substituting for χ (equation 2.29) we have

$$M_V^2(M_A, \tilde{g}, S, \omega) = \frac{1}{1 + 2\omega}\left[M_A^2\left(1 - \frac{\tilde{g}^2 S}{8\pi}\right) + \frac{\tilde{g}^2}{2}F_\pi^2\right], \tag{A.2}$$

which of course recovers the original equation when the exact 1st WSR is strictly enforced. From this we can conclude a non-zero ω parameter acts to reduce M_V, in turn increasing the splitting of vector and axial masses. As the S parameter is tightly constrained by EWPD, this ω parameter cannot be too large in a viable theory. Varying ω above the per-mill level alters the W boson mass and $\sin\theta_W$ from their observed SM values, so the assumption of $\omega = 0$ throughout the main body of this thesis is valid. The remaining analysis is included for completeness.

An important note is that the vev associated with the EWSB, v, is not itself an independent and fixed parameter in NMWT but a function of independent parameters. This function can be derived simultaneously with the r_2 and r_3 functions. Taking the difference between the axial and vector mass-squared equations in 2.22, we can find an expression for $r_2 v^2$,

$$r_2 v^2 = \frac{2}{\tilde{g}^2}(M_A^2 - M_V^2(M_A, \tilde{g}, S, \omega)), \tag{A.3}$$

where the function $M_V^2(M_A, \tilde{g}, S, \omega)$ will be kept temporarily in this form for brevity.

An equation for $r_3 v^2$ is simply a rearrangement of equation 2.23,

$$r_3 v^2 = \frac{4}{\tilde{g}^2} M_A^2 (1 - \chi(\tilde{g}, S)). \tag{A.4}$$

Rearranging the definition of ω a linear equation in terms of coefficients of v^2 can be written as

$$v^2 - r_3 v^2 + r_2 v^2 = \frac{4}{\tilde{g}^2} \omega M_V^2(M_A, \tilde{g}, S, \omega), \tag{A.5}$$

which combined with the previous equations A.3 and A.4 then gives the vev function

$$v^2(M_A, \tilde{g}, S, \omega) = \frac{2}{\tilde{g}^2}[M_V^2(M_A, \tilde{g}, S, \omega)(1 + 2\omega) + M_A^2(1 - 2\chi(\tilde{g}, S)). \tag{A.6}$$

This can now be directly substituted into equations A.3 and A.4 to find the functional forms of r_2 and r_3,

$$
\begin{aligned}
r_2(M_A,\tilde{g},S,\omega) &= \frac{(M_A^2 - M_V^2(M_A,\tilde{g},S,\omega))}{M_V^2(M_A,\tilde{g},S,\omega)(1+2\omega) + M_A^2(1-2\chi(\tilde{g},S))} && \text{(A.7)}\\
r_3(M_A,\tilde{g},S,\omega) &= \frac{2M_A^2(1-\chi(\tilde{g},S))}{M_V^2(M_A,\tilde{g},S,\omega)(1+2\omega) + M_A^2(1-2\chi(\tilde{g},S))}. && \text{(A.8)}
\end{aligned}
$$

The Lagrangian mass parameter m is found from the addition of the axial and vector mass-squared equations in 2.22;

$$
2m^2 + \frac{\tilde{g}^2 v^2 s}{2} = M_V^2 + M_A^2, \tag{A.9}
$$

so the functional form of m is

$$
m(M_A,\tilde{g},S,s,\omega) = \frac{1}{\sqrt{2}}\sqrt{M_V^2(M_A,\tilde{g},S,\omega) + M_A^2 - \frac{\tilde{g}^2 v^2(M_A,\tilde{g},S,\omega)s}{2}}. \tag{A.10}
$$

Note that $m(M_A,\tilde{g},S,\omega,s)$ is the only Lagrangian parameter that has an explicit dependence on the s parameter, this can be understood by identifying m as the mass term for the $A_{L/R}$ fields in $\mathcal{L}_{boson}$ 2.5. The s parameter controls the coupling strength of the composite Higgs to the TC sector, so it is only natural that this ‘mass’ parameter m should depend on the strength of these interactions as to display the hallmarks of EWSB in the NMWT framework.

For completeness, a set of fully parameterised functions of the above is presented here.

$$
M_V^2(M_A,\tilde{g},S,\omega) = \frac{1}{(1+2\omega)}\left[\frac{\tilde{g}^2 F_\pi^2}{2} + M_A^2\left(1 - \frac{\tilde{g}^2 S}{8\pi}\right)\right], \tag{A.11}
$$

$$
v(M_A,\tilde{g},S,\omega) = \sqrt{F_\pi^2 + \frac{2M_A^2}{\tilde{g}^2}\left(1 - \sqrt{1 - \frac{\tilde{g}^2 S}{8\pi}}\right)^2}, \tag{A.12}
$$

$$
r_2(M_A,\tilde{g},S,\omega) = \frac{M_A^2(2\omega + \frac{\tilde{g}^2 S}{8\pi}) - \frac{\tilde{g}^2 F_\pi^2}{2}}{(1+2\omega)(\frac{\tilde{g}^2 F_\pi^2}{2} + M_A^2(1 - \sqrt{1 - \frac{\tilde{g}^2 S}{8\pi}})^2)}, \tag{A.13}
$$

$$r_3(M_A, \tilde{g}, S, \omega) = \frac{2M_A^2(1-\sqrt{1-\frac{\tilde{g}^2 S}{8\pi}})}{\frac{\tilde{g}^2 F_\pi^2}{2} + M_A^2(1-\sqrt{1-\frac{\tilde{g}^2 S}{8\pi}})^2}, \tag{A.14}$$

$$m(M_A, \tilde{g}, S, s, \omega) = \frac{1}{\sqrt{2+2\omega}}\sqrt{M_A^2\left(1+\left(1-\frac{\tilde{g}^2 S}{8\pi}\right)(1-s-2s\omega)\right) - \tilde{g}^2 F_\pi^2 \omega}. \tag{A.15}$$

Finally, let us express the a parameter of the 2nd WSR as a function of the NMWT parameter space,

$$a(M_A, \tilde{g}, S, \omega) = \frac{3}{2\pi^2(1+2\omega)^2}\left[\frac{\tilde{g}^2}{4} + \frac{M_A^2}{F_\pi^2}\left(1-\frac{\tilde{g}^2 S}{8\pi}\right) + \frac{4M_A^4}{F_\pi^4 \tilde{g}^2}(\omega+\omega^2)\right]. \tag{A.16}$$

A.0.1 Independent formulation of mass matrices

The mass matrices described in 3.1 can also be written in terms of independent parameters of the fully 5-dimensional description of NMWT,

$$\mathcal{M}_N^2 = \begin{pmatrix} \frac{g_1^2 M_A^2(1+\omega)}{\tilde{g}^2}(1-\frac{\tilde{g}^2 S}{8\pi}+\frac{F_\pi^2\tilde{g}^2}{2M_A^2}) & -\frac{g_1 g_2 M_A^2 \omega}{\tilde{g}^2}(1-\frac{\tilde{g}^2 S}{8\pi}+\frac{F_\pi^2\tilde{g}^2}{2M_A^2}) & \frac{g_1 M_A^2}{\sqrt{2}\tilde{g}}\sqrt{1-\frac{\tilde{g}^2 S}{8\pi}} & -\frac{g_1 M_A^2}{\sqrt{2}\tilde{g}}(1-\frac{\tilde{g}^2 S}{8\pi}+\frac{F_\pi^2\tilde{g}^2}{2M_A^2}) \\ -\frac{g_1 g_2 M_A^2 \omega}{\tilde{g}^2}(1-\frac{\tilde{g}^2 S}{8\pi}+\frac{F_\pi^2\tilde{g}^2}{2M_A^2}) & \frac{g_2^2 M_A^2(1+\omega)}{\tilde{g}^2}(1-\frac{\tilde{g}^2 S}{8\pi}+\frac{F_\pi^2\tilde{g}^2}{2M_A^2}) & -\frac{g_2 M_A^2}{\sqrt{2}\tilde{g}}\sqrt{1-\frac{\tilde{g}^2 S}{8\pi}} & -\frac{g_2 M_A^2}{\sqrt{2}\tilde{g}}(1-\frac{\tilde{g}^2 S}{8\pi}+\frac{F_\pi^2\tilde{g}^2}{2M_A^2}) \\ \frac{g_1 M_A^2}{\sqrt{2}\tilde{g}}\sqrt{1-\frac{\tilde{g}^2 S}{8\pi}} & -\frac{g_2 M_A^2}{\sqrt{2}\tilde{g}}\sqrt{1-\frac{\tilde{g}^2 S}{8\pi}} & M_A^2 & 0 \\ -\frac{g_1 M_A^2}{\sqrt{2}\tilde{g}}(1-\frac{\tilde{g}^2 S}{8\pi}+\frac{F_\pi^2\tilde{g}^2}{2M_A^2}) & -\frac{g_2 M_A^2}{\sqrt{2}\tilde{g}}(1-\frac{\tilde{g}^2 S}{8\pi}+\frac{F_\pi^2\tilde{g}^2}{2M_A^2}) & 0 & M_A^2(1-\frac{\tilde{g}^2 S}{8\pi}+\frac{F_\pi^2\tilde{g}^2}{2M_A^2}) \end{pmatrix}. \tag{A.17}$$

Appendix B

Analytic Diagonalisation in the $M_A > M_V$ Regime

The details of the analytic diagonalisation of $\mathcal{M}_N^2$ and $\mathcal{M}_C^2$ are laid out in section 3.2, and only encapsulates the parameter space below the mass inversion ($M_A < M_{inv}$). Outside of this regime, the Z' switches from being the mostly-axial to the mostly-vector resonance (and the converse for Z''). This corresponds to the gauge mixing matrix switching mass ordering of the technicolor gauge fields, switching columns/rows 3 and 4 to give the following mixing matrix;

$$\mathcal{M}_N^2 = \begin{pmatrix} \frac{g_1^2}{\tilde{g}^2} M_V^2 (1+\omega) & -\frac{g_1 g_2}{\tilde{g}^2} M_V^2 \omega & -\frac{g_1}{\sqrt{2}\tilde{g}} M_V^2 & \frac{g_1}{\sqrt{2}\tilde{g}} M_A^2 \chi \\ -\frac{g_1 g_2}{\tilde{g}^2} M_V^2 \omega & \frac{g_2^2}{\tilde{g}^2} M_V^2 (1+\omega) & -\frac{g_2}{\sqrt{2}\tilde{g}} M_V^2 & -\frac{g_2}{\sqrt{2}\tilde{g}} M_A^2 \chi \\ \frac{g_1}{\sqrt{2}\tilde{g}} M_A^2 \chi & -\frac{g_2}{\sqrt{2}\tilde{g}} M_A^2 \chi & M_V^2 & 0 \\ -\frac{g_1}{\sqrt{2}\tilde{g}} M_V^2 & -\frac{g_2}{\sqrt{2}\tilde{g}} M_V^2 & 0 & M_A^2 \end{pmatrix}, \tag{B.1}$$

where $\mathcal{M}_C^2$ the lower-right 3x3 submatrix of $\mathcal{M}_N^2$. Following the procedure of [4], we perturbatively diagonalise $\mathcal{M}_N^2$ in orders of $\tilde{g}^{-1}$ up to 2nd order. Here however expand without inserting the fully independent form for M_V, but note that M_V^2 scales as $\tilde{g}^2$. We then find that the diagonalising matrices for $\mathcal{M}_N^2$ and $\mathcal{M}_C^2$ are

$$\mathcal{N} = \begin{pmatrix} \frac{g_2}{\sqrt{g_1^2+g_2^2}} & \frac{g_1}{\sqrt{g_1^2+g_2^2}} & \frac{\sqrt{2}g_1g_2}{\tilde{g}\sqrt{g_1^2+g_2^2}} & 0 \\ \frac{g_1}{\sqrt{g_1^2+g_2^2}} & -\frac{g_2}{\sqrt{g_1^2+g_2^2}} & \frac{(g_1^2-g_2^2}{\sqrt{g_1^2+g_2^2}} & -\frac{\sqrt{g_1^2+g_2^2}\chi}{\sqrt{2}\tilde{g}} \\ -\frac{g_1}{\sqrt{2}\tilde{g}} & -\frac{g_2}{\sqrt{2}\tilde{g}} & 1 & \frac{2(g_1^2-g_2^2)M_V^2\chi}{\tilde{g}^2(M_A^2-4M_V^2)} \\ \frac{g_1\chi}{\sqrt{2}\tilde{g}} & -\frac{g_2\chi}{\sqrt{2}\tilde{g}} & \frac{2(g_2^2-g_1^2)M_A^2\chi}{\tilde{g}^2(4M_A^2-M_V^2)} & 1 \end{pmatrix}, \tag{B.2}$$

$$\mathcal{C} = \begin{pmatrix} 1 & \frac{g_2}{\sqrt{2}\tilde{g}} & \frac{g_2\chi}{\sqrt{2}\tilde{g}} \\ \frac{g_2}{\sqrt{2}\tilde{g}} & \frac{3g_2^2M_A^2\chi}{2\tilde{g}^2(3M_A^2-M_V^2)} & 1 \\ -\frac{g_2}{\sqrt{2}\tilde{g}} & 1 & -\frac{3g_2^2M_V^2\chi}{2\tilde{g}^2(M_A^2-3M_V^2)} \end{pmatrix}. \tag{B.3}$$

Appendix C

Phenomenology of Z'/Z'' with $S \neq 0.1$

Here we provide the additional figures and information relevant to the phenomenological study presented in chapter 4. Throughout this chapter the results were presented at benchmark values of $S = 0.1$, $s = 0$, and $\omega = 0$. The effect of varying S is discussed here. As s is the Lagrangian parameter that quantifies Higgs interactions with the WTC gauge bosons, we continue to assume $s = 0$ throughout.

Mass Spectra

Figures C.1 and C.2 present $M_{Z'}$ and $\Delta M/M_{Z'}$ respectively for different values of S. The main feature to note is the mass inversion M_{inv} defined by Eq.(4.3) such that $M_{inv}^2 \propto 1/S$. The inversion point with $\Delta M \simeq 0$ can be seen in Fig C.2 where the Z' is axial-vector below the inversion point and vector above it. One can observe the inversion only for large values of $S = 0.2$ and 0.3 for the M_A around 2 and 1.6 TeV respectively according to the Eq.(4.3).

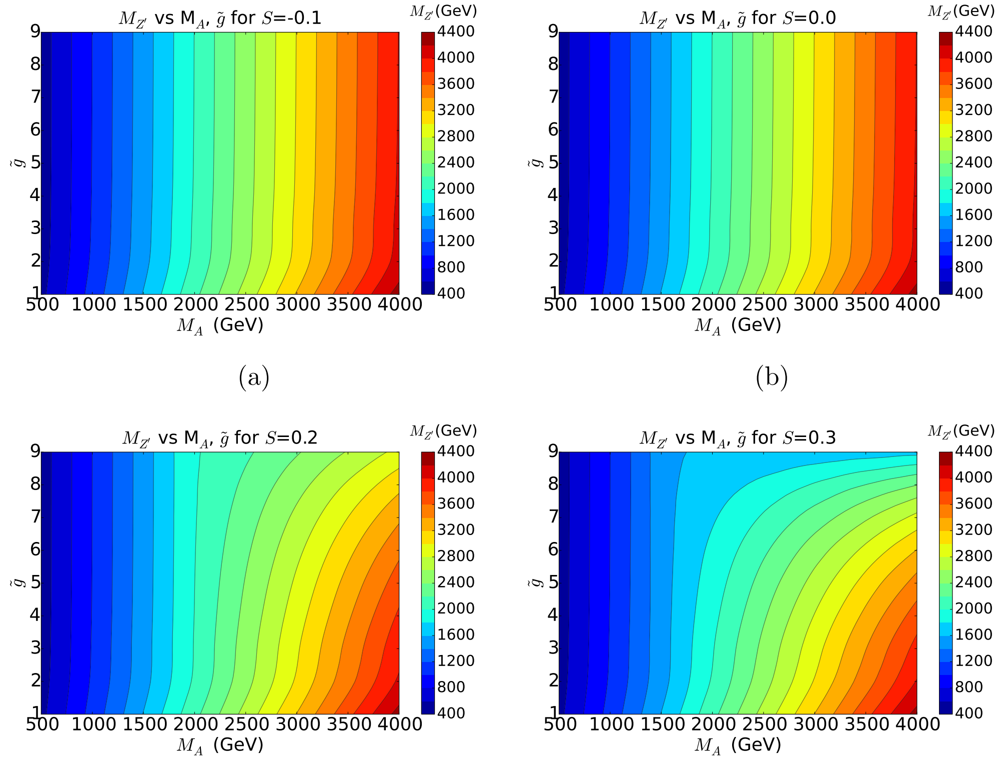

(a)

(b)

(c)

(d)

Figure C.1: $M_{Z'}$(GeV) as a function of M_A and $\tilde{g}$ parameters for the fixed values of $S = -0.1$ (a), $S = 0.0$ (b), $S = 0.2$ (c), $S = 0.3$ (d) respectively, and $s = 0$ throughout

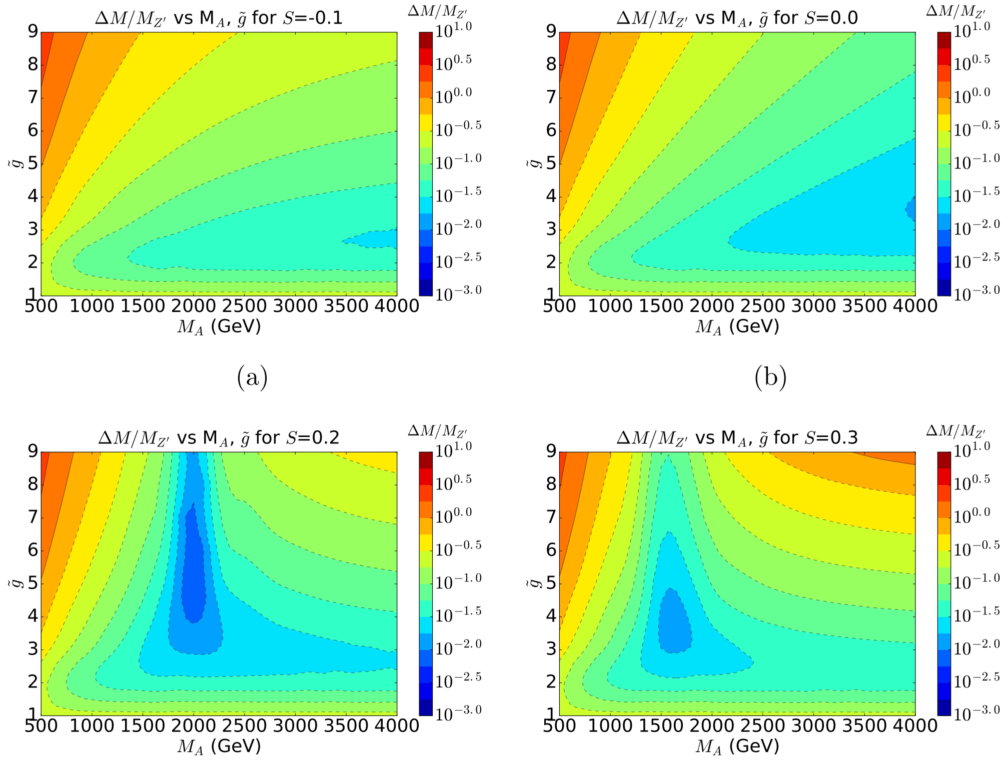

$\Delta M/M_{Z'}$ vs M$_A$, $\tilde{g}$ for S=-0.1

$\Delta M/M_{Z'}$ vs M$_A$, $\tilde{g}$ for S=0.0

$\Delta M/M_{Z'}$ vs M$_A$, $\tilde{g}$ for S=0.2

$\Delta M/M_{Z'}$ vs M$_A$, $\tilde{g}$ for S=0.3

(a)

(b)

(c)

(d)

Figure C.2: $\Delta M/M_{Z'}$ as a function of M_A and $\tilde{g}$ parameters for the fixed values of $S = -0.1$ (a), $S = 0.0$ (b), $S = 0.2$ (c), $S = 0.3$ (d) respectively, and $s = 0$ throughout

Couplings

In Figures C.3-C.4 and Figures C.5-C.6 we present the L-R components of the dilepton couplings for the Z' and Z'', respectively, for different values of S. These are analogous to the couplings presented in section 4.2.1, where the analytic form for the coupling components are also presented. The S dependence of these couplings is implicit in χ, g_1, and g_2, and the effect on the parameter space dependence for varying S is presented here.

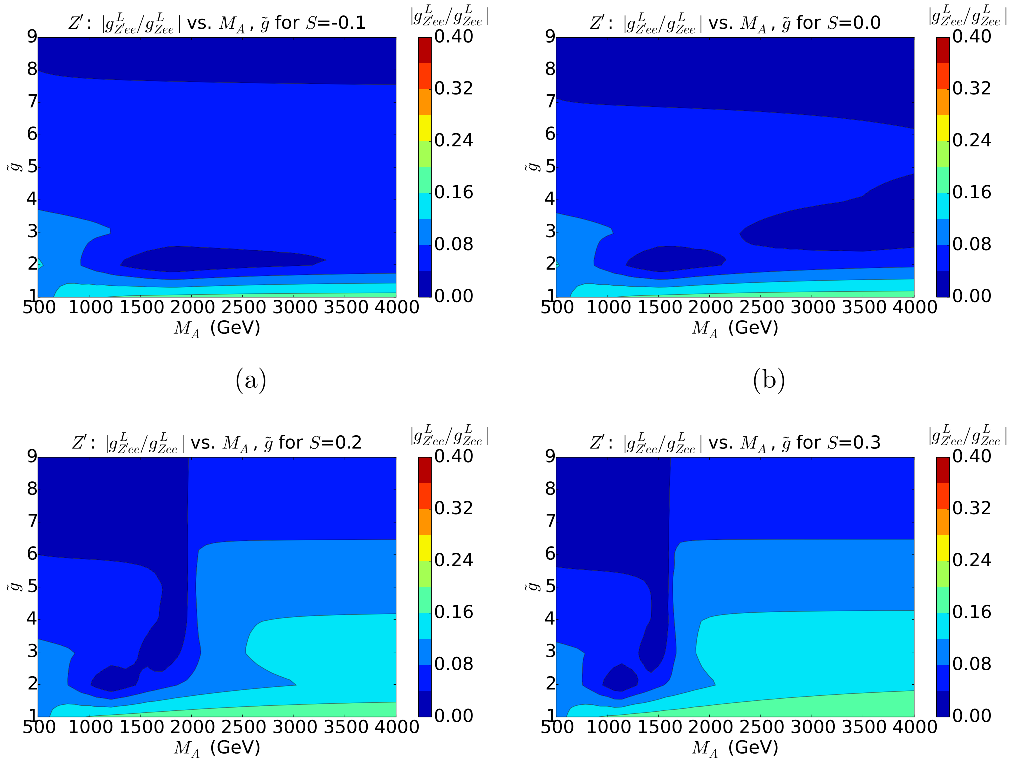

(a) (b)

(c) (d)

Figure C.3: Left handed component of the coupling of Z' to charged lepton pairs as a ratio to its SM equivalent, $|\ g_{Z'l^+l^-}/g_{Zl^+l^-}\ |$, as a function of M_A and $\tilde{g}$ parameters for the fixed values of $S = -0.1$ (a), $S = 0.0$ (b), $S = 0.2$ (c), $S = 0.3$ (d) respectively

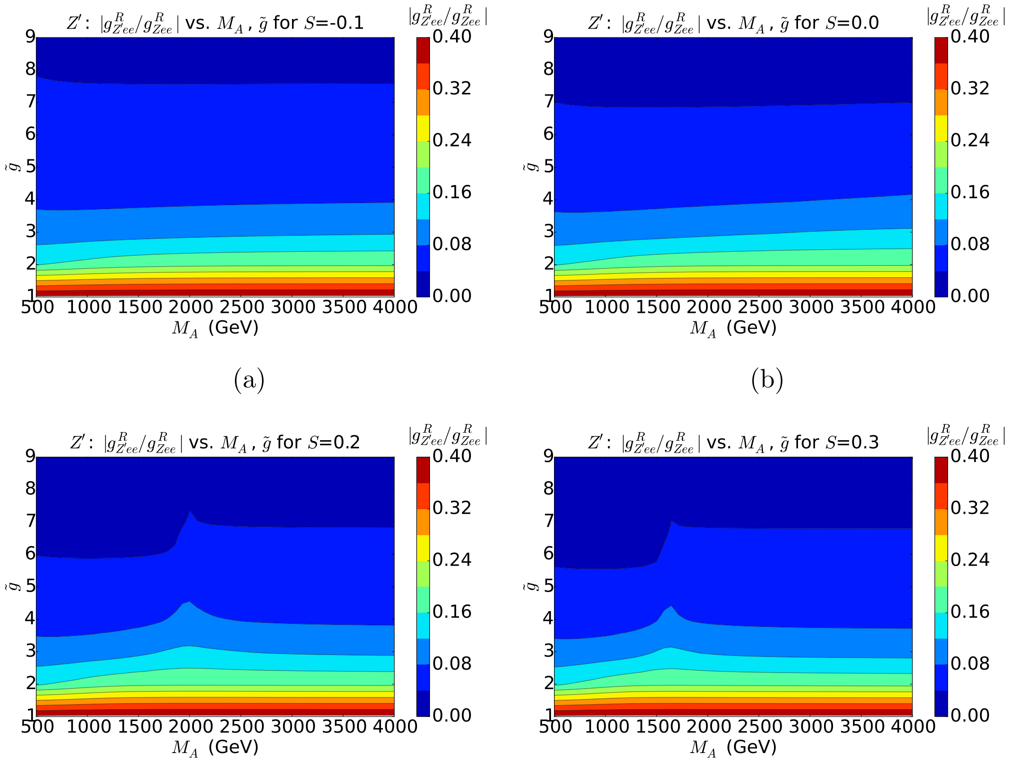

(a) (b)

(c) (d)

Figure C.4: Right handed component of the coupling of Z' to charged lepton pairs as a ratio to its SM equivalent, $\mid g_{Z'l^+l^-}/g_{Zl^+l^-} \mid$, as a function of M_A and $\tilde{g}$ parameters for the fixed values of $S = -0.1$ (a), $S = 0.0$ (b), $S = 0.2$ (c), $S = 0.3$ (d) respectively

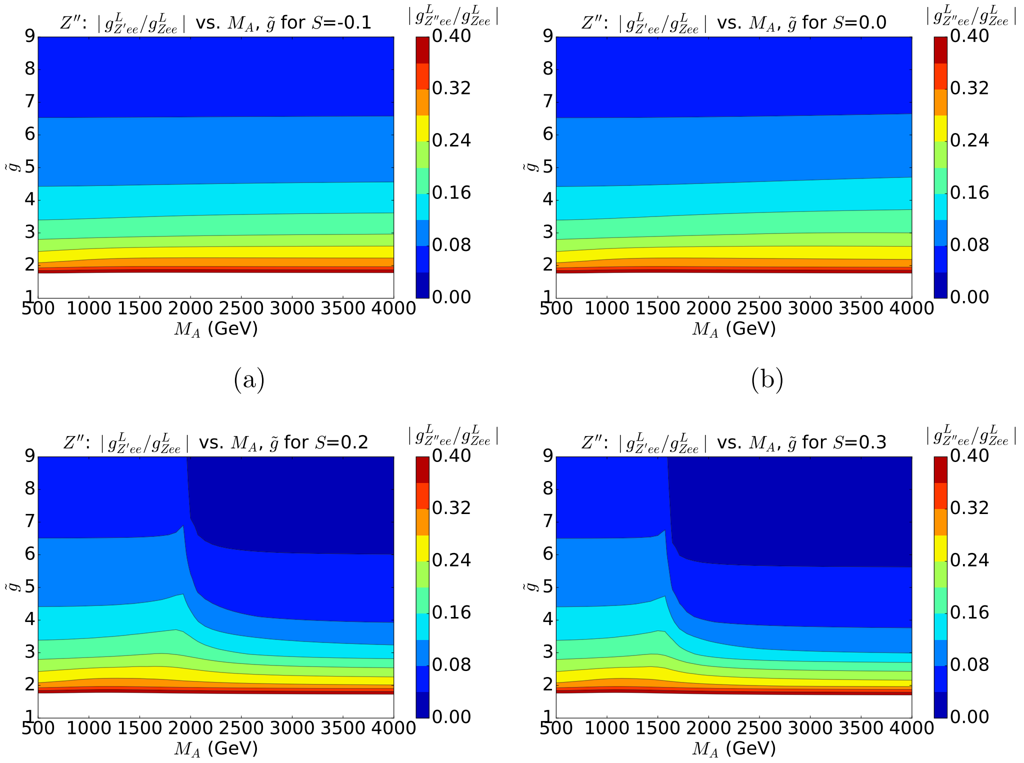

(a)

(b)

(c)

(d)

Figure C.5: Left handed component of the coupling of Z'' to charged lepton pairs as a ratio to its SM equivalent, $\mid g_{Z''l^+l^-}/g_{Zl^+l^-} \mid$, as a function of M_A and $\tilde{g}$ parameters for the fixed values of $S = -0.1$ (a), $S = 0.0$ (b), $S = 0.2$ (c), $S = 0.3$ (d) respectively

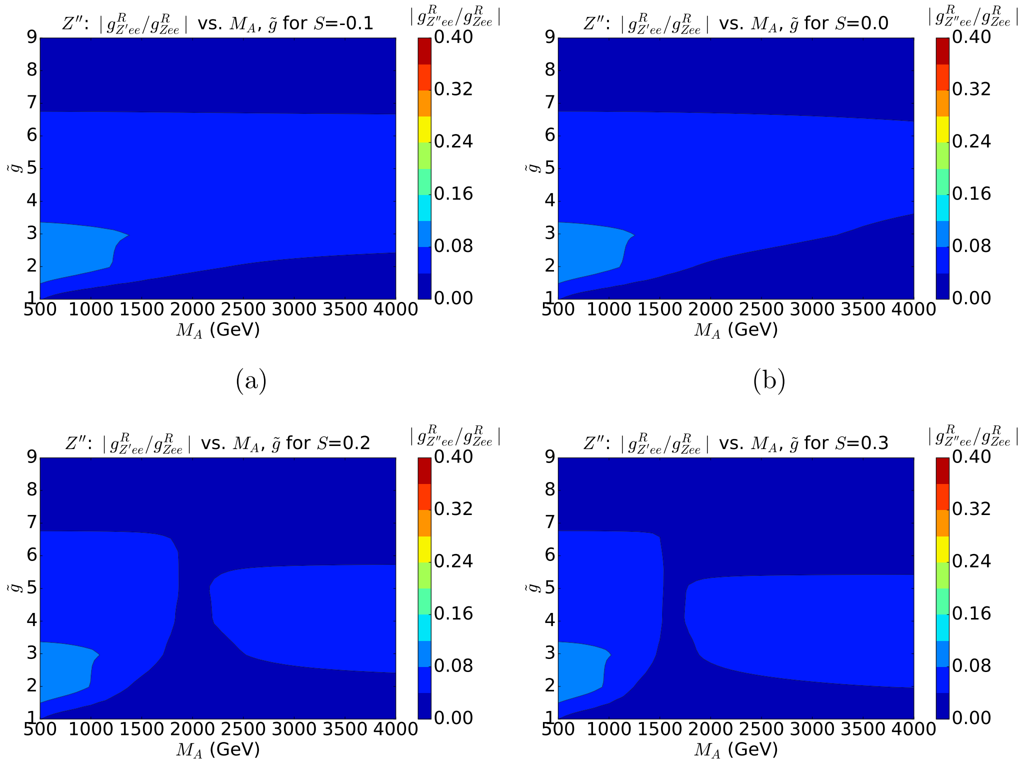

(a) (b)

(c) (d)

Figure C.6: Right handed component of the coupling of Z'' to charged lepton pairs as a ratio to its SM equivalent, $|\ g_{Z''l^+l^-}/g_{Zl^+l^-}\ |$, as a function of M_A and $\tilde{g}$ parameters for the fixed values of $S = -0.1$ (a), $S = 0.0$ (b), $S = 0.2$ (c), $S = 0.3$ (d) respectively

Widths and branching ratios

The width to mass ratio for Z' and $Z''$for different S are shown in Figures C.7 and C.8. The widths largely show similar behaviour to those at the benchmark value of $S = 0.1$ (Figure 4.4), with the exception of $S = 0$. At $S = 0$, the Z' width to mass ratio is very small (less than 1% level), so the Z' resonance is always narrow at this S. The Z'' also has a narrower width for much of the parameter space at $S = 0$, however the region of $\Gamma_{Z''} \geq M_{Z''}$ nevertheless appears in the region with low M_A and high $\tilde{g}$.

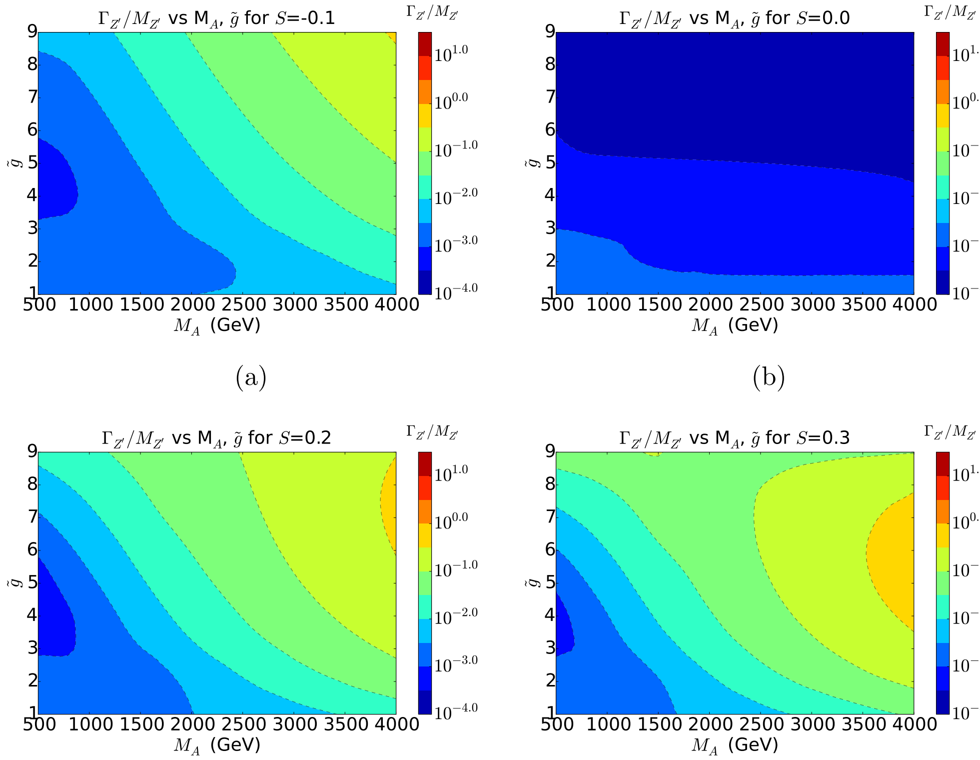

(a) (b)

(c) (d)

Figure C.7: $\Gamma_{Z'}/M_{Z'}$ as a function of M_A and $\tilde{g}$ parameters for the fixed values of $S = -0.1$ (a), $S = 0.0$ (b), $S = 0.2$ (c), $S = 0.3$ (d) respectively

The branching ratio spectra for the Z' with $\tilde{g} = 3, 8$ is presented in Figures C.9,C.10), and for the Z'' with $\tilde{g} = 3, 8$ — in Figures C.11, C.12 for various values S. The features of the branching ratio spectra such as the dips in the VV/Vh channels are discussed in section 4.3, and again we note that the $Z'' \to W'^{+}W'^{-}$ channel is opened at low M_A, high $\tilde{g}$ at all values of S. Also note that for the Z', at $S = 0$ where the resonance is very narrow,

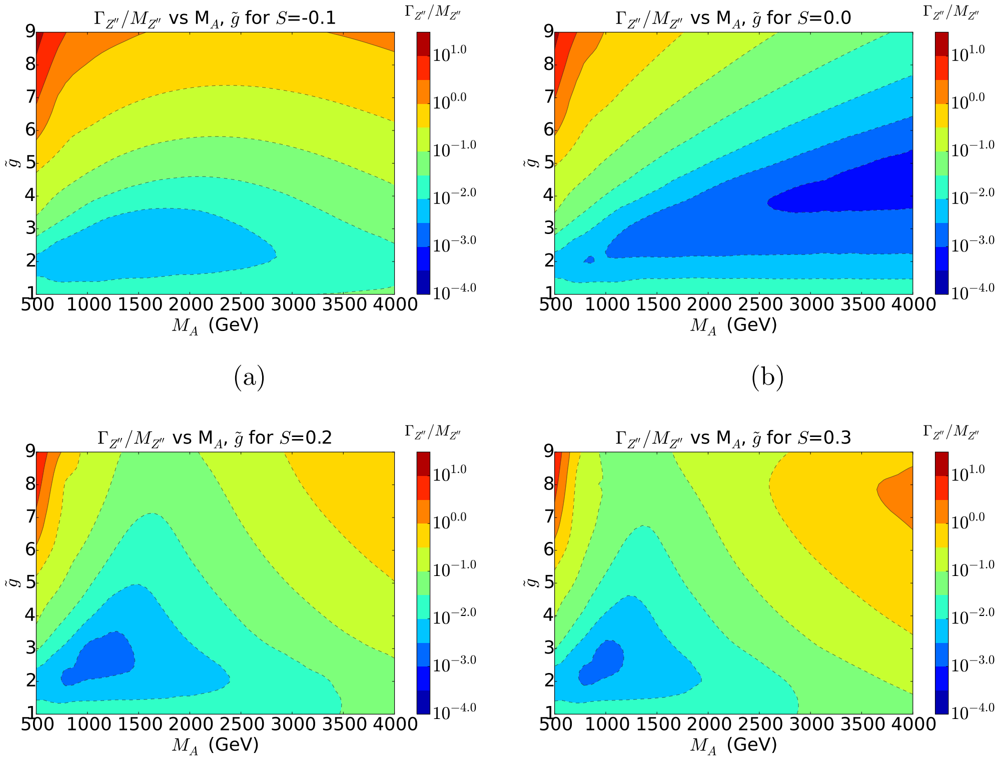

(a) (b)

(c) (d)

Figure C.8: $\Gamma_{Z''}/M_{Z''}$ as a function of M_A and $\tilde{g}$ parameters for the fixed values of $S = -0.1$ (a), $S = 0.0$ (b), $S = 0.2$ (c), $S = 0.3$ (d) respectively

the dilepton and diquark branching ratios are boosted and are the dominant decay channels across the whole (M_A, $\tilde{g}$) parameter space.

Again, the mass inversion point can also be identified as the point at which the W^+W^- and Zh branching ratios have a crossing point, hence the lack of crossing point at $S = -0.1, 0$.

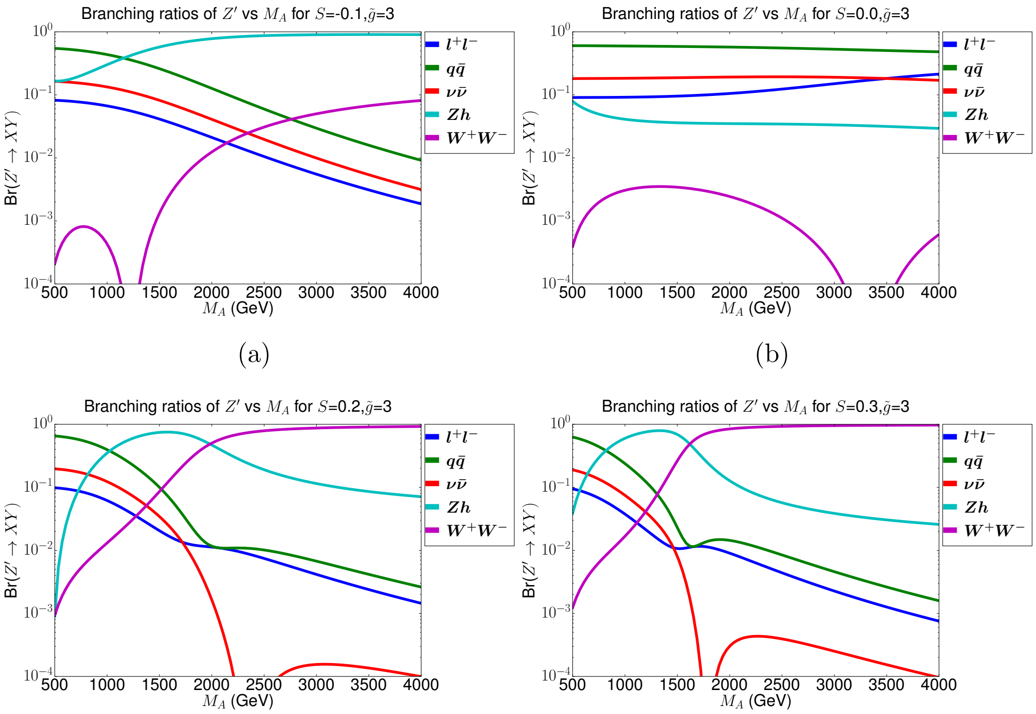

(a)

(b)

(c)

(d)

Figure C.9: $Br(Z')$ for all decay channels as a function of M_A at fixed value of $\tilde{g} = 3$ for $S = -0.1$ (a), $S = 0.0$ (b), $S = 0.2$ (c), $S = 0.3$ (d) respectively

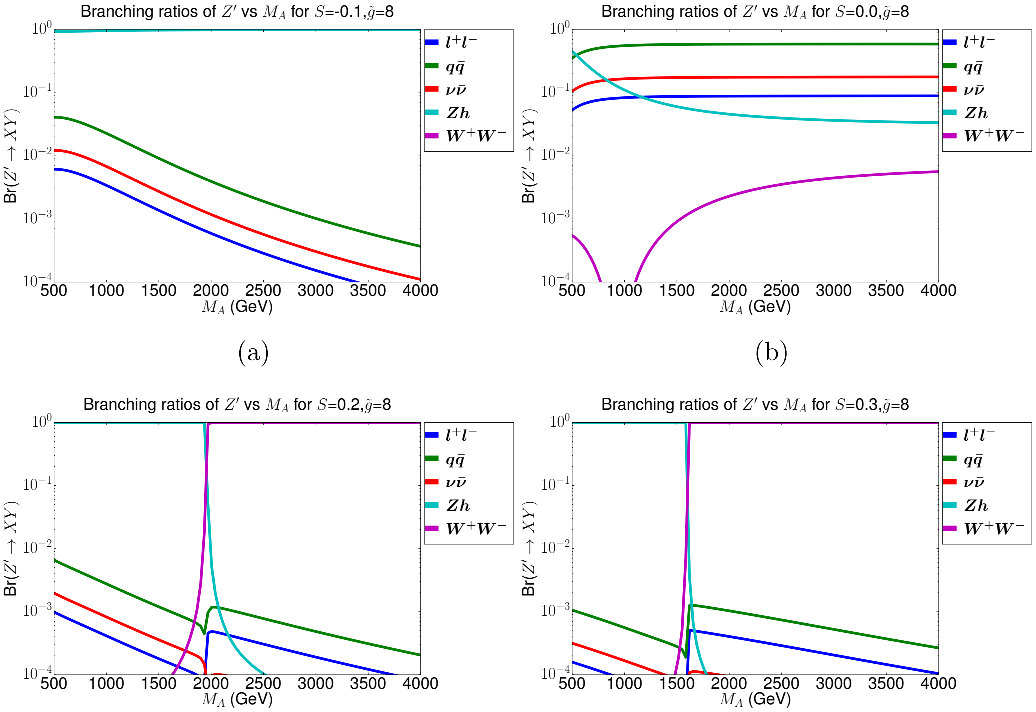

(a)

(b)

(c)

(d)

Figure C.10: $Br(Z')$ for all decay channels as a function of M_A at fixed value of $\tilde{g} = 8$ for $S = -0.1$ (a), $S = 0.0$ (b), $S = 0.2$ (c), $S = 0.3$ (d) respectively

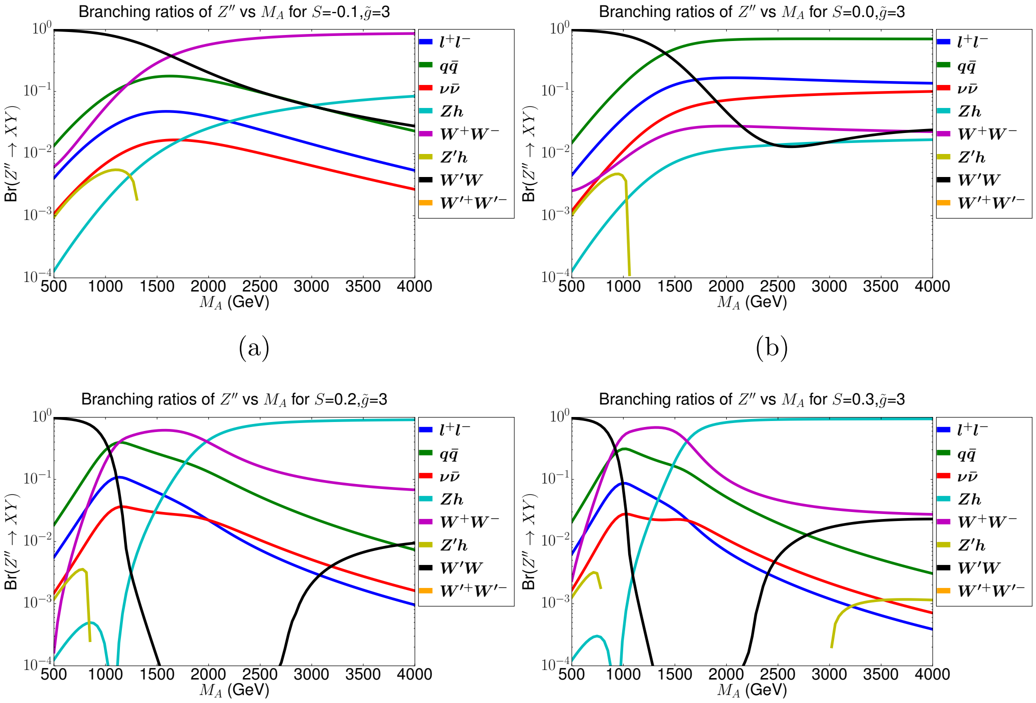

(a) (b) (c) (d)

Figure C.11: $Br(Z'')$ for all decay channels as a function of M_A at fixed value of $\tilde{g} = 3$ for $S = -0.1$ (a), $S = 0.0$ (b), $S = 0.2$ (c), $S = 0.3$ (d) respectively

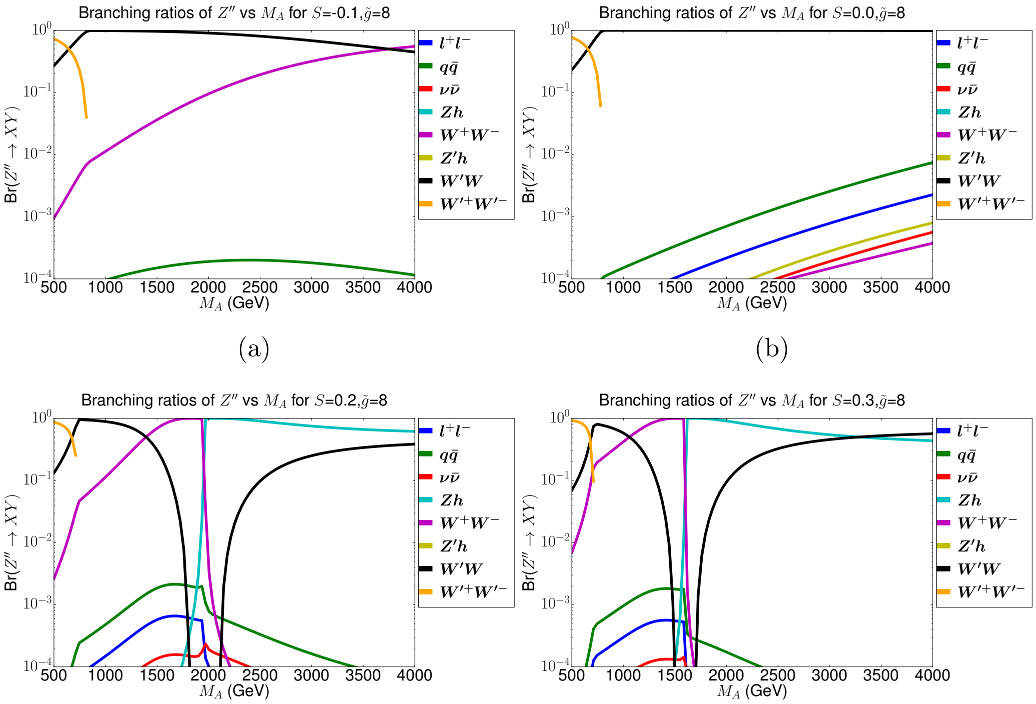

(a) (b)

(c) (d)

Figure C.12: $Br(Z'')$ for all decay channels as a function of M_A at fixed value of $\tilde{g} = 8$ for $S = -0.1$ (a), $S = 0.0$ (b), $S = 0.2$ (c), $S = 0.3$ (d) respectively

Cross sections

The DY production cross sections at LO for $pp \to Z' \to e^+e^-$ and $pp \to Z'' \to e^+e^-$ processes are presented in Fig. C.13 and Fig. C.14 respectively as contour levels of the cross section in $(M_A, \tilde{g})$ space for different S.

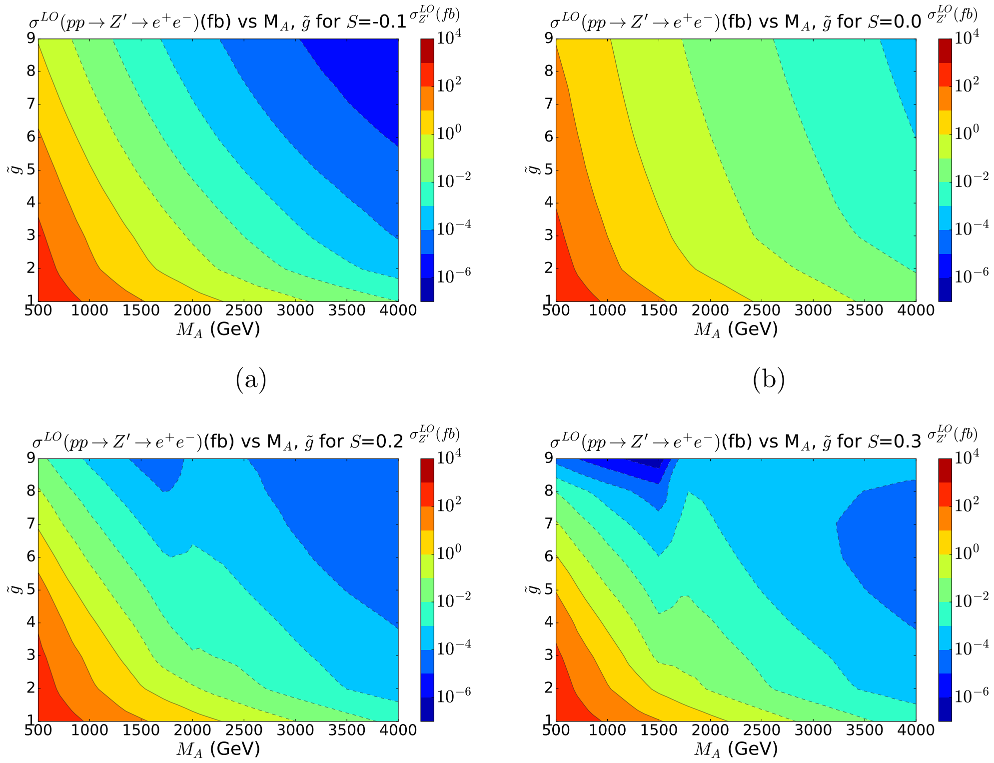

(a)

(b)

(c)

(d)

Figure C.13: DY production cross sections at LO for $pp \to Z' \to e^+e^-$ for $S = -0.1$ (a), $S = 0.0$ (b), $S = 0.2$ (c), $S = 0.3$ (d) respectively

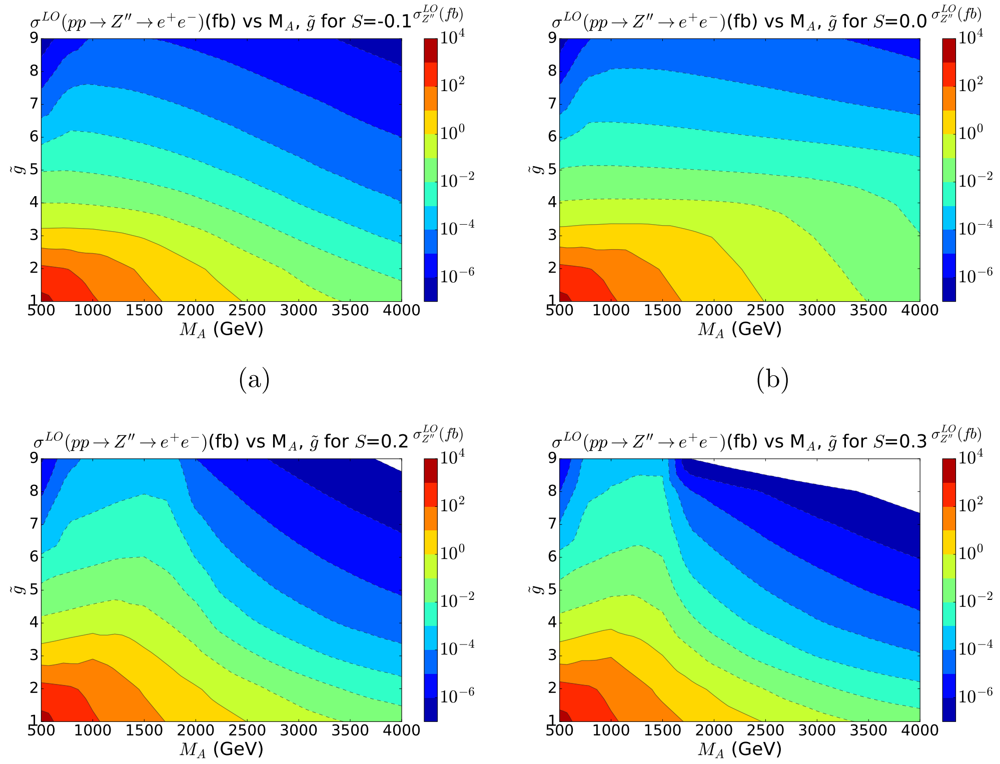

(a) (b)

(c) (d)

Figure C.14: DY production cross sections at LO for $pp \to Z'' \to e^+e^-$ for $S = -0.1$ (a), $S = 0.0$ (b), $S = 0.2$ (c), $S = 0.3$ (d) respectively

C.0.1 Effect of S on Drell-Yan NMWT Exclusions

As noted in section 5.2, the S parameter could be of great importance in determining the excluded region of WTC parameter space. As such, we present a set of figures for each discrete S in which we show the LHC@13TeV, $36fb^{-1}$ Drell-Yan dilepton limits on the WTC parameter space for fixed S. This is for direct comparison to the exclusions quoted and discussed in section 5.2. Figure C.15(a,b,c,d) show the excluded regions of M_A, $\tilde{g}$ for $S = -0.1, 0, 0.2, 0.3$ respectively.

The projected limits depend strongly on the S parameter, and for large S, the limit from dilepton searches at the LHC covers less of the parameter space, while the theoretical limit requiring $a > 0$ excludes a large portion of the M_A parameter space from above.

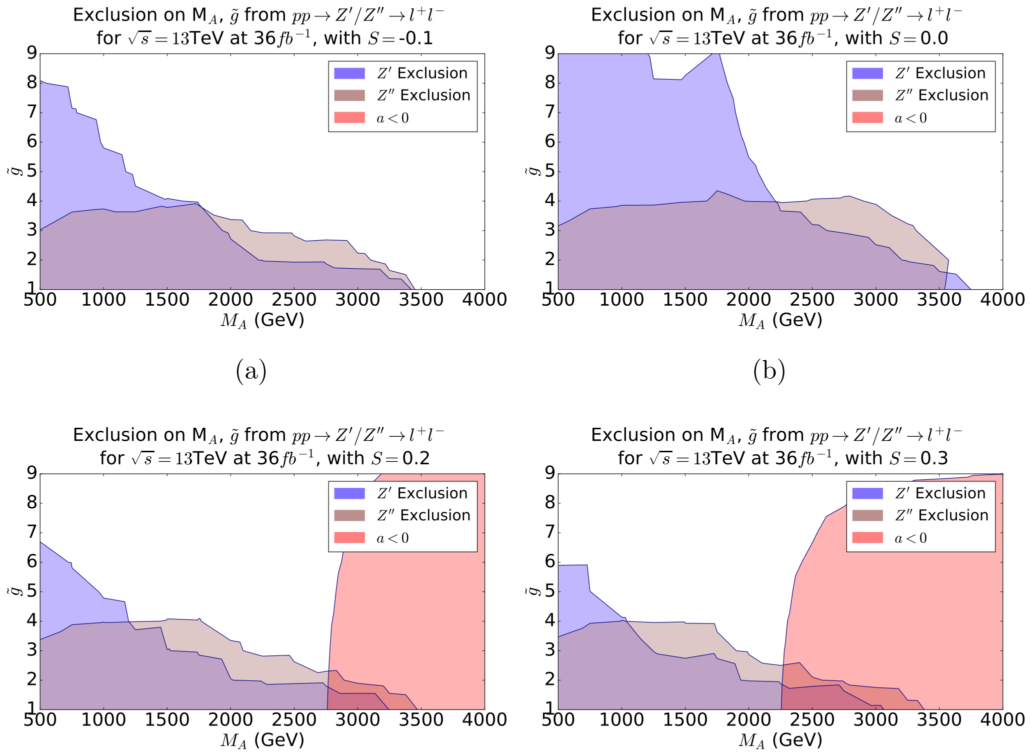

(a) (b)

(c) (d)

Figure C.15: Exclusion of the M_A,$\tilde{g}$ parameter space from Z' and Z'' DY processes at $\sqrt{s} = 13$TeV and luminosity of 36fb^{-1} for $S = -0.1$ (a), $S = 0.0$ (b), $S = 0.2$ (c), $S = 0.3$ (d) respectively

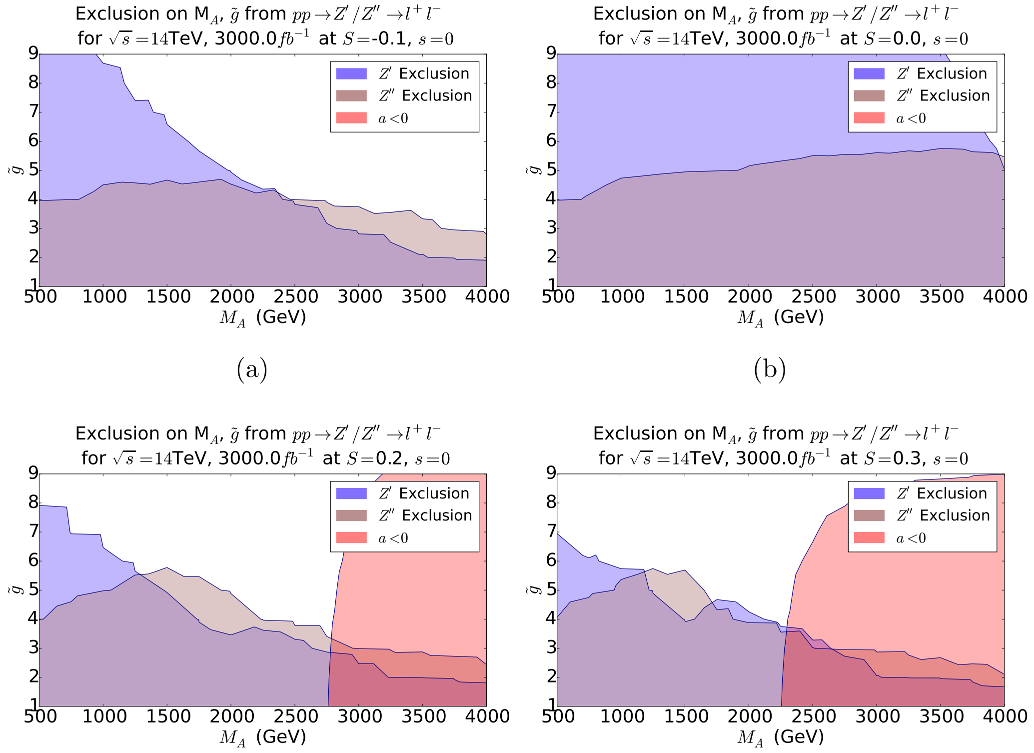

(a)

(b)

(c)

(d)

Figure C.16: Exclusion of the M_A,$\tilde{g}$ parameter space from Z' and Z'' DY processes at $\sqrt{s}$ = 14TeV and luminosity of $3000fb^{-1}$ for $S = -0.1$ (a), $S = 0.0$ (b), $S = 0.2$ (c), $S = 0.3$ (d) respectively

Bibliography

[1] J. Haller, A. Hoecker, R. Kogler, K. Mönig, T. Peiffer, and J. Stelzer, *Update of the global electroweak fit and constraints on two-Higgs-doublet models*, *Eur. Phys. J.* **C78** (2018), no. 8 675, [`arXiv:1803.0185`].

[2] **Gfitter Group** Collaboration, M. Baak, J. Cúth, J. Haller, A. Hoecker, R. Kogler, K. Mönig, M. Schott, and J. Stelzer, *The global electroweak fit at NNLO and prospects for the LHC and ILC*, *Eur. Phys. J.* **C74** (2014) 3046, [`arXiv:1407.3792`].

[3] R. D. Ball et al., *Parton distributions with LHC data*, *Nucl. Phys.* **B867** (2013) 244–289, [`arXiv:1207.1303`].

[4] A. Belyaev, A. Coupe, M. Frandsen, E. Olaiya, and C. Shepherd-Themistocleous, *Walking technicolor in light of Z′ searches at the LHC*, *Phys. Rev.* **D99** (2019), no. 5 055004, [`arXiv:1805.1086`].

[5] A. Belyaev, A. Coupe, N. Evans, D. Locke, and M. Scott, *Any Room Left for Technicolor? Dilepton Searches at the LHC and Beyond*, *Phys. Rev.* **D99** (2019), no. 9 095006, [`arXiv:1812.0905`].

[6] A. Belyaev, A. Coupe, N. Evans, and D. Locke, “Probing walking technicolor with vv and vh searches at the lhc.” Publication upcoming.

[7] **CMS** Collaboration, S. Chatrchyan et al., *Observation of a new boson at a mass of 125 GeV with the CMS experiment at the LHC*, *Phys. Lett.* **B716** (2012) 30–61, [`arXiv:1207.7235`].

[8] **ATLAS** Collaboration, G. Aad et al., *Observation of a new particle in the search for the Standard Model Higgs boson with the ATLAS detector at the LHC*, *Phys. Lett.* **B716** (2012) 1–29, [`arXiv:1207.7214`].

[9] L. Susskind, *Dynamics of Spontaneous Symmetry Breaking in the Weinberg-Salam Theory*, *Phys. Rev.* **D20** (1979) 2619–2625.

[10] S. Weinberg, *Implications of Dynamical Symmetry Breaking*, *Phys. Rev.* **D13** (1976) 974–996. [Addendum: Phys. Rev.D19,1277(1979)].

[11] M. E. Peskin and T. Takeuchi, *Estimation of oblique electroweak corrections*, *Phys. Rev.* **D46** (1992) 381–409.

[12] F. Sannino and K. Tuominen, *Orientifold theory dynamics and symmetry breaking*, *Phys. Rev.* **D71** (2005) 051901, [`hep-ph/0405209`].

[13] D. D. Dietrich and F. Sannino, *Conformal window of SU(N) gauge theories with fermions in higher dimensional representations*, *Phys. Rev.* **D75** (2007) 085018, [`hep-ph/0611341`].

[14] T. A. Ryttov and F. Sannino, *Conformal Windows of SU(N) Gauge Theories, Higher Dimensional Representations and The Size of The Unparticle World*, *Phys. Rev.* **D76** (2007) 105004, [`arXiv:0707.3166`].

[15] T. A. Ryttov and F. Sannino, *Supersymmetry inspired QCD beta function*, *Phys. Rev.* **D78** (2008) 065001, [`arXiv:0711.3745`].

[16] D. D. Dietrich, F. Sannino, and K. Tuominen, *Light composite Higgs from higher representations versus electroweak precision measurements: Predictions for CERN LHC*, *Phys. Rev.* **D72** (2005) 055001, [`hep-ph/0505059`].

[17] M. Gell-Mann, *Symmetries of baryons and mesons*, *Phys. Rev.* **125** (Feb, 1962) 1067–1084.

[18] S. L. Glashow, *Partial Symmetries of Weak Interactions*, *Nucl. Phys.* **22** (1961) 579–588.

[19] S. Weinberg, *A Model of Leptons*, *Phys. Rev. Lett.* **19** (1967) 1264–1266.

[20] A. Salam, *Weak and Electromagnetic Interactions*, *Conf. Proc.* **C680519** (1968) 367–377.

[21] Y. Nambu, *Quasi-particles and gauge invariance in the theory of superconductivity*, *Phys. Rev.* **117** (Feb, 1960) 648–663.

[22] J. Goldstone, *Field theories with superconductor solutions*, *Il Nuovo Cimento (1955-1965)* **19** (Jan, 1961) 154–164.

[23] J. Goldstone, A. Salam, and S. Weinberg, *Broken symmetries*, *Phys. Rev.* **127** (Aug, 1962) 965–970.

[24] E. Gildener and S. Weinberg, *Symmetry breaking and scalar bosons*, *Phys. Rev. D* **13** (Jun, 1976) 3333–3341.

[25] E. Gildener, *Gauge-symmetry hierarchies*, *Phys. Rev. D* **14** (Sep, 1976) 1667–1672.

[26] S. Weinberg, *Gauge hierarchies*, *Physics Letters B* **82** (1979), no. 3 387 – 391.

[27] R. K. Kaul, *Naturalness and Electro-weak Symmetry Breaking*, `arXiv:0803.0381`.

[28] G. Bhattacharyya, *Electroweak Symmetry Breaking and BSM Physics (A Review)*, *Pramana* **72** (2009) 37–54, [`arXiv:0807.3883`].

[29] S. Weinberg, *Implications of dynamical symmetry breaking: An addendum*, *Phys. Rev. D* **19** (Feb, 1979) 1277–1280.

[30] L. Susskind, *Dynamics of spontaneous symmetry breaking in the weinberg-salam theory*, *Phys. Rev. D* **20** (Nov, 1979) 2619–2625.

[31] E. Farhi and L. Susskind, *Technicolour*, *Physics Reports* **74** (1981), no. 3 277 – 321.

[32] M. E. Peskin and D. V. Schroeder, *An Introduction to quantum field theory.* Addison-Wesley, Reading, USA, 1995.

[33] S. Scherer and M. R. Schindler, *A Chiral perturbation theory primer*, `hep-ph/0505265`.

[34] S. Dimopoulos and L. Susskind, *Mass Without Scalars*, *Nucl. Phys.* **B155** (1979) 237–252. [2,930(1979)].

[35] E. Eichten and K. Lane, *Dynamical breaking of weak interaction symmetries*, *Physics Letters B* **90** (1980), no. 1 125 – 130.

[36] S. King, *A WALK WITH TECHNICOLOR*, *Phys. Lett.* **B184** (1987) 49–54.

[37] R. S. Chivukula, *Weak Isospin Violation in 'Walking' Technicolor*, *Phys. Rev. Lett.* **61** (1988) 2657.

[38] S. F. King, *WALKING TECHNICOLOR MODELS*, *Nucl. Phys.* **B320** (1989) 487–540.

[39] T. Appelquist, *WALKING TECHNICOLOR*, in *IN *NAGOYA 1988, PROCEEDINGS, NEW TRENDS IN STRONG COUPLING GAUGE THEORIES* 34-43.*, 1988.

[40] R. Sundrum and S. D. H. Hsu, *Walking technicolor and electroweak radiative corrections*, *Nucl. Phys.* **B391** (1993) 127–146, [`hep-ph/9206225`].

[41] K. D. Lane and M. V. Ramana, *Walking technicolor signatures at hadron colliders*, *Phys. Rev.* **D44** (1991) 2678–2700.

[42] F. Sannino and K. Tuominen, *Orientifold theory dynamics and symmetry breaking*, *Phys. Rev.* **D71** (2005) 051901, [`hep-ph/0405209`].

[43] F. Sannino, *Dynamical Stabilization of the Fermi Scale: Phase Diagram of Strongly Coupled Theories for (Minimal) Walking Technicolor and Unparticles*, `arXiv:0804.0182`.

[44] R. S. Chivukula, *Lectures on technicolor and compositeness*, in *Flavor physics for the millennium. Proceedings, Theoretical Advanced Study Institute in elementary particle physics, TASI 2000, Boulder, USA, June 4-30, 2000*, pp. 731–772, 2000. `hep-ph/0011264`.

[45] S. Weinberg, *Phenomenological lagrangians*, *Physica A: Statistical Mechanics and its Applications* **96** (1979), no. 1 327 – 340.

[46] H. Georgi, *Weak Interactions and Modern Particle Theory.* 1984.

[47] A. Manohar and H. Georgi, *Chiral Quarks and the Nonrelativistic Quark Model*, *Nucl. Phys.* **B234** (1984) 189–212.

[48] J. Gasser and H. Leutwyler, *Chiral perturbation theory: Expansions in the mass of the strange quark*, *Nuclear Physics B* **250** (1985), no. 1 465 – 516.

[49] **Particle Data Group** Collaboration, M. t. Tanabashi, *Review of particle physics*, *Phys. Rev. D* **98** (Aug, 2018) 030001.

[50] T. Appelquist and L. C. R. Wijewardhana, *Chiral Hierarchies and Chiral Perturbations in Technicolor*, *Phys. Rev.* **D35** (1987) 774.

[51] T. Appelquist and L. C. R. Wijewardhana, *Chiral Hierarchies from Slowly Running Couplings in Technicolor Theories*, *Phys. Rev.* **D36** (1987) 568.

[52] A. G. Cohen and H. Georgi, *Walking Beyond the Rainbow*, *Nucl. Phys.* **B314** (1989) 7–24.

[53] T. Appelquist, D. Karabali, and L. C. R. Wijewardhana, *Chiral hierarchies and flavor-changing neutral currents in hypercolor*, *Phys. Rev. Lett.* **57** (Aug, 1986) 957–960.

[54] M. Soldate and R. Sundrum, *Z couplings to pseudo-goldstone bosons within extended technicolor*, *Nuclear Physics B* **340** (1990), no. 1 1 – 32.

[55] B. Balaji, *Goldstone bosons in the Appelquist-Terning ETC model*, *Phys. Rev.* **D51** (1995) 3969–3973, [`hep-ph/9505312`].

[56] B. Holdom, *Techniodor*, *Physics Letters B* **150** (1985), no. 4 301 – 305.

[57] K. Yamawaki, M. Bando, and K.-i. Matumoto, *Scale-invariant hypercolor model and a dilaton*, *Phys. Rev. Lett.* **56** (Mar, 1986) 1335–1338.

[58] T. Appelquist, T. Takeuchi, M. Einhorn, and L. Wijewardhana, *Higher mass scales and mass hierarchies*, *Physics Letters B* **220** (1989), no. 1 223 – 228.

[59] T. Appelquist and L. C. R. Wijewardhana, *Chiral hierarchies from slowly running couplings in technicolor theories*, *Phys. Rev. D* **36** (Jul, 1987) 568–580.

[60] S. F. King, *Composite/elementary extended technicolor*, *Physics Letters B* **195** (1987), no. 1 66 – 73.

[61] N. Evans and F. Sannino, *Minimal walking technicolour, the top mass and precision electroweak measurements*, `hep-ph/0512080`.

[62] R. Foadi, M. T. Frandsen, and F. Sannino, *125 GeV Higgs boson from a not so light technicolor scalar*, *Phys. Rev.* **D87** (2013), no. 9 095001, [`arXiv:1211.1083`].

[63] E. Witten, *An su(2) anomaly*, *Physics Letters B* **117** (1982), no. 5 324 – 328.

[64] C. T. Hill and E. H. Simmons, *Strong dynamics and electroweak symmetry breaking*, *Phys. Rept.* **381** (2003) 235–402, [`hep-ph/0203079`]. [Erratum: Phys. Rept.390,553(2004)].

[65] T. Appelquist, M. Piai, and R. Shrock, *Lepton dipole moments in extended technicolor models*, *Phys. Lett.* **B593** (2004) 175–180, [`hep-ph/0401114`].

[66] A. Belyaev, R. Foadi, M. T. Frandsen, M. Jarvinen, F. Sannino, and A. Pukhov, *Technicolor Walks at the LHC*, *Phys. Rev.* **D79** (2009) 035006, [`arXiv:0809.0793`].

[67] T. Appelquist, P. S. Rodrigues da Silva, and F. Sannino, *Enhanced global symmetries and the chiral phase transition*, *Phys. Rev.* **D60** (1999) 116007, [`hep-ph/9906555`].

[68] M. Bando, T. Kugo, and K. Yamawaki, *Nonlinear Realization and Hidden Local Symmetries*, *Phys. Rept.* **164** (1988) 217–314.

[69] M. Bando, T. Kugo, S. Uehara, K. Yamawaki, and T. Yanagida, *Is rho Meson a Dynamical Gauge Boson of Hidden Local Symmetry?*, *Phys. Rev. Lett.* **54** (1985) 1215.

[70] R. Foadi, M. T. Frandsen, T. A. Ryttov, and F. Sannino, *Minimal Walking Technicolor: Set Up for Collider Physics*, *Phys. Rev.* **D76** (2007) 055005, [`arXiv:0706.1696`].

[71] S. Weinberg, *Precise relations between the spectra of vector and axial-vector mesons*, *Phys. Rev. Lett.* **18** (Mar, 1967) 507–509.

[72] T. Appelquist and F. Sannino, *The Physical spectrum of conformal SU(N) gauge theories*, *Phys. Rev.* **D59** (1999) 067702, [`hep-ph/9806409`].

[73] M. Kurachi and R. Shrock, *Behavior of the S Parameter in the Crossover Region Between Walking and QCD-Like Regimes of an SU(N) Gauge Theory*, *Phys. Rev.* **D74** (2006) 056003, [`hep-ph/0607231`].

[74] M. Kurachi and R. Shrock, *Study of the Change from Walking to Non-Walking Behavior in a Vectorial Gauge Theory as a Function of N(f)*, *JHEP* **12** (2006) 034, [`hep-ph/0605290`].

[75] G. Bélanger, N. D. Christensen, A. Pukhov, and A. Semenov, *Slhaplus: A library for implementing extensions of the standard model*, *Computer Physics Communications* **182** (2011), no. 3 763 – 774.

[76] A. Belyaev, N. D. Christensen, and A. Pukhov, *CalcHEP 3.4 for collider physics within and beyond the Standard Model*, *Comput. Phys. Commun.* **184** (2013) 1729–1769, [`arXiv:1207.6082`].

[77] A. V. Semenov, *LanHEP: A Package for automatic generation of Feynman rules in field theory. Version 2.0*, `hep-ph/0208011`.

[78] S. D. Drell and T.-M. Yan, *Massive lepton-pair production in hadron-hadron collisions at high energies*, *Phys. Rev. Lett.* **25** (Aug, 1970) 316–320.

[79] D. Berdine, N. Kauer, and D. Rainwater, *Breakdown of the Narrow Width Approximation for New Physics*, *Phys. Rev. Lett.* **99** (2007) 111601, [`hep-ph/0703058`].

[80] **CMS** Collaboration, A. M. Sirunyan et al., *Search for high-mass resonances in dilepton final states in proton-proton collisions at* $\sqrt{s} =$ *13 TeV*, `arXiv:1803.0629`.

[81] E. Accomando, D. Becciolini, A. Belyaev, S. Moretti, and C. Shepherd-Themistocleous, *Z' at the LHC: Interference and Finite Width Effects in Drell-Yan*, *JHEP* **10** (2013) 153, [`arXiv:1304.6700`].

[82] M. Bondarenko, A. Belyaev, L. Basso, E. Boos, V. Bunichev, et al., "High Energy Physics Model Database : Towards decoding of the underlying theory (within Les Houches 2011: Physics at TeV Colliders New Physics Working Group Report)." `https://hepmdb.soton.ac.uk/`, arXiv:1203.1488, 2012.

[83] **NNPDF** Collaboration, R. D. Ball, V. Bertone, S. Carrazza, L. Del Debbio, S. Forte, A. Guffanti, N. P. Hartland, and J. Rojo, *Parton distributions with QED corrections*, *Nucl. Phys.* **B877** (2013) 290–320, [`arXiv:1308.0598`].

[84] R. Hamberg, W. L. van Neerven, and T. Matsuura, *A Complete calculation of the order* $\alpha - s^2$ *correction to the Drell-Yan K factor*, *Nucl. Phys.* **B359** (1991) 343–405.

[85] W. L. van Neerven and E. B. Zijlstra, *The O* $(alpha - s^{2)}$ *corrected Drell-Yan K factor in the DIS and MS scheme*, *Nucl. Phys.* **B382** (1992) 11–62.

[86] R. Hamberg, T. Matsuura, and W. van Neerven ZWPROD program (1989-2002), http://www.lorentz.leidenuniv.nl/research/neerven/DECEASED/Welcome.html.

[87] A. Buckley, J. Ferrando, S. Lloyd, K. Nordström, B. Page, M. Rüfenacht, M. Schönherr, and G. Watt, *LHAPDF6: parton density access in the LHC precision era*, *Eur. Phys. J.* **C75** (2015) 132, [`arXiv:1412.7420`].

[88] E. Accomando, A. Belyaev, L. Fedeli, S. F. King, and C. Shepherd-Themistocleous, *Z' physics with early LHC data*, *Phys. Rev.* **D83** (2011) 075012, [`arXiv:1010.6058`].

[89] **ATLAS** Collaboration, G. Aad et al., *Search for high-mass dilepton resonances in pp collisions at $\sqrt{s} = 8$ TeV with the ATLAS detector*, *Phys. Rev.* **D90** (2014), no. 5 052005, [`arXiv:1405.4123`].

[90] **ATLAS** Collaboration, M. Aaboud et al., *Search for heavy resonances decaying into a W or Z boson and a Higgs boson in final states with leptons and b-jets in 36 fb^{-1} of $\sqrt{s} = 13$ TeV pp collisions with the ATLAS detector*, *JHEP* **03** (2018) 174, [`arXiv:1712.0651`].

[91] **ATLAS** Collaboration, M. Aaboud et al., *Search for WW/WZ resonance production in $\ell\nu qq$ final states in pp collisions at $\sqrt{s} = 13$ TeV with the ATLAS detector*, *JHEP* **03** (2018) 042, [`arXiv:1710.0723`].

[92] **ATLAS** Collaboration, G. Aad et al., *Search for a new resonance decaying to a W or Z boson and a Higgs boson in the $\ell\ell/\ell\nu/\nu\nu + b\bar{b}$ final states with the ATLAS detector*, *Eur. Phys. J.* **C75** (2015), no. 6 263, [`arXiv:1503.0808`].

[93] K. G. Wilson, *Confinement of quarks*, *Phys. Rev. D* **10** (Oct, 1974) 2445–2459.

[94] C. Pica, *Beyond the Standard Model: Charting Fundamental Interactions via Lattice Simulations*, *PoS* **LATTICE2016** (2016) 015, [`arXiv:1701.0778`].

[95] T. DeGrand, *Lattice tests of beyond Standard Model dynamics*, *Rev. Mod. Phys.* **88** (2016) 015001, [`arXiv:1510.0501`].

[96] S. Catterall and F. Sannino, *Minimal walking on the lattice*, *Phys. Rev.* **D76** (2007) 034504, [`arXiv:0705.1664`].

[97] S. Catterall, J. Giedt, F. Sannino, and J. Schneible, *Phase diagram of SU(2) with 2 flavors of dynamical adjoint quarks*, *JHEP* **11** (2008) 009, [`arXiv:0807.0792`].

[98] Y. Shamir, B. Svetitsky, and T. DeGrand, *Zero of the discrete beta function in SU(3) lattice gauge theory with color sextet fermions*, *Phys. Rev.* **D78** (2008) 031502, [`arXiv:0803.1707`].

[99] L. Del Debbio, A. Patella, and C. Pica, *Higher representations on the lattice: Numerical simulations. SU(2) with adjoint fermions*, *Phys. Rev.* **D81** (2010) 094503, [`arXiv:0805.2058`].

[100] L. Del Debbio, M. T. Frandsen, H. Panagopoulos, and F. Sannino, *Higher representations on the lattice: Perturbative studies*, *JHEP* **06** (2008) 007, [`arXiv:0802.0891`].

[101] J. M. Maldacena, *The Large N limit of superconformal field theories and supergravity*, *Int. J. Theor. Phys.* **38** (1999) 1113–1133, [`hep-th/9711200`]. [Adv. Theor. Math. Phys.2,231(1998)].

[102] J. Polchinski, *String theory. Vol. 1: An introduction to the bosonic string.* Cambridge Monographs on Mathematical Physics. Cambridge University Press, 2007.

[103] K. Becker, M. Becker, and J. H. Schwarz, *String theory and M-theory: A modern introduction.* Cambridge University Press, 2006.

[104] E. Kiritsis, *String theory in a nutshell.* Princeton University Press, USA, 2019.

[105] D. Z. Freedman and A. Van Proeyen, *Supergravity.* Cambridge Univ. Press, Cambridge, UK, 2012.

[106] E. D'Hoker and D. Z. Freedman, *Supersymmetric gauge theories and the AdS / CFT correspondence*, in *Strings, Branes and Extra Dimensions: TASI 2001: Proceedings*, pp. 3–158, 2002. `hep-th/0201253`.

[107] L. Susskind, *The World as a hologram*, *J. Math. Phys.* **36** (1995) 6377–6396, [`hep-th/9409089`].

[108] E. Witten, *Anti-de Sitter space and holography*, *Adv. Theor. Math. Phys.* **2** (1998) 253–291, [`hep-th/9802150`].

[109] S. S. Gubser, I. R. Klebanov, and A. M. Polyakov, *Gauge theory correlators from noncritical string theory*, *Phys. Lett.* **B428** (1998) 105–114, [`hep-th/9802109`].

[110] A. Karch and E. Katz, *Adding flavor to AdS / CFT*, *JHEP* **06** (2002) 043, [`hep-th/0205236`].

[111] M. Kruczenski, D. Mateos, R. C. Myers, and D. J. Winters, *Meson spectroscopy in AdS / CFT with flavor*, *JHEP* **07** (2003) 049, [`hep-th/0304032`].

[112] J. Babington, J. Erdmenger, N. J. Evans, Z. Guralnik, and I. Kirsch, *Chiral symmetry breaking and pions in nonsupersymmetric gauge / gravity duals*, *Phys. Rev.* **D69** (2004) 066007, [`hep-th/0306018`].

[113] J. Erdmenger, N. Evans, I. Kirsch, and E. Threlfall, *Mesons in Gauge/Gravity Duals - A Review*, *Eur. Phys. J.* **A35** (2008) 81–133, [`arXiv:0711.4467`].

[114] J. Erlich, E. Katz, D. T. Son, and M. A. Stephanov, *QCD and a holographic model of hadrons*, *Phys. Rev. Lett.* **95** (2005) 261602, [`hep-ph/0501128`].

[115] L. Da Rold and A. Pomarol, *Chiral symmetry breaking from five dimensional spaces*, *Nucl. Phys.* **B721** (2005) 79–97, [`hep-ph/0501218`].

[116] T. Alho, N. Evans, and K. Tuominen, *Dynamic AdS/QCD and the Spectrum of Walking Gauge Theories*, *Phys. Rev.* **D88** (2013) 105016, [`arXiv:1307.4896`].

[117] N. Evans and K. Tuominen, *Holographic modelling of a light technidilaton*, *Phys. Rev.* **D87** (2013), no. 8 086003, [`arXiv:1302.4553`].

[118] **CMS** Collaboration, C. Collaboration, *Search for dark matter production in association with jets, or hadronically decaying W or Z boson at* $\sqrt{s} = 13\ TeV$, .

[119] F. Zimmermann, *Strategy and issues for the LHC upgrades and fair, including longer-term prospects*, .